Density Limit Disruptions in the Compact Toroidal Hybrid Experiment

by

James D. Kring

A dissertation submitted to the Graduate Faculty of
Auburn University
in partial fulfillment of the
requirements for the Degree of
Doctor of Philosophy

Auburn, Alabama
August, 7, 2021

Keywords: density limit disruptions, tokamak, stellarator, machine learning, bolometers

Approved by

David A. Maurer, Chair, Professor of Physics
Stephen F. Knowlton, Professor Emeritus of Physics
David A. Ennis, Associate Professor of Physics
Luca Guazzotto, Associate Professor of Physics
Allen L. Landers, Professor and Chair of Physics
Chad G. Rose, Assistant Professor, Mechanical Engineering

Abstract

Density limit disruptions in toroidal plasma experiments have been an active area of research for decades. Density limit disruptions are plasma terminations that occur as the plasma density is increased. Plasma disruptions in magnetically-confined, current-carrying toroidal devices result in a sudden loss of confinement leading to a rapid drop of the plasma temperature immediately followed by drop of the toriodal plasma current. Heat and particles are expelled to the edge of the plasma at a rate higher than in a normal discharge which can damage the plasma facing components on large experiments and future fusion reactors. Tokamak-like disruptions do not occur in current-free stellarators, where the required rotational transform is produced by currents in external coils, but exists as a radiative collapse.

This thesis presents the observations of density limit-induced disruptions in a current-carrying stellarator, the Compact Toroidal Hybrid (CTH) experiment at Auburn University. In addition, the development of an *in situ* wavelength calibration system for the x-ray imaging crystal spectrometers (XICS) on the Wendelstein 7-X (W7-X) experiment is described.

To further the study of CTH density limit disruptions, new bolometer arrays were installed on CTH. A synthetically trained De-Convolution Neural Network (DeCNN) based inversion method has been developed for the new bolometer arrays to capitalize on the available spatial information. The inverted bolometer fluctuations show spatial and temporal correlations with the poloidal magnetic field fluctuations indicating that the source of the radiation is magneto-hydrodynamic (MHD) instabilities.

The physics underlying the tokamak-like density limit in CTH plasmas may be ascribed to a radiative instability localized to a specific rational surface. The best predictor of the tokamak-like density limit characteristics across all ranges of vacuum rotational transform was found to be Hugill density limit, not the Greenwald limit. Of important significance, at increasing levels of vacuum rotational transform, the performance of the plasma (i.e. the slow collapse) is

not dictated by either Greenwald or Hugill limits but seems to be caused by increased plasma resistivity possibly due to toroidally trapped particles.

Acknowledgments

First and foremost, I would like to thank my Lord and Savior Jesus Christ whose death, burial, and resurrection provide salvation and hope for all who accept Him as their personal Savior.

Second, I would like to thank my amazing wife Rachel, who has been a constant encouragement and help to me as I have gone through graduate school.

Third, I would like to dedicate this work to my fifth and sixth grade teacher Amy Athey to fulfill a promise I made to her all those years ago.

Fourth, I would like to thank my advisor Dave Maurer who through continued patience and flexibility has taught me much more than just plasma physics but how to work with people as well. Throughout my time of researching fusion at CTH, I have learned a great deal about plasma physics, MHD, building diagnostics, and operating a very complicated machine which would not have been possible without the wonderful people working on CTH. I would like to thank fellow fusion researchers Greg Hartwell for teaching me the ins and outs about CTH, Steve Knowlton for the great discussions on density limits and other areas of plasma physics, John Dawson for his continual upkeep of the electronics that were broken throughout my research, David Ennis, and every other graduate student involved with CTH. I could not have accomplished this research without you. Thank you all!

Table of Contents

List of Figures

List of Tables

Chapter 1

Introduction

1.1 Introduction to Density Limit Disruptions in Toroidal Devices

Plasma disruptions in magnetically-confined, current-carrying toroidal devices result in a sudden loss of confinement leading to a fast drop of the plasma temperature immediately followed by a rapid quench of the toroidal plasma current. Due to the loss of confinement resulting from the drop of the poloidal magnetic field, heat and particles are expelled to the edge of the plasma at a rate higher than in a normal discharge. The large outward particle flux and heat flow to the vessel walls and divertor (if present) along with inductively generated relativistic electron beams may damage plasma facing components, especially in large tokamaks. The collapse of the plasma current produces larger than normal eddy currents in conducting plasma facing components and in the structure of the confinement device, leading to potentially excessive force-loading and mechanical damage. Because of these issues, the avoidance and mitigation of disruptions are considered essential for future power-producing tokamak devices such as ITER (1; 2; 3; 4) and SPARC (5).

Tokamak-like disruptions do not occur in current-free stellarators, where the required rotational transform is produced by currents in external coils. While the lack of plasma current should reduce the drive of current-driven magnetohydrodynamic (MHD) instabilities that often lead to major disruptions, the inherent 3D magnetic field structure may also play a role in the relative immunity of stellarators to disruption. In tokamaks, small levels of 3D fields are routinely applied to control the growth of resistive wall (6) and edge localized modes (7) and are also used for error field correction (8). Nonetheless, it is possible that bootstrap currents in some configurations of high-performance stellarators may reduce immunity of the stellarator to disruptions, especially at high plasma pressure.

Known causes of disruptions in toroidal current-carrying plasmas include operational limits on density (density limit), pressure (β limit), plasma current (low-q limit), unstable vertical drifts, and operator error or mechanical failure and other off-normal events. Density limit disruptions are known to occur in magnetic confinement experiments including tokamaks, reversed field pinches, spheromaks and field-reversed configurations, and serve as an upper limit for plasma density (9). The density in conventional stellarators is typically limited by radiative collapse on a slower time scale than that of a disruption. Since the mid-1960s, multiple studies have attempted to explain why the density limit appears in different magnetic confinement designs (10; 11; 12; 13; 14; 15). The highlights of these studies are shown in the following sections.

1.1.1 Murakami Limit

These density limit studies led to proposals of empirical scaling relationships governing the density limit. One of the initial scalings for tokamak devices was by Murakami (12) who observed a linear scaling law by plotting the maximum achievable electron plasma density ($n_{\mathrm{M}} = n_{\mathrm{e}}(\mathrm{max})$) against ratio of the toroidal magnetic field to the major radius of the plasma B_{T}/R using data taken from over ten different tokamaks as seen in Fig. 1.1.

This result prompted the calling of this scaling the Murakami limit or Murakami number which is defined as

$$n_{\mathrm{M}} < \frac{B_{\mathrm{T}}}{R_0} \tag{1.1}$$

where B_T is the toroidal magnetic field in Teslas and R_0 is the major radius in meters if the density n_M is expressed in units of $10^{20}m^{-3}$. For tokamaks, the Murakami limit scales like the plasma current ($\frac{B_{\mathrm{T}}}{R_0} \propto I_{\mathrm{P}}$). While the Murakami limit was thought to represent a global power balance of radiation losses and plasma heating, it was later found to be well surpassed when the plasma was very clean (13) and when additional heating was provided by neutral beam injection (16). Despite this shortcoming, the Murakami limit laid the foundation for future work by identifying the strongest dependence of the density, in that it scales with B_{T}/R.

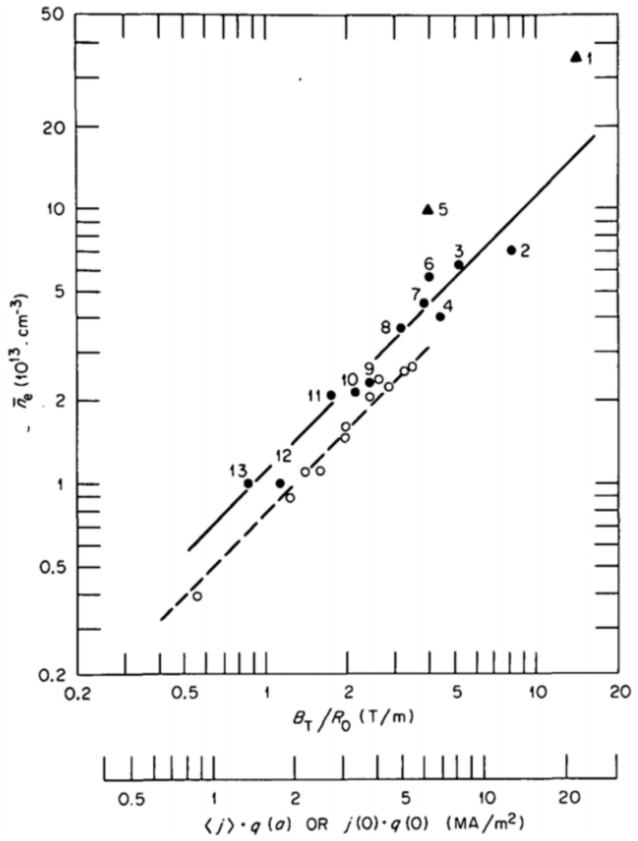

Figure 1.1: Maximum achievable n_e versus B_T/R of various tokamaks. a) The black triangles: the densities obtained by pulsing in cold neutral gas. b) The black dots: the densities obtained in normal operations. c) The open circles: the densities obtained in "constant-q(a) experiment" on ORMAK. Figure and caption reproduced from (12).

In addition, Murakami confirmed the phenomena of the appearance of disruptive instabilities associated with current channel shrinkage, edge cooling, and impurity flux.

1.1.2 Hugill Limit

As alluded to in the previous section, with more data available, it became obvious that the Murakami density limit was incomplete and insufficient to explain tokamak observations. On the DITE tokamak, the Murakami density limit was surpassed by up to a factor of two in discharges with auxilary heating and cleaner plasmas (17; 15). Fig. 1.2 shows the results from the DITE tokamak. With the help of neutral beam injection, the achievable density increased as $1/q$ increases. Fig. 1.2 also shows the operational space for the DITE tokamak with boundaries at the low q limit and the Hugill density limit.

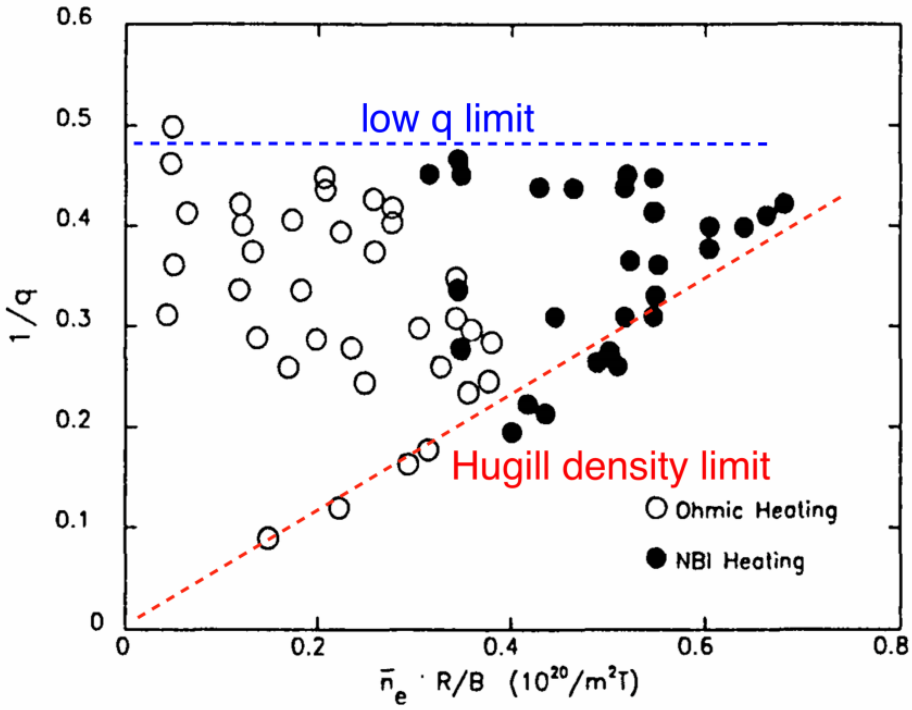

Figure 1.2: Hugill plot for DITE. Each circle represents a discharge. Figure and caption reproduced from (17).

The Hugill limit (15) has the form of

$$n_{\mathrm{H}} = C_{\mathrm{H}} \frac{B_{\mathrm{T}}}{qR_0} \tag{1.2}$$

with C_H being a scaling factor and q being the safety factor in cylindrical form. While possessing similar disruption phenomena as seen by Murakami, the disruptions in accordance with the Hugill limit were found to be insensitive to the input power when the input power was sufficiently large.

Expanding the experimental domain to include poloidally shaped tokamaks, Fig. 1.3 shows the operational space for the Alcator C, DIII and PBX experiments. If the Hugill limit is indeed a universal density scaling law, the the lower bounds of the operational spaces in Fig. 1.3 should align together, which is not seen. While the Hugill limits provides useful scaling behavior for circular, high-aspect ratio tokamak plasmas, when plasmas were strongly shaped, the Hugill scaling factor C_H could vary greatly indicating that a factor was missing in the Hugill limit.

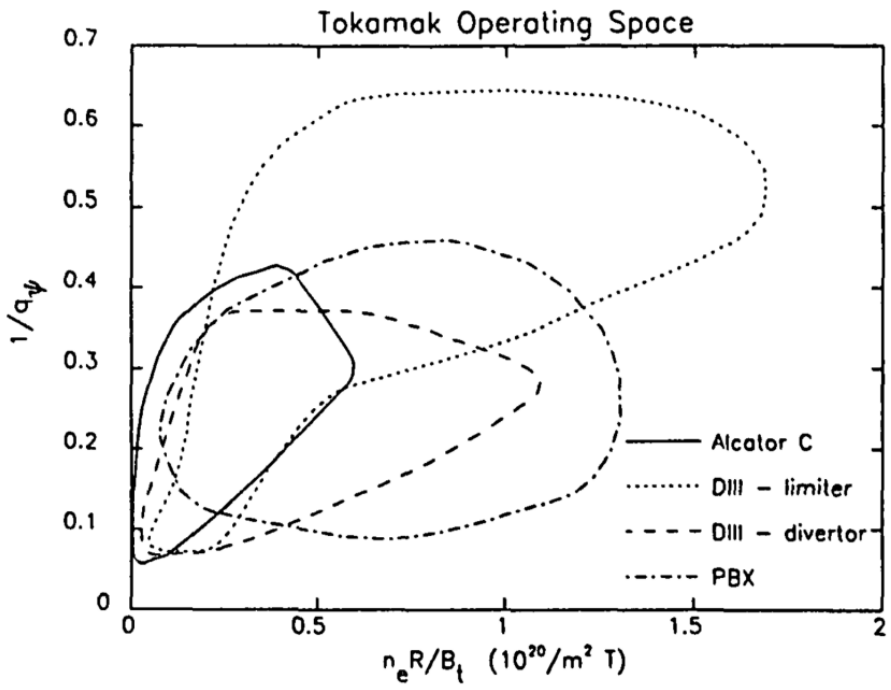

Figure 1.3: Hugill plot for Alcator C, DIII and PBX. Each circle represents a discharge. Figure and caption reproduced from (17).

1.1.3 Greenwald Limit

The inability of the Hugill limit to explain strongly shaped plasmas prompted further density scaling attempts. The most recent and widely used empirical scaling relationship at present for current carrying toroidal devices was proposed by Greenwald (18) in which the maximum achievable density is given by the equality:

$$n_{\mathrm{G}} = \frac{I_{\mathrm{p}}}{\pi a^2} \tag{1.3}$$

where I_p is the plasma current in mega-amperes, and a the semi-minor radius of the plasma in units of meters, and n_G is the maximum attainable line-averaged density expressed in units of $10^{20} m^{-3}$. In effect, the density scales with the plasma current density and surprisingly nothing else.

Fig. 1.4 shows Greenwald's plot for Alcator C density limits. Here, Greenwald used the original form of his limit which is $n_{\mathrm{e}} = \kappa J$ where κ is the plasma elongation and J is the

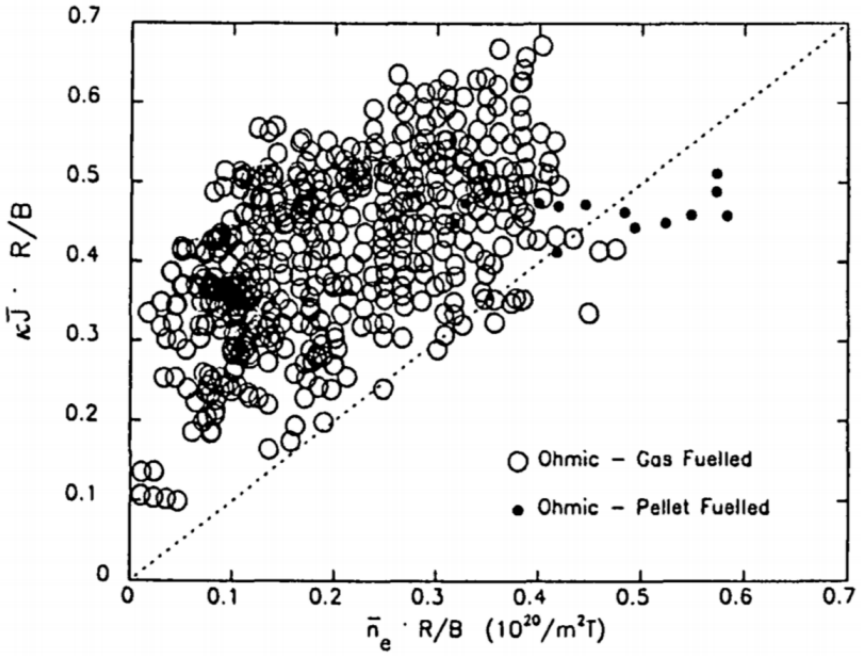

Figure 1.4: Greenwald density limit plot for Alcator C. Figure and caption reproduced from (18).

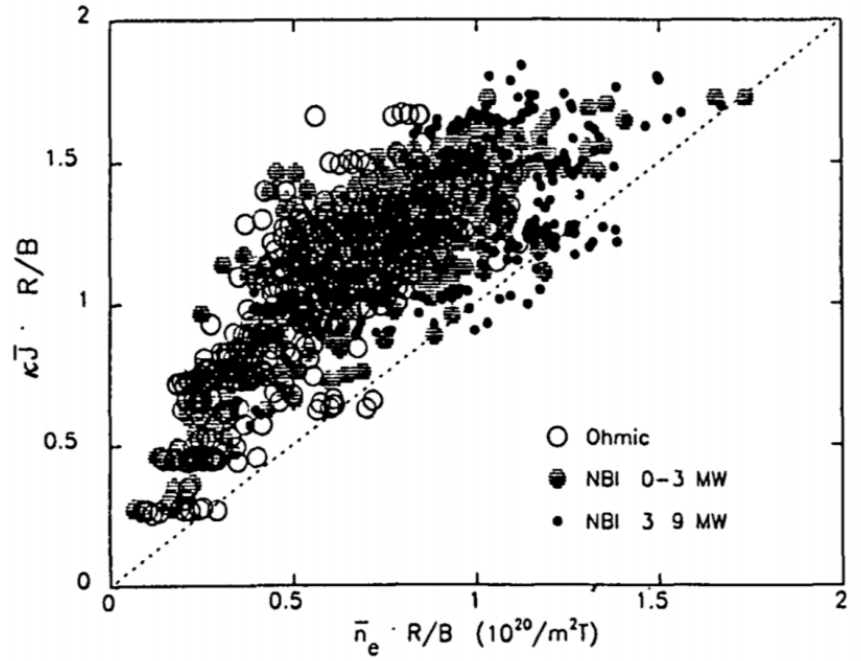

Figure 1.5: Greenwald density limit plot for DIII (limiter). Figure and caption reproduced from (18).

average current density. Fig. 1.5 shows the corresponding data taken from the DIII experiment. Greenwald's plots show the applicability of his limit, without using different scaling factors, to experiments with different plasma shapes. Note that the pellet fueled discharges on Alcator C exceed the Greenwald density limit by 20%. The observation that the Greenwald density limit can be exceeded by increasing only the core density shows it to be a local phenomenon related to the edge plasma density. This supposition forms the basis of a textbook model of density limit disruption (19). The Greenwald limit, while purely empirical with no explanation of the underlying physics driving the disruption, currently serves as the most widely accepted density limit scaling for current-carrying toroidal devices.

1.1.4 Sudo Limit

In contrast to tokamaks, stellarators typically carry no or rather small amounts of plasma current. While density limits can be observed in stellarators, they exhibit different characteristics. Hard disruptions do not occur, and instead the plasma shrinks and decays due to radiative collapse as the density limit is reached. The density limits in these conventional stellarators are often empirically modeled with the Sudo limit (20) as a power balance and has the form

$$n_{\mathrm{S}} = 0.25 \left(\frac{P_{\mathrm{in}} B_0}{a^2 R_0} \right)^{0.5} \tag{1.4}$$

where P_{in} is the absorbed power in megawatts, B_0 is the magnetic field strength on the plasma axis in Teslas, a the average minor radius in meters, and R_0 the major radius in meters. With additional stellarator data, the exponents in 1.4 are found to vary from $P_{\mathrm{in}}^{0.5\to1.0} B_0^{0.5\to1.0} R_0^{-1.5\to0}$(20; 21; 22).

1.1.5 Phenomenology of Density Limit Disruptions

Several phenomena may be observed in tokamak discharges as the density is raised toward the density limit. They include the appearance of MARFEs (23; 24), divertor detachment (25; 26), a drop in H-mode confinement (27; 28; 29), changes in ELM activity (30), a transition from

H-mode to L-mode (28; 31; 32), poloidal detachment (33; 34), increase of coherent MHD oscillations concurrent with a peaking of the current profile (35; 36), and finally major disruptions. The first four, MARFEs, divertor detachment, H-mode degradation and the change in ELM activity can happen over a wide range of densities, varying from $0.3 - 0.9\ n_G$. The other phenomena, the H/L mode transaction, poloidal detachment, shrinkage of current density profile, growing MHD activity and the disruptions, occur at or near the limit density n_G.

Cooling of the edge appears to be a key element in all observations of density limit driven disruptions (9). Observations of discharges with peaked density profiles that exceed the Greenwald density limit also support this hypothesis. Neutral beam injection (NBI) (37; 38), pellet injection (39; 40; 41) and transport modification (42; 43) have been used to obtain the peaked density profiles with line-averaged densities in excess of Greenwald limit. Radiation is usually proposed as the cause of the edge cooling, but no first-principle theory is universally accepted. Nonetheless, there is a general agreement on the final scenario of the density limit in that the edge plasma cools, the current profile narrows in the radial coordinate, growing MHD instabilities (usually the $m/n = 2/1$ tearing mode) develop followed by a loss of MHD equilibrium, and the final terminating current disruption (44). Because the radiated power from the plasma increases with density (45) and plasmas with high levels of impurities tend to be thermally unstable and cannot achieve high densities (11), several radiation models have been considered, including core radiation from high Z impurities (12), formation of thermal condensation or MARFEs (46), radial detachment (47; 48), and divertor detachment (49; 50). These models are able to reproduce some features of disruptions in certain cases with good quantitative agreement. However, they are not entirely satisfactory as they require assumptions about edge transport, which is not well understood. They also make predictions about power and impurity scaling that are not consistent with experimental observations (9).

Another approach to explain the cause of density limits focuses on enhanced turbulent transport. There is some evidence that increased edge transport at high densities is responsible for the edge cooling (51; 52; 53; 54; 55). Accordingly, several models have been developed to explain the increase of transport at high densities and its relation to the density limit (56; 57; 58; 59). Simulation work has successfully discovered regimes of extremely large turbulent

transport, which, to a certain extent, is consistent with experimental observations. However, further investigation is needed to find a comprehensive and well-characterized edge turbulence model. Present transport-based models are not able to make quantitative predictions. Both radiation and transport models have experimental ramifications that need to be pursued.

More recently, the thermo-resistive effect is being reconsidered to explain the physics behind the tokamak density limit. It combines several important effects with regard to tearing stability, including thermal effects on the 3D resistivity distribution (60; 61; 62; 63; 64). Specifically, it is a combination of nonlinearly-growing tearing modes leading to current profile narrowing and a model of radiation driven islands. The thermo-resistive formalism is found to be able to quantitatively reproduce the Greenwald density limit (18). To justify this mechanism, further investigation with experimental data of high spatial resolution is needed.

1.2 Goals of this Thesis

As fusion science is now moving into the era of controlled burning plasma tokamak experiments such as ITER (65; 1) and SPARC (5), critical challenges remain in the area of density limit disruptions. The work in this thesis uses the tokamak/stellarator hybrid at Auburn University called the Compact Toroidal Hybrid (CTH) to perform experiments with a goal of understanding the dynamics of density limit disruptions. The hybrid nature of CTH comes from its ability to vary externally applied rotational transform, i.e. the amount of three-dimensional (3D) magnetic field imposed from coils outside the plasma. More external rotational transform enhances the imposed poloidal magnetic field, that in tokamaks is primarily produced by the plasma current alone, effectively making CTH more stellarator-like. In principle, the stellarator configuration can avoid the problem of major disruptions by operating in MHD stable regimes. Indeed, experiments on current-carrying stellarators have shown evidences of disruption avoidance and improved positional stability (66; 67; 68).

Stellarators can operate with long pulses without significant auxiliary current drive. Thus the stellarator configuration is inherently a steady-state concept, and the stellarator approach is considered to be a realistic means to overcome a number of practical challenges to tokamak based fusion systems. What is more, the stellarator provides an example of the benefits that

strong 3D magnetic field shaping can have in relation to toroidal magnetic confinement. High performance stellarators such as LHD are exploring confinement regimes in current-free helical discharges (69), in which the average non-axisymmetric magnetic field component B_{3D} is comparable to the main axisymmetric toroidal filed B_0, $B_{3D}/B_0 \sim 0.3$. LHD has achieved an averaged beta value of 5% (70), comparable to that required for stellarator power plant. There is also evidence that quasi-symmetric field configurations in stellarators improves the confinement and plasma flow while exploiting the steady-state advantages of the stellarator (71; 72). On the other hand, modest levels of 3D field structure ($B_{3D}/B_0 \sim 10^{-4} - 10^{-3}$) have been applied to tokamaks to effect control of resistive wall modes (RWM) (73; 74) and edge localized modes (ELM) (7; 75). Relative theoretical work suggests that some form of 3D magnetic field structure is expected in the design of future steady state reactors (76; 77; 78).

A natural question arises, what are the potential benefits of a larger level of non-axisymmetric shaping field in nominally axisymmetric tokamaks, or how can the 3D vacuum equilibrium of helical configurations broadly improve control and maintenance of tokamak discharges. This could lead to the control and avoidance of disruptions as well as the sustainment of the discharges by means of supplemental rotational transform supplied by external helical or modular coils with $B_{3D}/B_0 \sim 10^{-2} - 10^{-1}$. To answer this question, a hybrid magnetic configuration such as CTH is useful, where a toroidal plasma current can be driven on the flux surface of a pure stellarator equilibrium. The goal of this approach is specifically to reduce plasma disruptions and their consequences by superimposing closed stellarator flux surfaces on current-driven toroidal discharges.

The major objectives of this work on CTH focus on understanding the effects of strong 3D shaping on the density limit disruptions seen in tokamak and hybrid discharges. An auxiliary goal is the enhancement of diagnostics for plasma research. Specifically they are:

- Developing a first of its kind, *in-situ* wavelength calibration for x-ray imaging crystal spectrometers using a custom developed x-ray ray tracing code.

- Exploring the dynamics of density limit disruptions using bolometers to measure the plasma's edge spatially-resolved power density (emission integrated over the spectral range in which most of the radiation takes place) during CTH discharges.

- Capitalizing on the bolometric spatial information using machine learning for advanced tomographic inversion of the incident power on the bolometers.

- Understanding the physics of major disruptions in hybrid discharges as well as the mechanism of their mitigation and avoidance with imposed external vacuum rotational transform.

1.3 Overview of Thesis

The outline of this thesis is as follows: Chapter 2 contains the developement of the *in-situ* wavelength calibration for x-ray imaging crystal spectrometers using a newly written x-ray raytracing code in Python, XICSRT (79; 80; 81). Chapter 3 discusses the CTH experiment, especially its flexible magnetic configuration, along with the diagnostics available in equilibrium reconstruction on CTH. Chapter 4 describes the developement and application of a De-Convolutional Neural Network (DeCNN), trained on synthetic data, for high resolution tomographic inversion of the new CTH bolometers. Chapter 5 contains a complete discussion of the scaling laws, experimental observations, involved physics and proposed mechanism of density limit disruptions on toroidal confinement experiments, similarity and uniqueness of density limit disruptions on CTH, and demonstrates the suppression of density limit disruptions with increasing amounts of stellarator transform provided by the external coil currents. Chapter 6 summarizes and discusses the major results of this thesis along with possible future work to extend current understanding of density limit disruptions and to apply the newly developed DeCNN in new areas.

Additionally, two appendices are included. The first details the ensemble of Python scripts written to access CTH data, perform reconstructions, handle analysis, and perform plotting. The second appendix explains the steps taken to absolutely calibrate the bolometers and SXR cameras.

References

[1] I. Organization, "Iter research plan within the staged approach (level iii—provisional version)," 2018.

[2] M. Lehnen, K. Aleynikova, P. Aleynikov, D. Campbell, P. Drewelow, N. Eidietis, Y. Gasparyan, R. Granetz, Y. Gribov, N. Hartmann, E. Hollmann, V. Izzo, S. Jachmich, S.-H. Kim, M. Kočan, H. Koslowski, D. Kovalenko, U. Kruezi, A. Loarte, S. Maruyama, G. Matthews, P. Parks, G. Pautasso, R. Pitts, C. Reux, V. Riccardo, R. Roccella, J. Snipes, A. Thornton, and P. de Vries, "Disruptions in iter and strategies for their control and mitigation," *Journal of Nuclear Materials*, vol. 463, pp. 39–48, 2015. PLASMA-SURFACE INTERACTIONS 21.

[3] P. C. de Vries, G. Pautasso, D. Humphreys, M. Lehnen, S. Maruyama, J. A. Snipes, A. Vergara, and L. Zabeo, "Requirements for triggering the iter disruption mitigation system," *Fusion Science and Technology*, vol. 69, no. 2, pp. 471–484, 2016.

[4] A. H. Boozer, "Pivotal issues on relativistic electrons in ITER," *Nuclear Fusion*, vol. 58, p. 036006, jan 2018.

[5] R. Sweeney, A. J. Creely, J. Doody, T. Fülöp, D. T. Garnier, R. Granetz, M. Greenwald, L. Hesslow, J. Irby, V. A. Izzo, and et al., "Mhd stability and disruptions in the sparc tokamak," *Journal of Plasma Physics*, vol. 86, no. 5, p. 865860507, 2020.

[6] C. Cates, M. Shilov, M. E. Mauel, G. A. Navratil, D. Maurer, S. Mukherjee, D. Nadle, J. Bialek, and A. Boozer, "Suppression of resistive wall instabilities with distributed, independently controlled, active feedback coils," *Physics of Plasmas*, vol. 7, no. 8, pp. 3133–3136, 2000.

[7] T. Evans, R. Moyer, J. Watkins, T. Osborne, P. Thomas, M. Becoulet, J. Boedo, E. Doyle, M. Fenstermacher, K. Finken, R. Groebner, M. Groth, J. Harris, G. Jackson, R. L. Haye, C. Lasnier, S. Masuzaki, N. Ohyabu, D. Pretty, H. Reimerdes, T. Rhodes, D. Rudakov, M. Schaffer, M. Wade, G. Wang, W. West, and L. Zeng, "Suppression of large edge

localized modes with edge resonant magnetic fields in high confinement diii-d plasmas," *Nuclear Fusion*, vol. 45, no. 7, p. 595, 2005.

[8] J. Scoville and R. L. Haye, "Multi-mode error field correction on the diii-d tokamak," *Nuclear Fusion*, vol. 43, no. 4, p. 250, 2003.

[9] M. Greenwald, "Density limits in toroidal plasmas," *Plasma Physics and Controlled Fusion*, vol. 44, no. 8, p. R27, 2002.

[10] L. Artsimovich, "Tokamak devices," *Nuclear Fusion*, vol. 12, no. 2, p. 215, 1972.

[11] V. Vershkov and S. Mirnov, "Role of impurities in current tokamak experiments," *Nuclear Fusion*, vol. 14, no. 3, p. 383, 1974.

[12] M. Murakami, J. Callen, and L. Berry, "Some observations on maximum densities in tokamak experiments," *Nuclear Fusion*, vol. 16, no. 2, p. 347, 1976.

[13] S. Fielding, J. Hugill, G. McCracken, J. Paul, R. Prentice, and P. Stott, "High-density discharges with gettered torus walls in dite," *Nuclear Fusion*, vol. 17, no. 6, p. 1382, 1977.

[14] S. Costa, R. D. Angelis, S. Ortolani, and M. Puiatti, "Total radiation measurements in the eta-beta ii experiment," *Nuclear Fusion*, vol. 22, no. 10, p. 1301, 1982.

[15] J. Hugill and et al, "High density operation in dite with neutral beam injection," tech. rep., Culham Laboratory Report, 1983.

[16] K. Axon, R. Gill, R. Hemsworth, J. Hugill, P. Lomas, J. Paul, B. Powell, R. Prentice, P. Stott, and D. Summers, "Electron and ion heating by neutral injection in the DITE tokamak," *Nuclear Fusion*, vol. 18, pp. 981–984, jul 1978.

[17] K. B. Axon, W. H. M. Clark, and J. G. Cordey, *Beam-driven currents, power balances and density limits with neutral injection in DITE*. International Atomic Energy Agency (IAEA): IAEA, 1981.

[18] M. Greenwald, J. Terry, S. Wolfe, S. Ejima, M. Bell, S. Kaye, and G. Neilson, "A new look at density limits in tokamaks," *Nuclear Fusion*, vol. 28, no. 12, p. 2199, 1988.

[19] J. Wesson and D. J. Campbell, *Tokamaks*, vol. p.749. Clarendon Press, 2004.

[20] S. Sudo, Y. Takeiri, H. Zushi, F. Sano, K. Itoh, K. Kondo, and A. Iiyoshi, "Scalings of energy confinement and density limit in stellarator/heliotron devices," *Nuclear Fusion*, vol. 30, no. 1, p. 11, 1990.

[21] ItohKimitaka and ItohSanae-Inoue, "Detached and attached plasma in stellarators," *Journal of the Physical Society of Japan*, vol. 57, no. 4, pp. 1269–1272, 1988.

[22] L. Giannone, J. Baldzuhn, R. Burhenn, P. Grigull, U. Stroth, F. Wagner, R. Brakel, C. Fuchs, H. J. Hartfuss, K. McCormick, A. Weller, C. Wendland, N. Team, E. Team, W.-A. Team, K. Itoh, and S.-I. Itoh, "Physics of the density limit in the w7-as stellarator," *Plasma Physics and Controlled Fusion*, vol. 42, no. 6, p. 603, 2000.

[23] B. Lipschultz, B. LaBombard, E. Marmar, M. Pickrell, J. Terry, R. Watterson, and S. Wolfe, "Marfe: an edge plasma phenomenon," *Nuclear Fusion*, vol. 24, no. 8, p. 977, 1984.

[24] B. Lipschultz, "Review of marfe phenomena in tokamaks," *Journal of Nuclear Materials*, vol. 145, pp. 15 – 25, 1987.

[25] G. Matthews, "Plasma detachment from divertor targets and limiters," *Journal of Nuclear Materials*, vol. 220, pp. 104 – 116, 1995.

[26] C. S. Pitcher and P. C. Stangeby, "Experimental divertor physics," *Plasma Physics and Controlled Fusion*, vol. 39, no. 6, p. 779, 1997.

[27] M. Greenwald, R. Boivin, F. Bombarda, P. Bonoli, C. Fiore, D. Garnier, J. Goetz, S. Golovato, M. Graf, R. Granetz, S. Horne, A. Hubbard, I. Hutchinson, J. Irby, B. LaBombard, B. Lipschultz, E. Marmar, M. May, G. McCracken, P. O'Shea, J. Rice, J. Schachter, J. Snipes, P. Stek, Y. Takase, J. Terry, Y. Wang, R. Watterson, B. Welch, and S. Wolfe, "H mode confinement in alcator c-mod," *Nuclear Fusion*, vol. 37, no. 6, p. 793, 1997.

[28] N. Asakura, K. Shimizu, H. Shirai, Y. Koide, and T. Takizuka, "Degradation of energy and particle confinement in high-density elmy h-mode plasmas on jt-60u," *Plasma Physics and Controlled Fusion*, vol. 39, no. 9, p. 1295, 1997.

[29] W. Suttrop, A. G. Peeters, F. Ryter, J. Stober, and the ASDEX Upgrade team, "Physics and scaling of the h-mode transition in asdex upgrade," *Plasma Physics and Controlled Fusion*, vol. 41, no. 3A, p. A569, 1999.

[30] H. Zohm, "Edge localized modes (elms)," *Plasma Physics and Controlled Fusion*, vol. 38, no. 2, p. 105, 1996.

[31] V. Mertens, M. Kaufmann, J. Neuhauser, J. Schweinzer, J. Stober, K. Buchl, O. Gruber, G. Haas, A. Herrmann, A. Kallenbach, and M. Weinlich, "High density operation close to greenwald limit and h mode limit in asdex upgrade," *Nuclear Fusion*, vol. 37, no. 11, p. 1607, 1997.

[32] F. Ryter, W. Suttrop, B. Brüsehaber, M. Kaufmann, V. Mertens, H. Murmann, A. G. Peeters, J. Stober, J. Schweinzer, H. Zohm, and A. U. Team, "H-mode power threshold and transition in asdex upgrade," *Plasma Physics and Controlled Fusion*, vol. 40, no. 5, p. 725, 1998.

[33] G. McCracken, J. Allen, K. Axon, R. Barnsley, S. Fielding, D. Goodall, N. Hawkes, J. Hugill, P. Johnson, G. Matthews, and C. Pitcher, "A study of detached plasmas in the dite tokamak," *Journal of Nuclear Materials*, vol. 145, pp. 181 – 185, 1987.

[34] J. Strachan, F. Boody, C. Bush, S. Cohen, B. Grek, L. Grisham, F. Jobes, D. Johnson, D. Mansfield, S. Medley, W. Morris, H. Park, J. Schivell, G. Taylor, K. Wong, S. Yoshikawa, M. Zarnstorff, and S. Zweben, "Experimental results from detached plasmas in tftr," *Journal of Nuclear Materials*, vol. 145, pp. 186 – 190, 1987.

[35] R. G. Kleva and J. F. Drake, "Density limit disruptions in tokamaks," *Physics of Fluids B: Plasma Physics*, vol. 3, no. 2, pp. 372–383, 1991.

[36] P. C. ITER Physics Expert Group on Disruptions, MHD, and I. P. B. Editors, "Chapter 3: Mhd stability operational limits and disruptions," *Nuclear Fusion*, vol. 39, no. 12, p. 2251, 1999.

[37] M. Bell, G. Schmidt, P. Efthimion, B. Grek, R. Hulse, D. Owens, H. Park, A. Ramsey, J. Schivell, and G. Taylor, "Attainment of high plasma densities in tftr with injection of multiple deuterium pellets," *Nuclear Fusion*, vol. 32, no. 9, p. 1585, 1992.

[38] R. Maingi, M. Mahdavi, T. Petrie, L. Baylor, T. Jernigan, R. L. Haye, A. Hyatt, M. Wade, J. Watkins, and D. Whyte, "Density limit studies on diii-d," *Journal of Nuclear Materials*, vol. 266269, pp. 598 – 603, 1999.

[39] Y. Kamada, N. Hosogane, R. Yoshino, T. Hirayama, and T. Tsunematsu, "Study of the density limit with pellet fuelling in jt-60," *Nuclear Fusion*, vol. 31, no. 10, p. 1827, 1991.

[40] A. Stabler, K. McCormick, V. Mertens, E. Muller, J. Neuhauser, H. Niedermeyer, K.-H. Steuer, H. Zohm, F. Dollinger, A. Eberhagen, G. Fussmann, O. Gehre, J. Gernhardt, T. Hartinger, J. Hofmann, E. Kakoulidis, M. Kaufmann, G. Kyriakakis, R. Lang, H. Murmann, W. Poschenrieder, F. Ryter, W. Sandmann, U. Schneider, G. Siller, F. Soldner, N. Tsois, O. Vollmer, and F. Wagner, "Density limit investigations on asdex," *Nuclear Fusion*, vol. 32, no. 9, p. 1557, 1992.

[41] R. Maingi, M. A. Mahdavi, T. C. Jernigan, R. J. L. Haye, A. W. Hyatt, L. R. Baylor, D. G. Whyte, M. R. Wade, T. W. Petrie, J. W. Cuthbertson, A. W. Leonard, M. Murakami, R. T. Snider, R. D. Stambaugh, J. G. Watkins, W. P. West, and R. D. Wood, "Investigation of physical processes limiting plasma density in high confinement mode discharges on diii-d," *Physics of Plasmas*, vol. 4, no. 5, pp. 1752–1760, 1997.

[42] F. X. Söldner, E. R. Müller, F. Wagner, H. S. Bosch, A. Eberhagen, H. U. Fahrbach, G. Fussmann, O. Gehre, K. Gentle, J. Gernhardt, O. Gruber, W. Herrmann, G. Janeschitz, M. Kornherr, K. Krieger, H. M. Mayer, K. McCormick, H. D. Murmann, J. Neuhauser,

R. Nolte, W. Poschenrieder, H. Röhr, K. H. Steuer, U. Stroth, N. Tsois, and H. Verbeek, "Improved confinement in high-density ohmic discharges in asdex," *Phys. Rev. Lett.*, vol. 61, pp. 1105–1108, Aug 1988.

[43] C. L. Fiore, J. E. Rice, P. T. Bonoli, R. L. Boivin, J. A. Goetz, A. E. Hubbard, I. H. Hutchinson, R. S. Granetz, M. J. Greenwald, E. S. Marmar, D. Mossessian, M. Porkolab, G. Taylor, J. Snipes, S. M. Wolfe, and S. J. Wukitch, "Internal transport barriers on alcator c-mod," *Physics of Plasmas*, vol. 8, no. 5, pp. 2023–2028, 2001.

[44] F. C. Schuller, "Disruptions in tokamaks," *Plasma Physics and Controlled Fusion*, vol. 37, no. 11A, p. A135, 1995.

[45] A. Gibson, "Radiation limits to tokamak operation," *Nuclear Fusion*, vol. 16, no. 3, p. 546, 1976.

[46] J. F. Drake, "Marfes: Radiative condensation in tokamak edge plasma," *The Physics of Fluids*, vol. 30, no. 8, pp. 2429–2433, 1987.

[47] P. Guzdar, C. Liu, and J. Dong, "Thermal equilibria of detached plasmas and density limits," *Nuclear Fusion*, vol. 28, no. 10, p. 1791, 1988.

[48] M. Z. Tokar, "On threshold of radial detachment in tokamaks," *Physics of Plasmas*, vol. 7, no. 6, pp. 2432–2438, 2000.

[49] J. Neuhauser and R. Wunderlich, "A radially continuous two-chamber model for the high-recycling divertor edge layer," *Journal of Nuclear Materials*, vol. 145, pp. 877 – 880, 1987.

[50] H. Capes, P. Ghendrih, A. Samain, A. Grosman, and J. P. Morera, "Thermal equilibrium in a diverted plasma," *Plasma Physics and Controlled Fusion*, vol. 32, no. 2, p. 103, 1990.

[51] D. L. Brower, C. X. Yu, R. V. Bravenec, H. Lin, N. C. Luhmann, W. A. Peebles, C. P. Ritz, B. A. Smith, A. J. Wootton, Z. M. Zhang, and S. J. Zhao, "Confinement degradation and enhanced microturbulence as long-time precursors to high-density-limit tokamak disruptions," *Phys. Rev. Lett.*, vol. 67, pp. 200–203, Jul 1991.

[52] M. Marinak, "Behaviour of the particle transport coefficients near the density limit in the microwave tokamak experiment," *Nuclear Fusion*, vol. 35, no. 4, p. 399, 1995.

[53] F. Sardei, P. Grigull, Y. Feng, G. Herre, D. Hildebrandt, J. Kißlinger, F. Wagner, and H. Wolff, "Boundary layer study on the wendelstein 7-as stellarator," *Journal of Nuclear Materials*, vol. 220, pp. 736 – 740, 1995.

[54] R. Moyer, J. Cuthbertson, T. Evans, G. Porter, and J. Watkins, "The role of turbulent transport in diii-d edge and divertor plasmas," *Journal of Nuclear Materials*, vol. 241, pp. 633 – 638, 1997.

[55] B. LaBombard, R. L. Boivin, M. Greenwald, J. Hughes, B. Lipschultz, D. Mossessian, C. S. Pitcher, J. L. Terry, S. J. Zweben, and A. Group, "Particle transport in the scrape-off layer and its relationship to discharge density limit in alcator c-mod," *Physics of Plasmas*, vol. 8, no. 5, pp. 2107–2117, 2001.

[56] F. A. Haas and A. Thyagaraja, "A phenomenological interpretation of transport limits and slow-time evolution in tokamaks," *Plasma Physics and Controlled Fusion*, vol. 28, no. 8, p. 1093, 1986.

[57] D. R. Thayer and P. H. Diamond, "Thermally driven convective cells and tokamak edge turbulence," *The Physics of Fluids*, vol. 30, no. 12, pp. 3724–3734, 1987.

[58] R. W. Harvey and R. O. Dendy, "A trapped passing fluid model for tokamak neoclassical transport," *Physics of Fluids B: Plasma Physics*, vol. 4, no. 4, pp. 902–910, 1992.

[59] B. N. Rogers, J. F. Drake, and A. Zeiler, "Phase space of tokamak edge turbulence, the $L-H$ transition, and the formation of the edge pedestal," *Phys. Rev. Lett.*, vol. 81, no. 20, 1998.

[60] D. A. Gates and L. Delgado-Aparicio, "Origin of tokamak density limit scalings," *Phys. Rev. Lett.*, vol. 108, no. 16, p. 165004, 2012.

[61] D. Gates, L. Delgado-Aparicio, and R. White, "Physics of radiation-driven islands near the tokamak density limit," *Nuclear Fusion*, vol. 53, no. 6, p. 063008, 2013.

[62] R. B. White, D. A. Gates, and D. P. Brennan, "Thermal island destabilization and the greenwald limit," *Physics of Plasmas*, vol. 22, no. 2, p. 022514, 2015.

[63] D. A. Gates, D. P. Brennan, L. Delgado-Aparicio, Q. Teng, and R. B. White, "Thermo-resistive disruptions and the tokamak density limit," *Physics of Plasmas*, vol. 23, no. 5, p. 056113, 2016.

[64] Q. Teng, D. Brennan, L. Delgado-Aparicio, D. Gates, J. Swerdlow, and R. White, "A predictive model for the tokamak density limit," *Nuclear Fusion*, vol. 56, no. 10, p. 106001, 2016.

[65] K. Ikeda, "Progress in the iter physics basis," *Nuclear Fusion*, vol. 47, no. 6, 2007.

[66] H. Ikezi, K. F. Schwarzenegger, and C. Ludescher, "Semi-stellarator field stabilization of tokamak plasma," *The Physics of Fluids*, vol. 22, no. 10, pp. 2009–2013, 1979.

[67] W. .-A. Team, "Stabilization of the (2, 1) tearing mode and of the current disruption in the w7-a stellarator," *Nuclear Fusion*, vol. 20, no. 9, p. 1093, 1980.

[68] M. Hirsch, J. Baldzuhn, C. Beidler, R. Brakel, R. Burhenn, A. Dinklage, H. Ehmler, M. Endler, V. Erckmann, Y. Feng, J. Geiger, L. Giannone, G. Grieger, P. Grigull, H.-J. HartfuÃ, D. Hartmann, R. Jaenicke, R. KÃ¶nig, H. P. Laqua, H. MaaÃberg, K. McCormick, F. Sardei, E. Speth, U. Stroth, F. Wagner, A. Weller, A. Werner, H. Wobig, S. Zoletnik, and for the W7-AS Team, "Major results from the stellarator wendelstein 7-as," *Plasma Physics and Controlled Fusion*, vol. 50, no. 5, p. 053001, 2008.

[69] O. Motojima, H. Yamada, A. Komori, N. Ohyabu, K. Kawahata, O. Kaneko, S. Masuzaki, A. Ejiri, M. Emoto, H. Funaba, M. Goto, K. Ida, H. Idei, S. Inagaki, N. Inoue, S. Kado, S. Kubo, R. Kumazawa, T. Minami, J. Miyazawa, T. Morisaki, S. Morita, S. Murakami, S. Muto, T. Mutoh, Y. Nagayama, Y. Nakamura, H. Nakanishi, K. Narihara, K. Nishimura, N. Noda, T. Kobuchi, S. Ohdachi, Y. Oka, M. Osakabe, T. Ozaki, B. J. Peterson, A. Sagara, S. Sakakibara, R. Sakamoto, H. Sasao, M. Sasao, K. Sato, M. Sato, T. Seki, T. Shimozuma, M. Shoji, H. Suzuki, Y. Takeiri, K. Tanaka, K. Toi, T. Tokuzawa,

K. Tsumori, K. Tsuzuki, I. Yamada, S. Yamaguchi, M. Yokoyama, K. Y. Watanabe, T. Watari, Y. Hamada, K. Matsuoka, K. Murai, K. Ohkubo, I. Ohtake, M. Okamoto, S. Satoh, T. Satow, S. Sudo, S. Tanahashi, K. Yamazaki, M. Fujiwara, and A. Iiyoshi, "Initial physics achievements of large helical device experiments," *Physics of Plasmas*, vol. 6, no. 5, pp. 1843–1850, 1999.

[70] A. Komori, H. Yamada, O. Kaneko, and et al, "Development of net-current free heliotron plasmas in the large helical device," in *22nd IAEA Fusion Energy Conference*, (Geneva), 2008.

[71] M. C. Zarnstorff, L. A. Berry, A. Brooks, E. Fredrickson, G.-Y. Fu, S. Hirshman, S. Hudson, L.-P. Ku, E. Lazarus, D. Mikkelsen, D. Monticello, G. H. Neilson, N. Pomphrey, A. Reiman, D. Spong, D. Strickler, A. Boozer, W. A. Cooper, R. Goldston, R. Hatcher, M. Isaev, C. Kessel, J. Lewandowski, J. F. Lyon, P. Merkel, H. Mynick, B. E. Nelson, C. Nuehrenberg, M. Redi, W. Reiersen, P. Rutherford, R. Sanchez, J. Schmidt, and R. B. White, "Physics of the compact advanced stellarator ncsx," *Plasma Physics and Controlled Fusion*, vol. 43, no. 12A, p. A237, 2001.

[72] J. M. Canik, D. T. Anderson, F. S. B. Anderson, C. Clark, K. M. Likin, J. N. Talmadge, and K. Zhai, "Reduced particle and heat transport with quasisymmetry in the helically symmetric experiment," *Physics of Plasmas*, vol. 14, no. 5, p. 056107, 2007.

[73] M. Okabayashi, J. Bialek, A. Bondeson, M. Chance, M. Chu, A. Garofalo, R. Hatcher, Y. In, G. Jackson, R. Jayakumar, T. Jensen, O. Katsuro-Hopkins, R. L. Haye, Y. Liu, G. Navratil, H. Reimerdes, J. Scoville, E. Strait, M. Takechi, A. Turnbull, P. Gohil, J. Kim, M. Makowski, J. Manickam, and J. Menard, "Control of the resistive wall mode with internal coils in the diiiâd tokamak," *Nuclear Fusion*, vol. 45, no. 12, p. 1715, 2005.

[74] S. Sabbagh, J. Berkery, R. Bell, J. Bialek, S. Gerhardt, J. Menard, R. Betti, D. Gates, B. Hu, O. Katsuro-Hopkins, B. LeBlanc, F. Levinton, J. Manickam, K. Tritz, and H. Yuh, "Advances in global mhd mode stabilization research on nstx," *Nuclear Fusion*, vol. 50, no. 2, p. 025020, 2010.

[75] Y. Liang, H. R. Koslowski, P. R. Thomas, E. Nardon, S. Jachmich, B. Alper, P. Andrew, Y. Andrew, G. Arnoux, Y. Baranov, M. BÃ©coulet, M. Beurskens, T. Biewer, M. Bigi, K. Crombe, E. D. L. Luna, P. de Vries, T. Eich, H. G. Esser, W. Fundamenski, S. Gerasimov, C. Giroud, M. P. Gryaznevich, D. Harting, N. Hawkes, S. Hotchin, D. Howell, A. Huber, M. Jakubowski, V. Kiptily, A. Kreter, L. Moreira, V. Parail, S. D. Pinches, E. Rachlew, O. Schmitz, O. Zimmermann, and J.-E. Contributors, "Active control of type-i edge localized modes on jet," *Plasma Physics and Controlled Fusion*, vol. 49, no. 12B, p. B581, 2007.

[76] A. H. Boozer, "Stellarators and the path from iter to demo," *Plasma Physics and Controlled Fusion*, vol. 50, no. 12, p. 124005, 2008.

[77] A. H. Boozer, "Use of nonaxisymmetric shaping in magnetic fusion," *Physics of Plasmas*, vol. 16, no. 5, p. 058102, 2009.

[78] D. A. Spong, "3d toroidal physics: Testing the boundaries of symmetry breaking," *Physics of Plasmas*, vol. 22, no. 5, p. 055602, 2015.

[79] J. Kring, N. Pablant, A. Langenberg, J. Rice, L. Delgado-Aparicio, D. Maurer, P. Traverso, M. Bitter, K. Hill, and M. Reinke, "In situ wavelength calibration system for the x-ray imaging crystal spectrometer (xics) on w7-x," *Review of Scientific Instruments*, vol. 89, no. 10, p. 10F107, 2018.

[80] *XICSRT package*, 2021. https://pypi.org/project/xicsrt.

[81] *XICSRT sourcecode*, 2021. https://github.com/PrincetonUniversity/xicsrt.

Chapter 2

In-situ Wavelength Calibration System for the X-ray Imaging Crystal Spectrometer on W7-X

2.1 Introduction

Wendelstein 7-X (W7-X) (1) is a neoclassically optimized, quasi-isodynamic stellarator that began operation in 2015 (2). W7-X, shown in Fig. 2.1, has a major radius R_0 of 5.5 m, a minor radius a of 0.53 m, a magnetic field B_0 of up to 3 T, and an eventual input power of up to 14 MW. While W7-X has already performed many experiments, what is relevant here are the impurity confinement studies in a neoclassically optimized stellarator (3; 4).

The primary diagnostic for these impurity confinement studies is the X-ray Imaging Crystal Spectrometer (XICS) (6; 7; 8; 9). XICS detects the emission of highly charged impurity ions to provide ion temperature, electron temperature, plasma flow velocity, and impurity ion density profiles. XICS systems have been used on W7-X (10), LHD (11), Alcator C-Mod (12), EAST (13), KSTAR (14) and other experiments with a XICS planned for ITER (15). The XICS system currently serves as the primary diagnostic for time resolved ion temperature (T_i) and radial electric field E_r (16) profiles on W7-X (17; 18).

The ion temperature is found from the Doppler broadening of spectral lines; the electron temperature from the intensity ratio of different x-ray wavelengths; the flow velocity from the Doppler shift of the lines; and the impurity ion density from the line intensities. In a stellarator, the radial electric field E_r can be inferred through measurements of the perpendicular plasma flow, $u_\perp$(19). Measured E_r profiles are important for many aspects of stellarator physics including the study of the neoclassical optimization in W7-X. Existing XICS systems lack any independent wavelength calibration capability and are currently based on plasma dependent

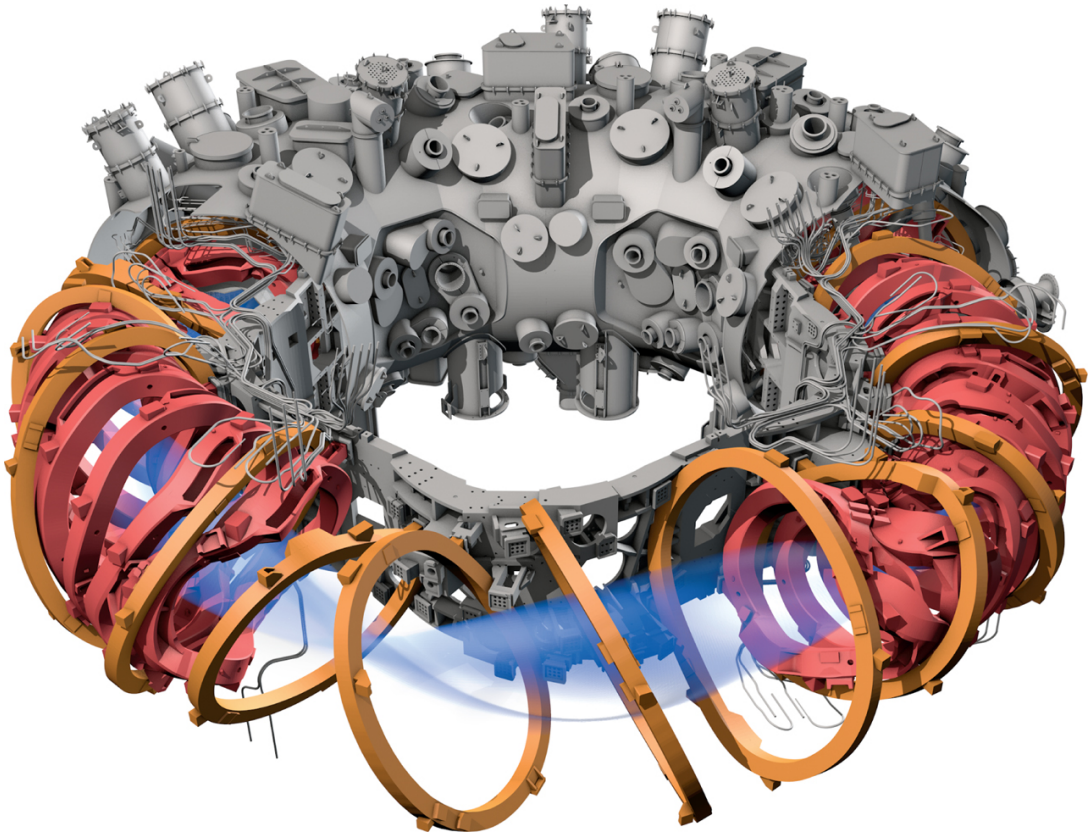

Figure 2.1: CAD rendering of the W7-X cryostat with its many ports, the magnetic coils, and the plasma (5).

calibrations. On tokamaks, plasma flow measurements are calibrated using locked mode plasmas, or through reversing the plasma flow. However, on stellarators, locked mode plasmas are not available, and the measurements are calibrated based on the assumption that the measurements are flux surface quantities. This chapter presents an independent, robust plasma flow calibration design that will work for any XICS system independent of the experiment.

2.2 XICS Wavelength Calibration System

2.2.1 XICS Overview

The XICS system on W7-X uses spherically bent crystals to diffract x-rays to photon counting imaging detectors. The spectral resolution of the diagnostic is produced by the crystals ability to diffract light of different wavelengths at different angles according to Bragg's Law. Bragg's Law is defined as

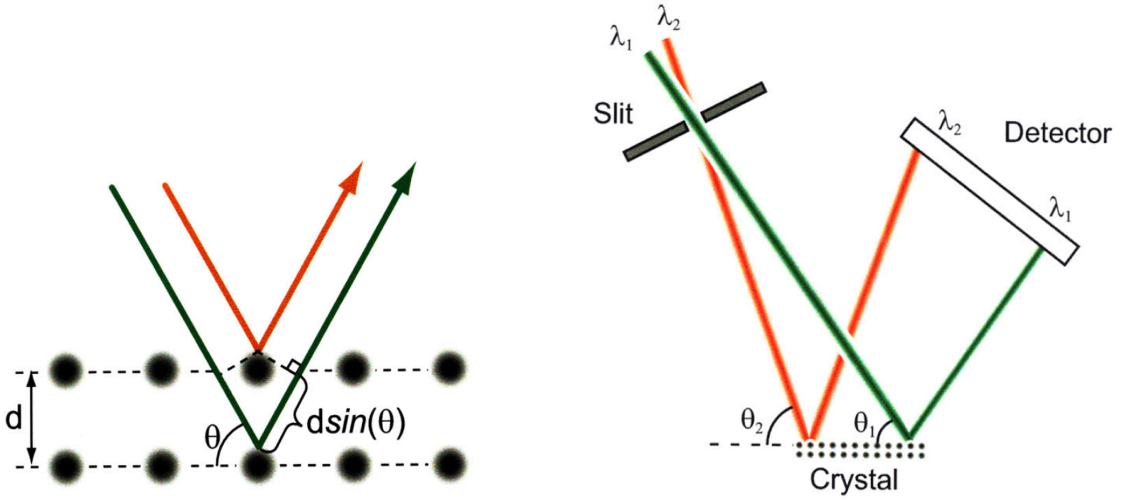

(a) (b)

Figure 2.2: Illustration of Bragg's Law in the diffraction of x-rays off a crystal lattice (a). Application of Bragg's Law to create a x-ray crystal spectrometer (b).

$$n\lambda = 2d\sin(\theta_{\mathrm{B}}) \tag{2.1}$$

where n is the order of diffraction, λ is the wavelength of the incident x-ray, d the atomic spacing in the crystal lattice, and θ_{B} is the scattering angle also known as the Bragg angle. Fig. 2.2(a) illustrates how x-ray diffraction according to Bragg's Law works with the crystal layers.

Applying the property of crystals, to diffract x-rays according to their wavelength, one can construct a crystal x-ray spectrometer. Fig. 2.2(b) shows a simple spectrometer setup where a flat crystal is used to diffract x-rays coming through the slit to different parts of the detector based upon the x-ray wavelength. Note that for each wavelength only a small portion of the crystal is used. This limitation becomes important when attempting to use this simple crystal spectrometer to measure low intensity x-ray wavelengths.

A solution to improve the x-ray gathering potential of the spectrometer without increasing the integration time, is to bend the crystal. Fig. 2.3 shows a circularly bent crystal that allows the entire crystal surface to be used to diffract a particular x-ray wavelength. With this arrangement, the focal points for different x-ray wavelengths now fall on the Rowland circle at different points. A Rowland surface is the surface on which the focal points of different

x-ray wavelengths will lie and is dependent on the geometry of the crystal. The impact of the crystal geometry and its corresponding Rowland surface means that for slightly different x-ray wavelengths incident on the detector the x-ray origination points (i.e. the plasma) are slightly spatially different. This side affect of improving x-ray gathering ability, in that different wavelengths are viewing slightly different portions of the plasma, is an important design consideration.

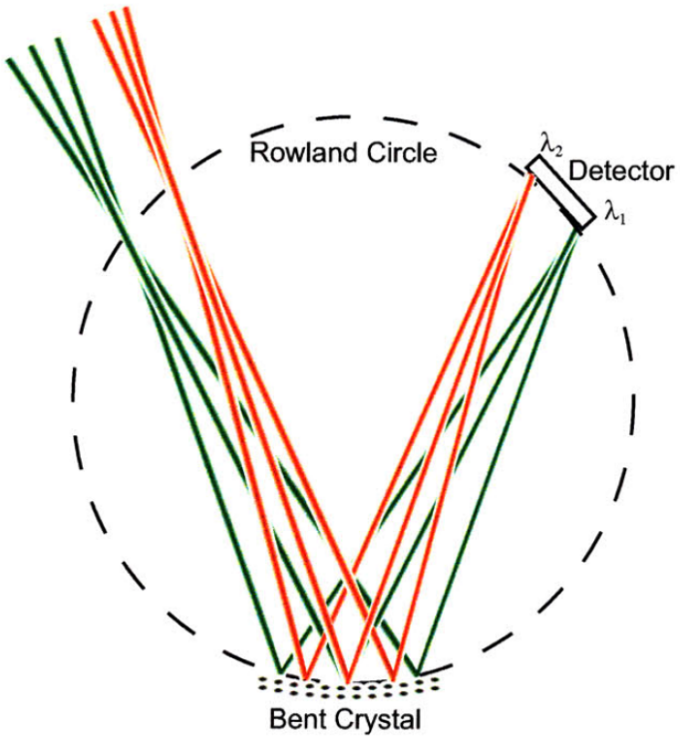

Figure 2.3: A bent crystal spectrometer allows the entire crystal to be used to diffract x-rays of the same wavelength.

A further enhancement to the circularly bent crystal spectrometer is to bend the crystal spherically which allows both spectral and spatial information to be gathered from the x-rays. Fig. 2.4 gives an example of a spherically bent crystal spectrometer and highlights its complexity. Possessing two focal points, the sagittal focal point f_s is for determining the spatial information and the meridional focal point f_m is for the spectral information. Being spherically bent, the Rowland circle in Fig. 2.3 now becomes a Rowland sphere. Because the detector is planar, the intersection of the detector with the Rowland sphere is a curve, meaning for multiple wavelengths, an image is now produced on the detector. Thus, as you vary the spatial location

of the source of the x-rays, the point on the detector will vary vertically up or down (sagittal plane) along a curve on the detector. Because of the axis of rotation, as the source of the x-rays varies down in the sagittal plane, the corresponding point on detector varies upward. A design consideration becomes apparent because, with a planar detector, only one x-ray wavelength can be appropriately focused on the detector.

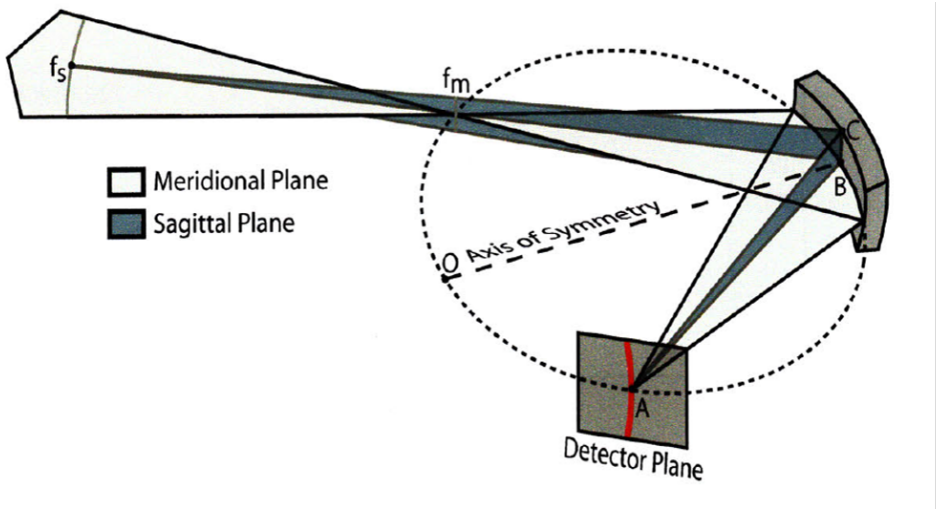

Figure 2.4: A spherically bent crystal spectrometer allows for both spatial and spectral information to be gathered from the detector's image. The Meridional (horizontal) plane provides spectral resolution. The Sagittal (vertical) plane provides spatial resolution.

The W7-X XICS diagnostic consists of two channels utilizing two spherically bent quartz crystals which measure the Ar^{16+} and Ar^{17+}/Fe^{24+} spectra respectively. In particular, the Ar^{16+} channel utilizes a Quartz (11-20) crystal with a radius of curvature of 1450 mm. Fig. 2.5 shows a side view of the XICS system. The crystals are housed in the cylindrical vacuum chamber visible on the far right of the system. The view of XICS extends to just below the magnetic axis and above the magnetic axis to about $r_{\text{eff}} = 0.8$. Possessing a view above and below the magnetic access greatly helps the tomographic inversion process.

Alluded to in the introduction to this chapter, XICS on W7-X is used to infer the radial electric field, E_r, from the perpendicular plasma flow, $u_\perp$. The measurement resolution of the perpendicular plasma flow, when ignoring systematic errors, is $5\mu m$ of line shift on the detector leading to an interpreted velocity error of $\Delta u_\perp = 1km/s$ ($\Delta E_r = 2kV/m$) with typical levels of argon puffing and a $10ms$ integration time. Better resolution is available through

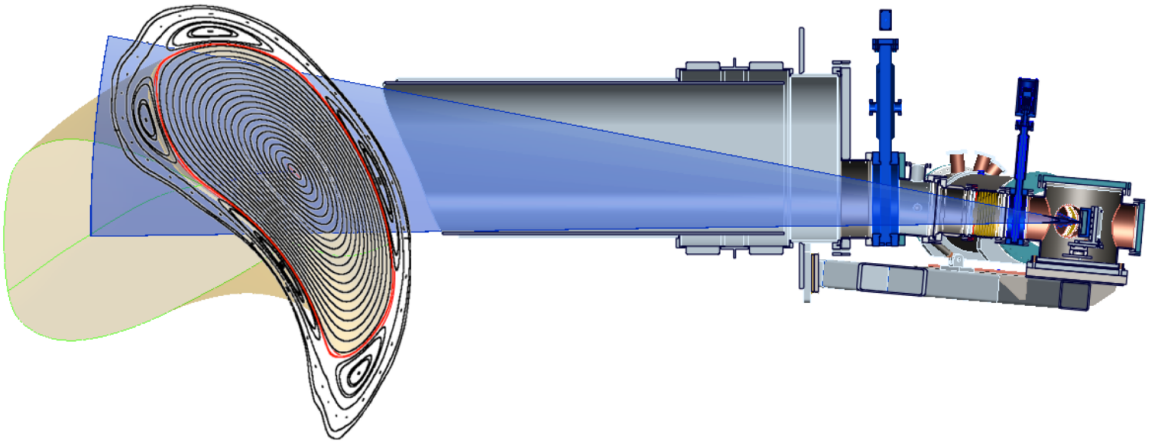

Figure 2.5: A side view of the X-ray Imaging Crystal Spectrometer (XICS) is shown highlighting the spatial resolution of the spectrometer (16).

additional time binning. The primary systematic errors in these measurements are due to the absolute wavelength calibration across the detector, which in this system, is equivalent to the absolute spatial alignment between the crystal and the detector. The absolute alignment can be considered in two parts: a constant shift across the detector, and a tilt of the detector leading to a linear shift of the wavelength. Without an absolute wavelength reference, the calibration is based on the ability to see a portion of the plasma on both sides of the magnetic axis under the assumption that the perpendicular flow is a flux surface quantity and the parallel flow is negligible.

Changes in the absolute wavelength calibration are expected to occur at least on the timescale of thermal changes in the diagnostic or the surrounding environment. Only a few degrees of temperature change, similar to what can be expected from an air conditioning cycle, have been shown to cause thermal expansion of the crystal lattice structure and therefore lead to spectral line shifts on the order of the desired plasma flow measurements (20). Similarly, thermal expansion of the steel structures that the crystal and detector are mounted on are also on the order to potentially cause significant calibration changes. Measurements of the crystal temperature and repeated calibrations during the planned long pulse discharges can be used to compensate for any spectral line shifts due to thermal expansion.

2.2.2 Calibration System Hardware

The wavelength calibration system designed for XICS consists of a x-ray tube positioned in front of the diffracting spherical crystal in order to provide x-ray calibration lines. The specific x-ray lines produced by the chosen anode for the x-ray tube will match the system's spectral range. This wavelength calibration design will illuminate all spatial channels on the detector simultaneously. The full spatial illumination is achieved by positioning the x-ray tube close to the spherical crystal and inside the focal points of the spherical crystal. A discussion on the modeling and experimental testing of this setup is covered later on in this chapter.

The x-ray tube for this calibration system is the XRT 30 by PROTO Manufacturing Inc. A Cadmium anode on the x-ray tube will provide the Cd $L\alpha$ and Cd $L\beta$ lines needed to calibrate the Ar^{16+} and Ar^{17+}/Fe^{24+} channels respectively for XICS. The x-ray tube will be operated up to 15 KeV and 2 mA. It will be placed 100mm from the crystals, between the crystals and the plasma. For routine operation between discharges or during long discharges, the x-ray tube is mounted on a rotating arm attached to a standard rotary feedthrough with fine motion control. This setup allows the x-ray tube to be easily rotated in and out of the line of sight of the spherical crystals.

The assembled calibration design is pictured in Fig. 2.6. For simplicity, the flanges, nipples, feedthroughs, cooling lines, and cabling have been hidden from the rendering in Fig. 2.6. The vertical shaft pictured connects the rotary feedthrough to the rotating arm holding the x-ray tube in addition to a counterweight balancing the x-ray tube. The two arms extending from the upper middle portion of the vertical shaft are physical safety stopping arms that prevent the x-ray tube from being positioned such that x-rays would enter the W7-X experiment. A post fastened to the top flange is the non-rendered component that will limit the motion of the arms.

Fig. 2.7 shows how the calibration system will replace the top flange on the chamber that houses the crystal. On the left, the crystal chamber is shown with this new addition placed on top. Progressing to the right in Fig. 2.7, the location of the calibration design can be seen with respect to the spherical crystal. Shown here, the x-ray tube is in the active position required for illumination of one of the detector channels. The system can be rotated to place the x-ray

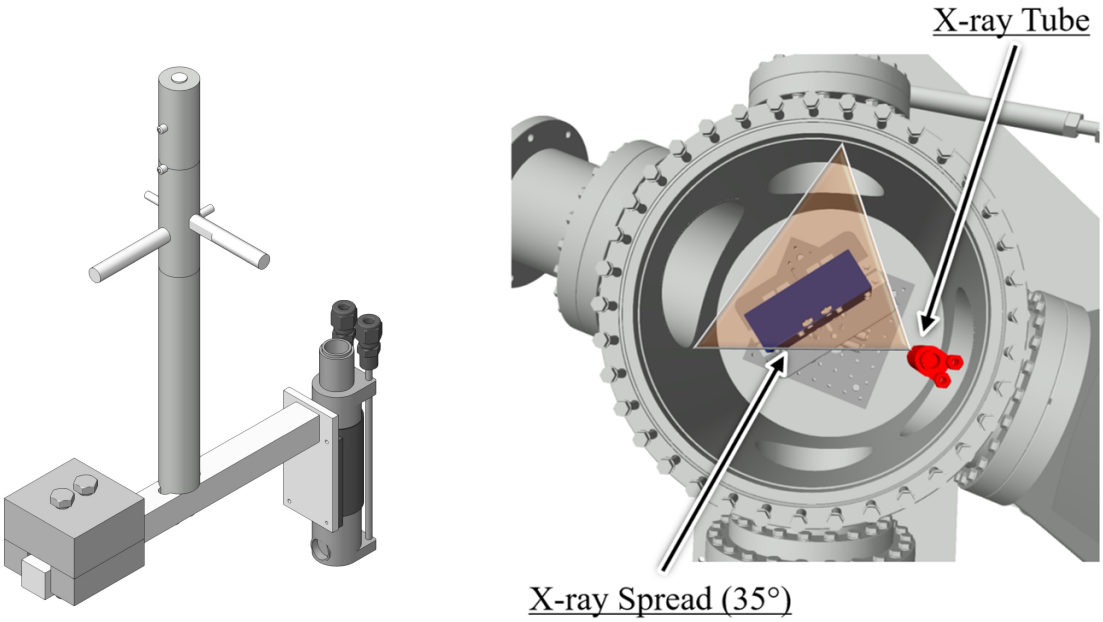

(a) Assembled Design (b) X-ray tube placement

Figure 2.6: Assembled calibration design along with the placement of the x-ray tube in the crystal chamber

tube in position for the second crystal. In the stored position, the x-ray tube will be rotated behind the crystal and will not limit any current capabilities of the XICS system. Extra ports have been put on the top flange to allow the installation of a camera to insure the rotary system is functioning properly.

Fig. 2.8 shows the placement of the x-ray tube in relation to the crystal and the plasma. This top-mounted arrangement of the x-ray tube in the chamber holding the crystal allows convenient access for installation and maintenance of the wavelength calibration system.

2.3 Simulation & Modeling

2.3.1 X-ray Ray Tracing

In order to validate the calibration design, X-ray Imaging Crystal Spectrometer Ray Tracing (XICSRT) was developed as a tool to analyze and test the proposed design. XICSRT is an object-oriented, ray tracing code written in Python that simulates the x-ray source, the spherical crystal, and the detector. Defining an arbitrary source, such as an isotropically emitting plasma or a x-ray tube emitting in a cone, the x-rays of a chosen wavelength are tracked as they travel

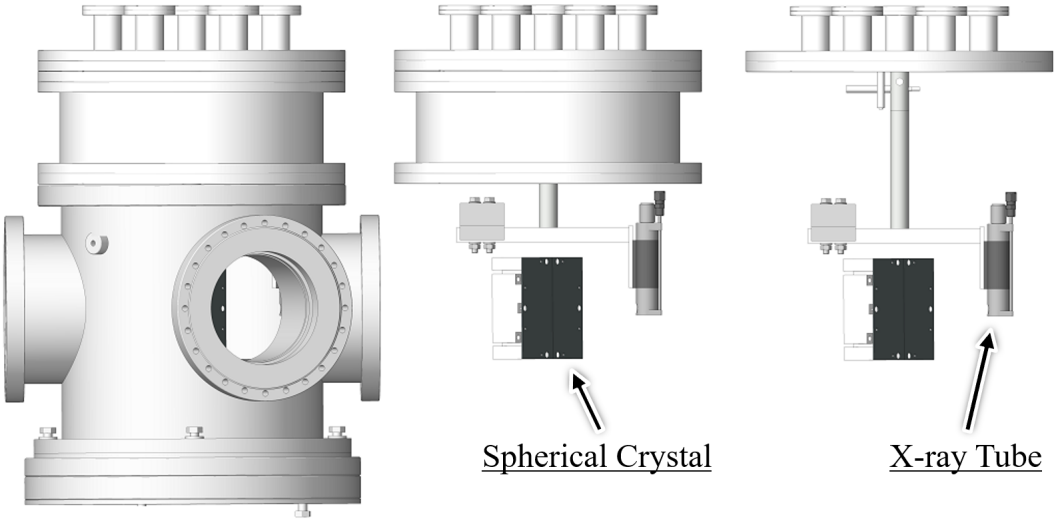

Figure 2.7: The placement of the x-ray tube with respect to the crystal chamber

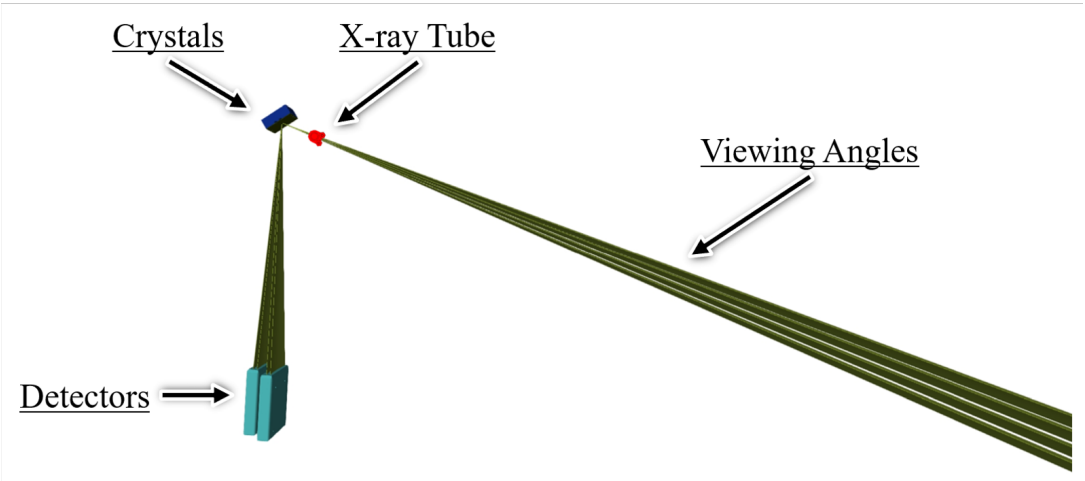

Figure 2.8: X-ray tube placement compared to the viewing angles of XICS

through the system. Fig. 2.9 shows an example of XICS-RT being used for the XICS system on W7-X.

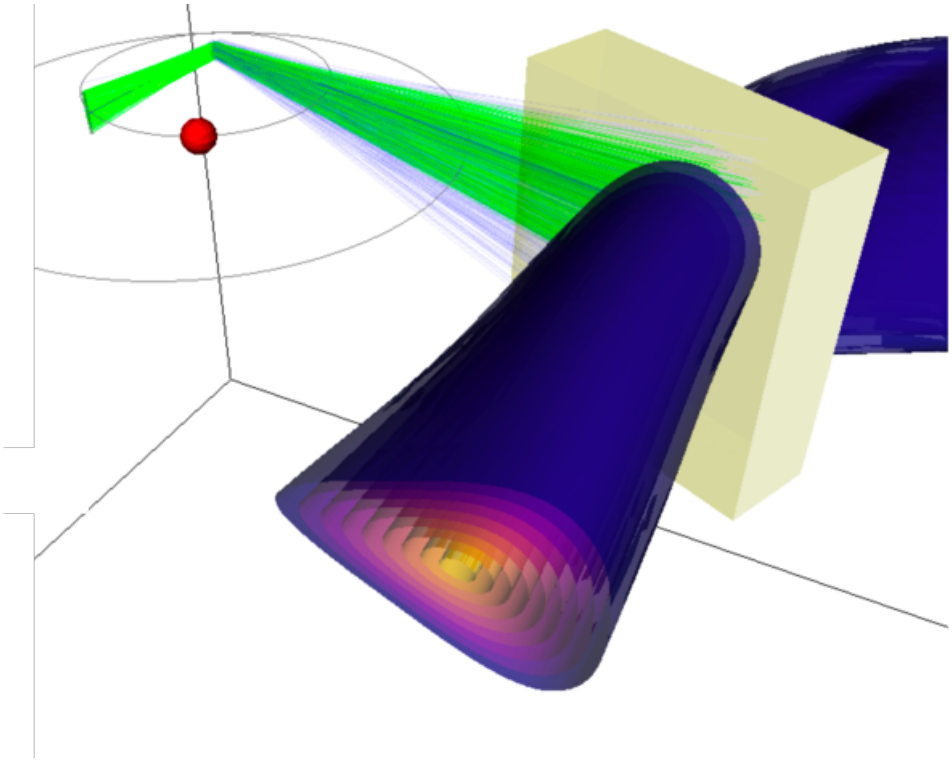

Figure 2.9: Example implementation of XICSRT to a W7-X plasma (flux surfaces shown). The rays are propagated from the plasma, to the crystal, and through to the detector. (8).

As the x-rays impinge on the crystal, only those that satisfy Bragg's Law (Eq. 2.1) and the crystal specific characteristics, such as the rocking curve which is the natural dispersion due to imperfection in the crystal lattice, are allowed to propagate further. The detector, with simulated pixels, counts all incident rays and outputs an image file. In recent years, XICSRT has been expanded to use any arbitrarily defined crystal geometry and x-ray source with results confirmed with SHADOW3 (21). XICSRT has been used to enhance and develop x-ray crystal spectrometers for ITER (22) and NIF (23) and further improvement of the system at W7-x (8). XICSRT has become publicly available and can be downloaded with documentation at https://pypi.org/project/xicsrt/ (24; 25).

Using XICSRT with the actual geometry of the XICS system on W7-X coupled with the physical characteristics of the x-ray source, the available configuration space for positioning the x-ray tube such that the detectors are illuminated over the full vertical extent was determined.

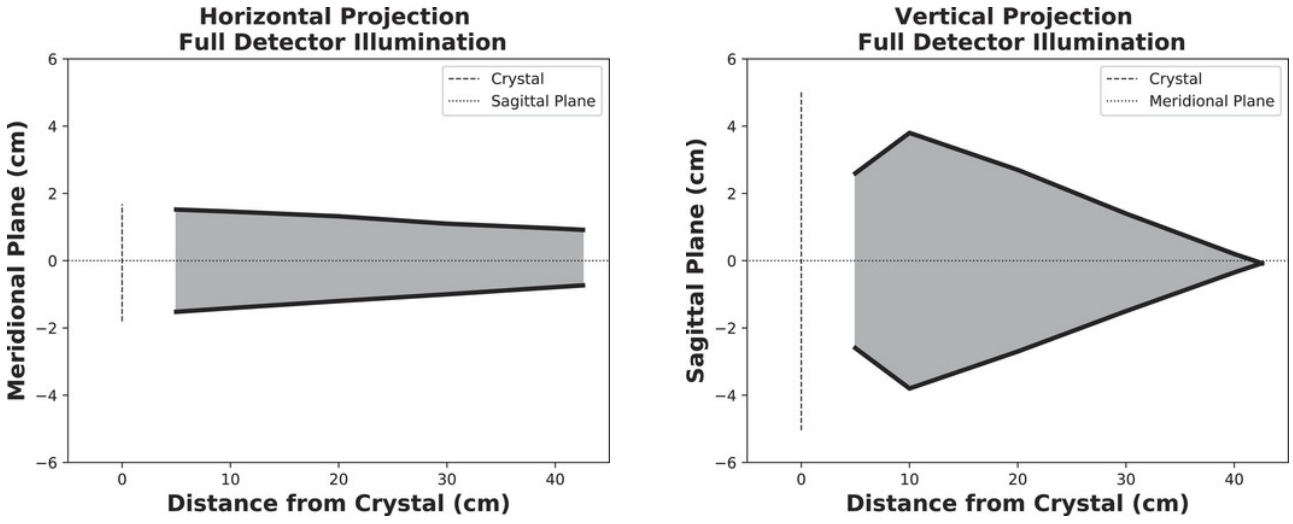

(a) (b)

Figure 2.10: Horizontal projection of the configuration envelope (a). Vertical projection of the configuration envelope (b).

Fig. 2.10 shows the horizontal (a) and vertical (b) projections of the configuration space. If the x-ray source is positioned anywhere inside this configuration envelope and directed at the spherical crystal, then the full vertical extent of the detector will be illuminated. The optimal position is along the center of the configuration envelopes.

2.3.2 Analytical Formulation

XICSRT was verified using an analytic formulation that was developed to understand the geometry of a spherical crystal x-ray spectrometer. Fig. 2.11 shows this geometry. The two circles represent spheres having radii of R and $R\cos\theta_{\mathrm{B}}$ with R being the radius of curvature of the spherical crystal and θ_B the Bragg Angle. The crystal's width extends from C_- to C_+ with C_0 being the center of the crystal. M is the center of curvature of the crystal, and P is the location of the planar detector. The rays, which are incident on the center of the crystal and diffracted according to the Bragg angle θ_{B} must be tangential to the sphere with radius $R\,cos\,\theta_{\mathrm{B}}$. In order to satisfy the Bragg condition at the center of the spherical crystal, the source must lie on the $\overline{C_0Q_0}$ line. For practical considerations, the source is inside the Q_0 position at some arbitrary Q_- location.

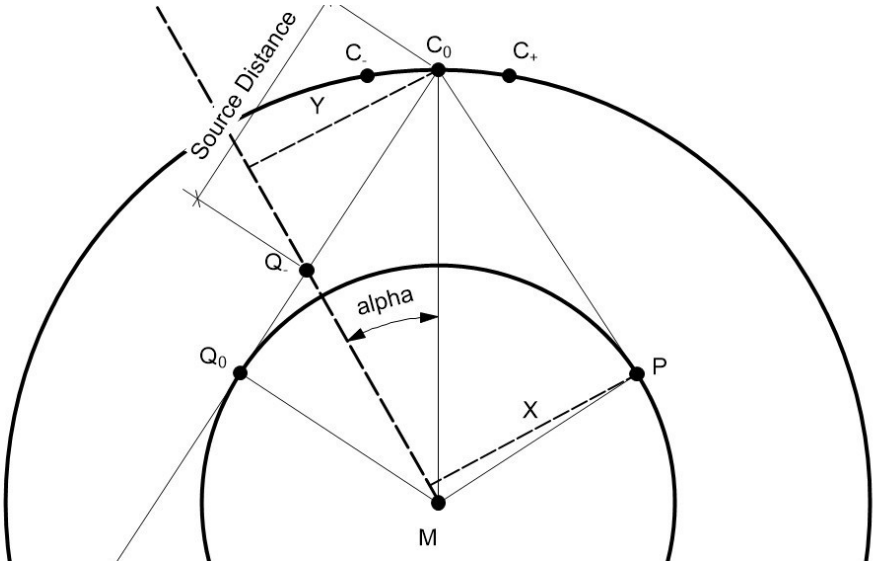

Figure 2.11: Two-dimensional projection (top down view) of the XICS geometry.

With the source located inside the focal lengths of the crystal, the resulting image on the detector is produced from a virtual image. The location of the virtual image (not shown in Fig. 2.11) is at the intersection of the lines $\overline{Q\_M}$ and $\overline{PC_0}$. With this virtual image, a characterization of the detector image can be made by rotating all rays which satisfy the Bragg angle about the $\overline{Q\_M}$ axis.

Using the actual geometry of XICS, Fig. 2.12 shows the comparison of XICSRT to the analytical formulation. In Fig. 2.12, the vertical extent of the detector refers to the height of the planar detector that is illuminated by an x-ray source positioned at the corresponding location. Any vertical extent above the solid horizontal line (the physical height of the detector) corresponds to the full illumination of all spatial channels on the detector. The plateau region in Fig. 2.12 resulted from the finite width of the detector plane; the decaying region resulted from the fixed spread of the x-ray source (chosen to match the actual x-ray tube). Good agreement was found between XICSRT and the analytical formulation.

2.4 Experimental Testing

2.4.1 Direct Illumination

Testing of the calibration design has been completed at the Plasma Science and Fusion Center (Cambridge, MA) using the High Resolution X-ray Crystal Imaging Spectrometer with Spatial

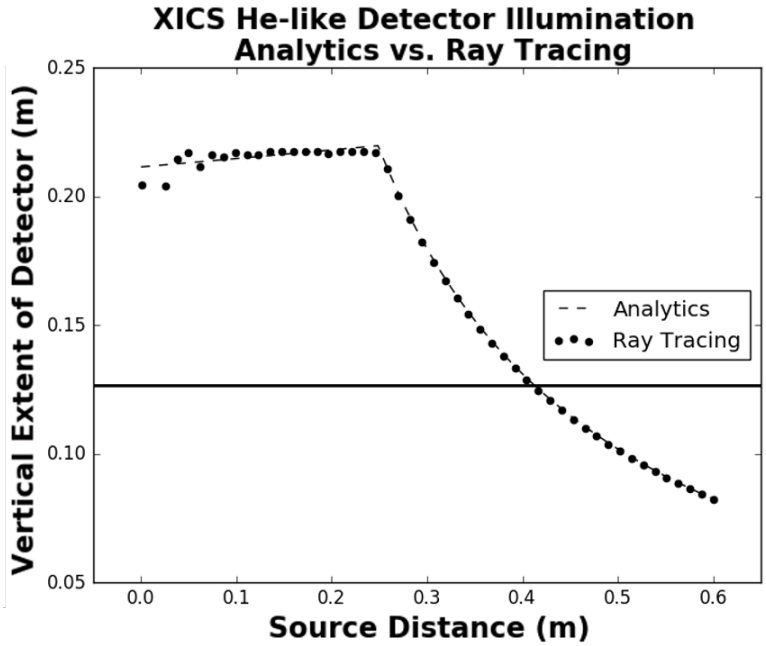

Figure 2.12: Comparison of XICS-RT and the analytical formulation.

Resolution (HIREXSR, an almost identical system to XICS)(12). An x-ray tube (same model as one in the calibration design) with a Cadmium anode at 9.5 kV, 0.5 mA was positioned in front of the diffracting crystal at a distance of 4 cm with the angles satisfying the Bragg condition. With an exposure of 500s (acceptable for wavelength calibrations), full illumination of the two working modules of the detector was found.

Fig. 2.13(a) shows the resulting image from the central module of the detector produced by the Cadmium Lα_1 and Cadmium Lα_2 lines. Fig. 2.13(b) is the XICSRT produced image with simulated x-ray source having the same spread, size, and distance from the spherical crystal as the actual experiment but only including the Cd Lα_1 line in the simulation. Fig. 2.13(c) illustrates the agreement between the two by plotting the vertically-centered, binned rows from each image.

2.4.2 Indirect Illumination

In an attempt to identify possible calibration schemes, several indirect illumination calibration methods, were investigated. These methods were motivated in order to provide a calibration source that would use the full crystal surface, mimicking the plasma. For the first test, a Cu

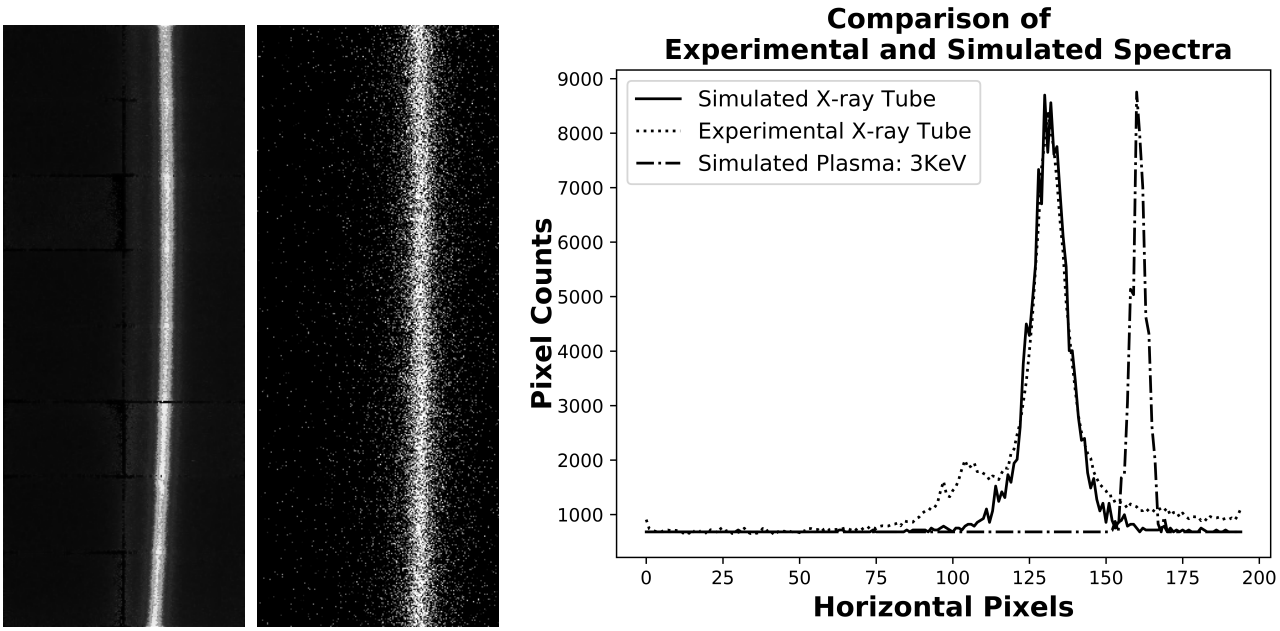

(a) (b) (c)

Figure 2.13: (a) Experimental and (b) Simulated images of the x-ray tube with profiles compared with simulated plasma light in (c).

x-ray tube was used to illuminate a thick Cadmium sheet in an attempt to excite reflection x-ray fluorescence. With a 2 mm thick Cadmium sheet placed approximate 30 cm in front of the crystal, the x-ray tube was positioned to the side of the crystal and aimed at the Cadmium sheet such that the illuminated area was in the line of sight of the full crystal. Next, transmission x-ray fluorescence was attempted with a thin 2 μm Cadmium foil, placed 2 cm from the crystal between the crystal and the Cu x-ray source. Finally, direct x-ray reflection of a Cd x-ray tube was tested using Cadmium, steel, and carbon sheets as the reflecting surfaces. All attempted methods failed to produce any detectable Cadmium lines on the detector, even after integration times of many hours. The lack of detectable x-ray emission is likely attributable to very small fluorescence yields. The indirect calibration methods were abandoned in favor of direct illumination of the spherical crystal by the x-ray tube as described in this chapter.

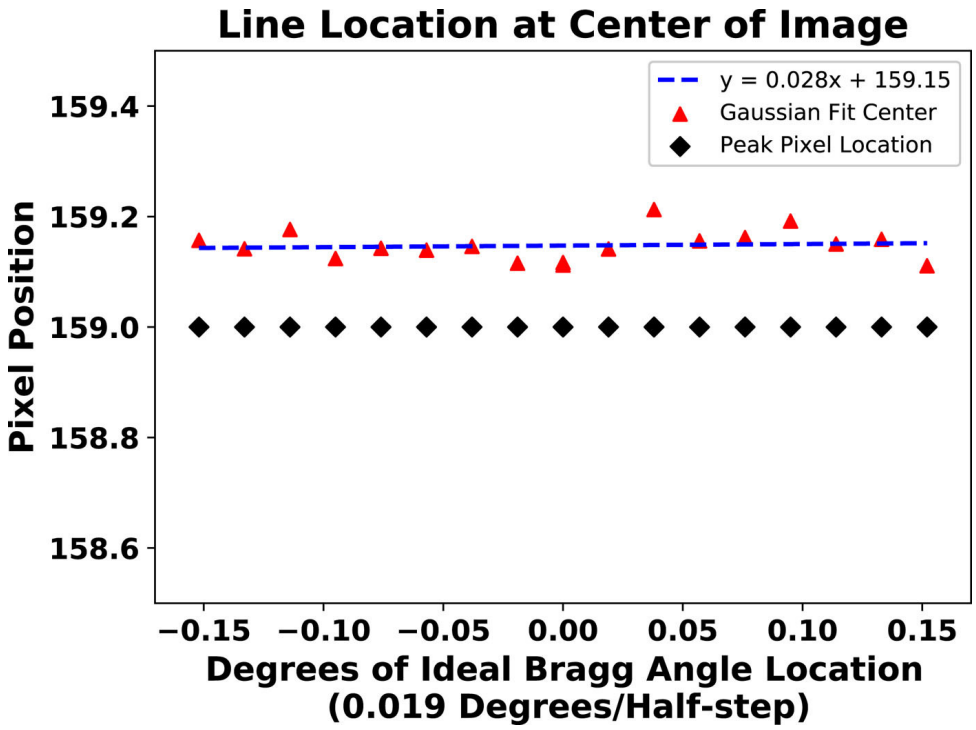

Figure 2.14: The impact of the x-ray tube placement on the pixel position of the calibration spectral line.

2.5 Wavelength Calibration Accuracy

The wavelength calibration accuracy of this design is limited by the random and systematic errors present in the system. The first random error in the wavelength calibration is the positioning of the x-ray tube at the optimal Bragg angle location which is dependent upon the rotary feedthrough. Fig. 2.14, the results of a positioning test using XICSRT, shows the change in position of the spectral lines (both the peak pixel location as well as a Gaussian fit pixel location) with a change in the angular rotation of the rotary feedthrough. Using the slope of the line fit to the Gaussian fit pixel location, the half-step of the rotary feedthrough (0.0019°) corresponds to a spectral shift of 2×10^{-7} Å (0.0005 pixels). Another random error is the ability to fit the spectral lines of the data. From the experimental testing with a 500 s exposure, the fitting error in the location of the calibration line is 1.5×10^{-7} Å (0.0004 pixels). The third possible random error is thermal expansion of the crystal or support system during the calibration exposure time. This limits the maximum integration time that can be used during the calibration, and can

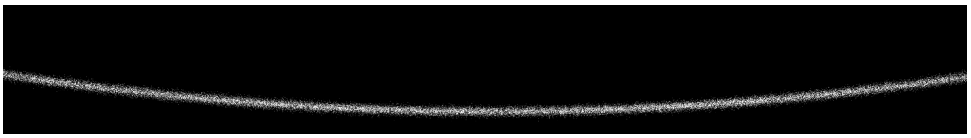

Figure 2.15: XICSRT produced image of the principle Ar^{16+} line of the plasma.

be potentially mitigated through characterization of the thermal effects on spectral line shifts coupled with precise temperature measurements.

The first systematic error to be quantified is the precision of the wavelength of the Cadmium lines ($L\alpha$ and $L\beta$) to be used for calibration. A literature study produces the most precise measurements to be 3.95635 ± 0.00004 Å and 3.73823 ± 0.00004 Å respectively (26). Two additional systematic errors arise because the x-ray tube is much smaller than the plasma and much closer, meaning only a fraction of the crystal will be used to diffract the calibration x-rays (compared to the plasma light using the full crystal). First, this difference will produce a change in the shape of the spectral lines. Second, depending on the location of the x-ray tube, a spectral line shift will also occur. Both of these systematic errors will be modeled using XICSRT. A high quality correction is expected; however, the final accuracy of this procedure will depend on our ability to accurately characterize the extent and angular spread of the x-ray source, as well as the rocking curve of the crystal. Fig. 2.15 demonstrates XICSRT's ability to produce plasma spectra (image has been rotated for this paper). This image was generated using a slab Ar^{16+} plasma (only the W-line simulated) at 5 KeV placed at the distance of 3.5m from the crystal. Given an absolute position accuracy of 1.5 mm (estimated value based on available remote measuring methods for the x-ray tube location relative to the crystal center), an absolute wavelength accuracy of 1×10^{-5} Å (1 km/s) is achievable. The future addition of a collimating slit may allow an in-situ calibration of the position of the x-ray tube with respect to the crystal edges, allowing a significant improvement in the absolute calibration.

2.6 Summary

A wavelength calibration system for x-ray imaging crystal spectrometers using direct illumination of the spherical diffracting crystal has been developed, tested, and designed for XICS on W7-X. This system will provide a wavelength calibration across the whole detector with

very high accuracy (limited mainly by integration time), but with a single remaining systematic offset. The random error in the measurement is estimated to be 3×10^{-7} Å (50 m/s) with a systematic error of 1×10^{-5} Å (1 km/s). This greatly improves the ability to measure perpendicular flow profiles to high accuracy, and will allow, for the first time on W7-X, parallel flow velocities to be simultaneously measured up to the larger systematic accuracy. Future improvements of the systematic accuracy are expected from future planned improvements in determination of the absolute location of the x-ray source and cross calibration with other diagnostics. In conjunction with the new calibration system, XICSRT, a x-ray ray tracing code in Python, has been developed and released to the public. XICSRT has already been used for development and enhancement of XICS systems for ITER, NIF, and W7-X.

Acknowledgements

Research supported by the U.S. DOE under Contract No. DE-AC02-09CH11466 with Princeton University. This work has been carried out within the framework of the EUROfusion Consortium and has received funding from the Euratom research and training programme 2014-2018 under grant agreement No 633053. The views and opinions expressed herein do not necessarily reflect those of the European Commission. We thank MIT PSFC for the use of their facilities in testing the calibration schemes.

References

[1] C. Beidler, G. Grieger, F. Herrnegger, E. Harmeyer, J. Kisslinger, W. Lotz, H. Maassberg, P. Merkel, J. Nührenberg, F. Rau, J. Sapper, F. Sardei, R. Scardovelli, A. Schlüter, and H. Wobig, "Physics and engineering design for wendelstein vii-x," *Fusion Technology*, vol. 17, no. 1, pp. 148–168, 1990.

[2] T. Sunn Pedersen, A. Dinklage, Y. Turkin, R. Wolf, S. Bozhenkov, J. Geiger, G. Fuchert, H.-S. Bosch, K. Rahbarnia, H. Thomsen, U. Neuner, T. Klinger, A. Langenberg, H. Trimiño Mora, P. Kornejew, J. Knauer, M. Hirsch, and N. Pablant, "Key results from

the first plasma operation phase and outlook for future performance in wendelstein 7-x," *Physics of Plasmas*, vol. 24, no. 5, p. 055503, 2017.

[3] A. Langenberg, N. Pablant, O. Marchuk, D. Zhang, J. Alonso, R. Burhenn, J. Svensson, P. Valson, D. Gates, M. Beurskens, and R. W. and, "Argon impurity transport studies at wendelstein 7-x using x-ray imaging spectrometer measurements," *Nuclear Fusion*, vol. 57, p. 086013, jun 2017.

[4] B. Geiger, T. Wegner, C. Beidler, R. Burhenn, B. Buttenschön, R. Dux, A. Langenberg, N. Pablant, T. Pütterich, Y. Turkin, T. Windisch, V. Winters, M. Beurskens, C. Biedermann, K. Brunner, G. Cseh, H. Damm, F. Effenberg, G. Fuchert, O. Grulke, J. Harris, C. Killer, J. Knauer, G. Kocsis, A. Krämer-Flecken, T. Kremeyer, M. Krychowiak, O. Marchuk, D. Nicolai, K. Rahbarnia, G. Satheeswaran, J. Schilling, O. Schmitz, T. Schröder, T. Szepesi, H. Thomsen, H. T. Mora, P. Traverso, and D. Z. and, "Observation of anomalous impurity transport during low-density experiments in w7-x with laser blow-off injections of iron," *Nuclear Fusion*, vol. 59, p. 046009, feb 2019.

[5] D. Clery, "Twisted logic," *Science*, vol. 350, no. 6259, pp. 369–371, 2015.

[6] N. A. Pablant, L. Delgado-Aparicio, M. Bitter, S. Brandstetter, E. Eikenberry, R. Ellis, K. W. Hill, P. Hofer, and M. Schneebeli, "Novel energy resolving x-ray pinhole camera on alcator c-mod," *Review of Scientific Instruments*, vol. 83, no. 10, p. 10E526, 2012.

[7] N. Pablant, A. Langenberg, A. Alonso, J. Baldzuhn, C. Beidler, S. Bozhenkov, R. Burhenn, K. Brunner, A. Dinklage, G. Fuchert, O. Ford, D. Gates, J. Geiger, M. Hirsch, U. Höfel, Y. Kazakov, J. Knauer, M. Krychowiak, H. Laqua, M. Landreman, S. Lazerson, H. Maaßberg, O. Marchuck, A. Mollen, E. Pasch, A. Pavone, S. Satake, T. Schröder, H. Smith, J. Svensson, P. Traverso, Y. Turkin, J. Velasco, A. von Stechow, F. Warmer, G. Weir, R. Wolf, and D. Z. and, "Investigation of the neoclassical ambipolar electric field in ion-root plasmas on w7-x," *Nuclear Fusion*, vol. 60, p. 036021, feb 2020.

[8] N. A. Pablant, A. Langenberg, J. A. Alonso, M. Bitter, S. A. Bozhenkov, O. P. Ford, K. W. Hill, J. Kring, O. Marchuck, J. Svensson, P. Traverso, T. Windisch, and Y. Yakusevitch, "Correction and verification of x-ray imaging crystal spectrometer analysis on wendelstein 7-x through x-ray ray tracing," *Review of Scientific Instruments*, vol. 92, no. 4, p. 043530, 2021.

[9] J. Kring, N. Pablant, A. Langenberg, J. Rice, L. Delgado-Aparicio, D. Maurer, P. Traverso, M. Bitter, K. Hill, and M. Reinke, "In situ wavelength calibration system for the x-ray imaging crystal spectrometer (xics) on w7-x," *Review of Scientific Instruments*, vol. 89, no. 10, p. 10F107, 2018.

[10] N. P. *et al. 41st EPS Conference on Plasma Physics*, vol. 38F, p. P1.076, 2014.

[11] N. A. P. *et al.*, "Layout and results from the initial operation of the high-resolution x-ray imaging crystal spectrometer on the large helical device," *Review of Scientific Instruments*, vol. 83, no. 8, p. 083506, 2012.

[12] A. I.-C. *et al.*, "Spatially resolved high resolution x-ray spectroscopy for magnetically confined fusion plasmas (invited)," *Review of Scientific Instruments*, vol. 79, no. 10, p. 10E302, 2008.

[13] B. L. *et al.*, "Measurement of helium-like and hydrogen-like argon spectra using double-crystal x-ray spectrometers on east," *Review of Scientific Instruments*, vol. 87, no. 11, p. 11E326, 2016.

[14] S. G. Lee, J. G. Bak, U. W. Nam, M. K. Moon, and J. K. Cheon, "Development of advanced x-ray imaging crystal spectrometer utilizing a large area segmented proportional counter for kstar," *Review of Scientific Instruments*, vol. 78, no. 6, p. 063504, 2007.

[15] J. M. *et al.*, "Multi-energy x-ray detector calibration for te and impurity density (nz) measurements of mcf plasmas," *Review of Scientific Instruments*, vol. 87, no. 11, p. 11E320, 2016.

[16] N. A. Pablant, A. Langenberg, A. Alonso, C. D. Beidler, M. Bitter, S. Bozhenkov, R. Burhenn, M. Beurskens, L. Delgado-Aparicio, A. Dinklage, G. Fuchert, D. Gates, J. Geiger, K. W. Hill, U. Höfel, M. Hirsch, J. Knauer, A. Krämer-Flecken, M. Landreman, S. Lazerson, H. Maaßberg, O. Marchuk, S. Massidda, G. H. Neilson, E. Pasch, S. Satake, J. Svennson, P. Traverso, Y. Turkin, P. Valson, J. L. Velasco, G. Weir, T. Windisch, R. C. Wolf, M. Yokoyama, and D. Zhang, "Core radial electric field and transport in wendelstein 7-x plasmas," *Physics of Plasmas*, vol. 25, no. 2, p. 022508, 2018.

[17] R. C. Wolf, A. Alonso, S. Äkäslompolo, J. Baldzuhn, M. Beurskens, C. D. Beidler, C. Biedermann, H.-S. Bosch, S. Bozhenkov, R. Brakel, H. Braune, S. Brezinsek, K.-J. Brunner, H. Damm, A. Dinklage, P. Drewelow, F. Effenberg, Y. Feng, O. Ford, G. Fuchert, Y. Gao, J. Geiger, O. Grulke, N. Harder, D. Hartmann, P. Helander, B. Heinemann, M. Hirsch, U. Höfel, C. Hopf, K. Ida, M. Isobe, M. W. Jakubowski, Y. O. Kazakov, C. Killer, T. Klinger, J. Knauer, R. König, M. Krychowiak, A. Langenberg, H. P. Laqua, S. Lazerson, P. McNeely, S. Marsen, N. Marushchenko, R. Nocentini, K. Ogawa, G. Orozco, M. Osakabe, M. Otte, N. Pablant, E. Pasch, A. Pavone, M. Porkolab, A. Puig Sitjes, K. Rahbarnia, R. Riedl, N. Rust, E. Scott, J. Schilling, R. Schroeder, T. Stange, A. von Stechow, E. Strumberger, T. Sunn Pedersen, J. Svensson, H. Thomson, Y. Turkin, L. Vano, T. Wauters, G. Wurden, M. Yoshinuma, M. Zanini, and D. Zhang, "Performance of wendelstein 7-x stellarator plasmas during the first divertor operation phase," *Physics of Plasmas*, vol. 26, no. 8, p. 082504, 2019.

[18] T. Klinger, T. Andreeva, S. Bozhenkov, C. Brandt, R. Burhenn, B. Buttenschön, G. Fuchert, B. Geiger, O. Grulke, H. Laqua, N. Pablant, K. Rahbarnia, T. Stange, A. von Stechow, N. Tamura, H. Thomsen, Y. Turkin, T. Wegner, I. Abramovic, S. Äkäslompolo, J. Alcuson, P. Aleynikov, K. Aleynikova, A. Ali, A. Alonso, G. Anda, E. Ascasibar, J. Bähner, S. Baek, M. Balden, J. Baldzuhn, M. Banduch, T. Barbui, W. Behr, C. Beidler, A. Benndorf, C. Biedermann, W. Biel, B. Blackwell, E. Blanco, M. Blatzheim, S. Ballinger, T. Bluhm, D. Böckenhoff, B. Böswirth, L.-G. Böttger, M. Borchardt, V. Borsuk, J. Boscary, H.-S. Bosch, M. Beurskens, R. Brakel, H. Brand, T. Bräuer, H. Braune,

S. Brezinsek, K.-J. Brunner, R. Bussiahn, V. Bykov, J. Cai, I. Calvo, B. Cannas, A. Cappa, A. Carls, D. Carralero, L. Carraro, B. Carvalho, F. Castejon, A. Charl, N. Chaudhary, D. Chauvin, F. Chernyshev, M. Cianciosa, R. Citarella, G. Claps, J. Coenen, M. Cole, M. Cole, F. Cordella, G. Cseh, A. Czarnecka, K. Czerski, M. Czerwinski, G. Czymek, A. da Molin, A. da Silva, H. Damm, A. de la Pena, S. Degenkolbe, C. Dhard, M. Dibon, A. Dinklage, T. Dittmar, M. Drevlak, P. Drewelow, P. Drews, F. Durodie, E. Edlund, P. van Eeten, F. Effenberg, G. Ehrke, S. Elgeti, M. Endler, D. Ennis, H. Esteban, T. Estrada, J. Fellinger, Y. Feng, E. Flom, H. Fernandes, W. Fietz, W. Figacz, J. Fontdecaba, O. Ford, T. Fornal, H. Frerichs, A. Freund, T. Funaba, A. Galkowski, G. Gantenbein, Y. Gao, J. G. Regaña, D. Gates, J. Geiger, V. Giannella, A. Gogoleva, B. Goncalves, A. Goriaev, D. Gradic, M. Grahl, J. Green, H. Greuner, A. Grosman, H. Grote, M. Gruca, C. Guerard, P. Hacker, X. Han, J. Harris, D. Hartmann, D. Hathiramani, B. Hein, B. Heinemann, P. Helander, S. Henneberg, M. Henkel, J. H. Sanchez, C. Hidalgo, M. Hirsch, K. Hollfeld, U. Höfel, A. Hölting, D. Höschen, M. Houry, J. Howard, X. Huang, Z. Huang, M. Hubeny, M. Huber, H. Hunger, K. Ida, T. Ilkei, S. Illy, B. Israeli, S. Jablonski, M. Jakubowski, J. Jelonnek, H. Jenzsch, T. Jesche, M. Jia, P. Junghanns, J. Kacmarczyk, J.-P. Kallmeyer, U. Kamionka, H. Kasahara, W. Kasparek, Y. Kazakov, N. Kenmochi, C. Killer, A. Kirschner, R. Kleiber, J. Knauer, M. Knaup, A. Knieps, T. Kobarg, G. Kocsis, F. Köchl, Y. Kolesnichenko, A. Könies, R. König, P. Kornejew, J.-P. Koschinsky, F. Köster, M. Krämer, R. Krampitz, A. Krämer-Flecken, N. Krawczyk, T. Kremeyer, J. Krom, M. Krychowiak, I. Ksiazek, M. Kubkowska, G. Kühner, T. Kurki-Suonio, P. Kurz, S. Kwak, M. Landreman, P. Lang, R. Lang, A. Langenberg, S. Langish, H. Laqua, R. Laube, S. Lazerson, C. Lechte, M. Lennartz, W. Leonhardt, C. Li, C. Li, Y. Li, Y. Liang, C. Linsmeier, S. Liu, J.-F. Lobsien, D. Loesser, J. L. Cisquella, J. Lore, A. Lorenz, M. Losert, A. Lücke, A. Lumsdaine, V. Lutsenko, H. Maaßberg, O. Marchuk, J. Matthew, S. Marsen, M. Marushchenko, S. Masuzaki, D. Maurer, M. Mayer, K. McCarthy, P. McNeely, A. Meier, D. Mellein, B. Mendelevitch, P. Mertens, D. Mikkelsen, A. Mishchenko, B. Missal, J. Mittelstaedt, T. Mizuuchi, A. Mollen, V. Moncada, T. Mönnich, T. Morisaki, D. Moseev, S. Murakami,

G. Náfrádi, M. Nagel, D. Naujoks, H. Neilson, R. Neu, O. Neubauer, U. Neuner, T. Ngo, D. Nicolai, S. Nielsen, H. Niemann, T. Nishizawa, R. Nocentini, C. Nührenberg, J. Nührenberg, S. Obermayer, G. Offermanns, K. Ogawa, J. Ölmanns, J. Ongena, J. Oosterbeek, G. Orozco, M. Otte, L. P. Rodriguez, N. Panadero, N. P. Alvarez, D. Papenfuß, S. Paqay, E. Pasch, A. Pavone, E. Pawelec, T. Pedersen, G. Pelka, V. Perseo, B. Peterson, D. Pilopp, S. Pingel, F. Pisano, B. Plaum, G. Plunk, P. Pölöskei, M. Porkolab, J. Proll, M.-E. Puiatti, A. P. Sitjes, F. Purps, M. Rack, S. Récsei, A. Reiman, F. Reimold, D. Reiter, F. Remppel, S. Renard, R. Riedl, J. Riemann, K. Risse, V. Rohde, H. Röhlinger, M. Romé, D. Rondeshagen, P. Rong, B. Roth, L. Rudischhauser, K. Rummel, T. Rummel, A. Runov, N. Rust, L. Ryc, S. Ryosuke, R. Sakamoto, M. Salewski, A. Samartsev, E. Sanchez, F. Sano, S. Satake, J. Schacht, G. Satheeswaran, F. Schauer, T. Scherer, J. Schilling, A. Schlaich, G. Schlisio, F. Schluck, K.-H. Schlüter, J. Schmitt, H. Schmitz, O. Schmitz, S. Schmuck, M. Schneider, W. Schneider, P. Scholz, R. Schrittwieser, M. Schröder, T. Schröder, R. Schroeder, H. Schumacher, B. Schweer, E. Scott, S. Sereda, B. Shanahan, M. Sibilia, P. Sinha, S. Sipliä, C. Slaby, M. Sleczka, H. Smith, W. Spiess, D. Spong, A. Spring, R. Stadler, M. Stejner, L. Stephey, U. Stridde, C. Suzuki, J. Svensson, V. Szabó, T. Szabolics, T. Szepesi, Z. Szökefalvi-Nagy, A. Tancetti, J. Terry, J. Thomas, M. Thumm, J. Travere, P. Traverso, J. Tretter, H. T. Mora, H. Tsuchiya, T. Tsujimura, S. Tulipán, B. Unterberg, I. Vakulchyk, S. Valet, L. Vano, B. van Milligen, A. van Vuuren, L. Vela, J.-L. Velasco, M. Vergote, M. Vervier, N. Vianello, H. Viebke, R. Vilbrandt, A. Vorköper, S. Wadle, F. Wagner, E. Wang, N. Wang, Z. Wang, F. Warmer, T. Wauters, L. Wegener, J. Weggen, Y. Wei, G. Weir, J. Wendorf, U. Wenzel, A. Werner, A. White, B. Wiegel, F. Wilde, T. Windisch, M. Winkler, A. Winter, V. Winters, S. Wolf, R. Wolf, A. Wright, G. Wurden, P. Xanthopoulos, H. Yamada, I. Yamada, R. Yasuhara, M. Yokoyama, M. Zanini, M. Zarnstorff, A. Zeitler, D. Zhang, H. Zhang, J. Zhu, M. Zilker, A. Zocco, S. Zoletnik, and M. Zuin, "Overview of first wendelstein 7-x high-performance operation," *Nuclear Fusion*, vol. 59, p. 112004, jun 2019.

[19] N. A. P. *et al.*, "Core radial electric field and transport in wendelstein 7-x plasmas," *Physics of Plasmas*, vol. 25, no. 2, p. 022508, 2018.

[20] L. D.-A. *et al.*, "Effects of thermal expansion of the crystal lattice on x-ray crystal spectrometers used for fusion research," *Plasma Physics and Controlled Fusion*, vol. 55, no. 12, p. 125011, 2013.

[21] M. Sánchez del Río, N. Canestrari, F. Jiang, and F. Cerrina, "Shadow3: A new version of the synchrotron x-ray optics modelling package," *Journal of synchrotron radiation*, vol. 18, pp. 708–16, 09 2011.

[22] Y. Yakusevitch, N. Pablant, J. Kring, Z. Cheng, and M. DeBock, "Poster: Simulated validation of the iter xrcs core using ray-tracing algorithm," in *62nd Annual Meeting of the APS Division of Plasma Physics*, November 2020.

[23] N. A. Pablant, M. Bitter, P. Efthimion, L. Gao, H. Hill, B. Kraus, J. Kring, M. MacDonald, N. Ose, Y. Ping, M. Schneider, S. Stoupin, and Y. Yakusevitch, "Design and expected performance of a variable-radii sinusoidal spiral x-ray spectrometer for the national ignition facility," *Review of Scientific Instruments*, vol. 92, no. 4, p. 043530, 2021.

[24] *XICSRT package*, 2021. https://pypi.org/project/xicsrt.

[25] *XICSRT sourcecode*, 2021. https://github.com/PrincetonUniversity/xicsrt.

[26] J. Bearden, "X-ray wavelengths," *Review of Modern Physics*, pp. 86–99, 1967.

Chapter 3

The Compact Toroidal Hybrid Experiment

3.1 Introduction

All of the plasma discharges used to study density limit disruptions in this work were obtained on the Compact Toroidal Hybrid (CTH) experiment at Auburn University. A photo of the CTH device is shown in Fig. 3.1. CTH is a low aspect ratio ($R_0/a_{\text{plasma}} \simeq 3.5$), low-beta ($\beta = 0.1\%$), five-field period torsatron that can operate as a traditional stellarator with ECRH heating or as a stellarator/tokamak hybrid with inductively generated plasma current.

Like all stellarators, the magnetic configuration of CTH lacks toroidal symmetry (or axisymmetry), but exhibits field-period symmetry in the toroidal direction, in which the magnetic configuration is repeated an integer number of times in the full toroidal circuit. The magnetic coil system is designed to create field-periodic magnetic flux surfaces, in which the set of points defining the magnetic flux surfaces have the following property (1):

$$\left[R\left(\Phi,\theta,\phi\right), Z\left(\Phi,\theta,\phi\right)\right] \iff \left[R\left(\Phi,\theta,\frac{2\pi n}{N}+\phi\right), Z\left(\Phi,\theta,\frac{2\pi n}{N}+\phi\right)\right] \tag{3.1}$$

Here the functions R and Z refer to the set of points on a given flux surface labeled by Φ, which is a radial-like coordinate that is typically the toroidal magnetic flux enclosed in a specific flux surface; $\Phi = \iint \vec{B}\cdot\hat{\phi}dA$. θ and ϕ are the poloidal and toroidal angles respectively with the number of field periods of CTH being $N = 5$. The coil configuration is also designed to enforce stellarator symmetry, so that the magnetic flux surfaces also exhibit the following property of

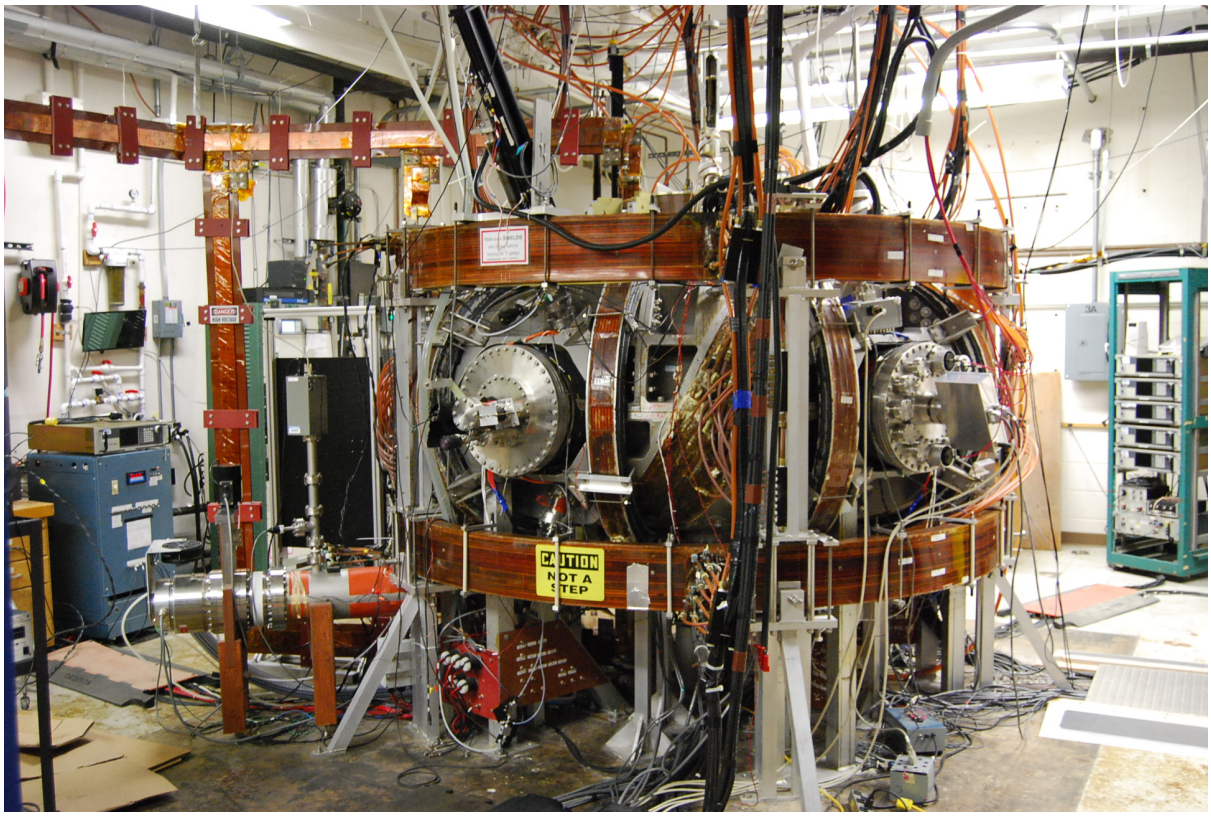

Figure 3.1: Photo of the Compact Toroidal Hybrid (CTH) experiment in its lab environment.

vertical symmetry:

$$[R(\Phi,\theta,\phi), Z(\Phi,\theta,\phi)] \iff [R(\Phi,\theta,-\phi), -Z(\Phi,\theta,\phi)] \tag{3.2}$$

CTH can operate as a pure stellarator but typically is operated as an unusual hybrid of a current-carrying tokamak and a stellarator. When operated as a pure stellarator, the magnetic rotational transform, which is necessary to generate closed, nested flux surfaces for plasma confinement, is provided by the external magnetic field coils alone. In hybrid operation, a central ohmic solenoid drives a toroidal current, I_{P}, within a pre-established ECRH (electron cyclotron resonance heating) stellarator plasma. By varying the currents in the external magnetic coils and the total plasma current, CTH is capable of investigating the effects of strong 3D shaping on MHD instabilities and disruptions that are driven by unstable plasma currents. Table. 3.1 shows several major parameters of the CTH design and plasmas.

Parameter	Dimension
Major radius (R_0)	0.75 m
Inner vacuum vessel radius (a_{vessel})	0.29 m
Toroidally averaged B-field along the magnetic axis (B_0)	0.64 T
Input ECRH heating	$\leq$ 15 kW
Input OH heating	100 kW
Average plasma minor radius (a_0)	0.2 m
Line-averaged density (n_{e})	$\leq 5.0 \times 10^{19} m^{-3}$
Electron temperature (T_{e})	$\leq$ 150 eV
Normalized Plasma Pressure (β)	$\approx 0.1\%$
Edge Vacuum Rotational Transform ι_{vac}	0.02 - 0.35
Edge Fractional Rotational Transform ι_{frac}	0.05 - 0.95

Table 3.1: Major parameters of the CTH design and operation

3.2 CTH Magnetic Configuration

The main magnet coils of CTH are shown in Fig. 3.2. They consist of six, independently-controlled, magnetic coil sets, which allow the vacuum magnetic rotational transform, magnetic shear, and vertical elongation to be varied. Also, the vacuum vessel and support structure is shown in gray.

Although the plasmas in CTH are non-axisymmetric, the vacuum vessel was chosen to be circular in both poloidal and toroidal cross section. It has a major radius of $R_0 = 0.75\,m$ and a minor radius of $a_{\text{vessel}} = 0.29\,m$. Unlike strongly-shaped vessels of stellarator configurations defined by a set of highly-optimized coils (3; 4; 5), the CTH vessel allows a large variety of plasma shapes and positions to be accommodated. The nested magnetic flux surfaces for an example CTH discharge are shown in Fig. 3.3 with the magnetic field strength handled by the color gradient (blue is low, yellow is high). The choice of a circular vessel was also based on economy. The wall of the Inconel 625 alloy vessel has an average thickness of $2.5\,mm$ and toroidal electric resistance of approximately $1\,m\Omega$. As a result, the inductive toroidal loop voltage of current-driven plasmas will also induce current within the vacuum vessel itself. The placement of all ports are designed to maintain the five-field periodicity and reduce the magnitude of symmetry-breaking errors from finite vacuum vessel currents. These finite vacuum

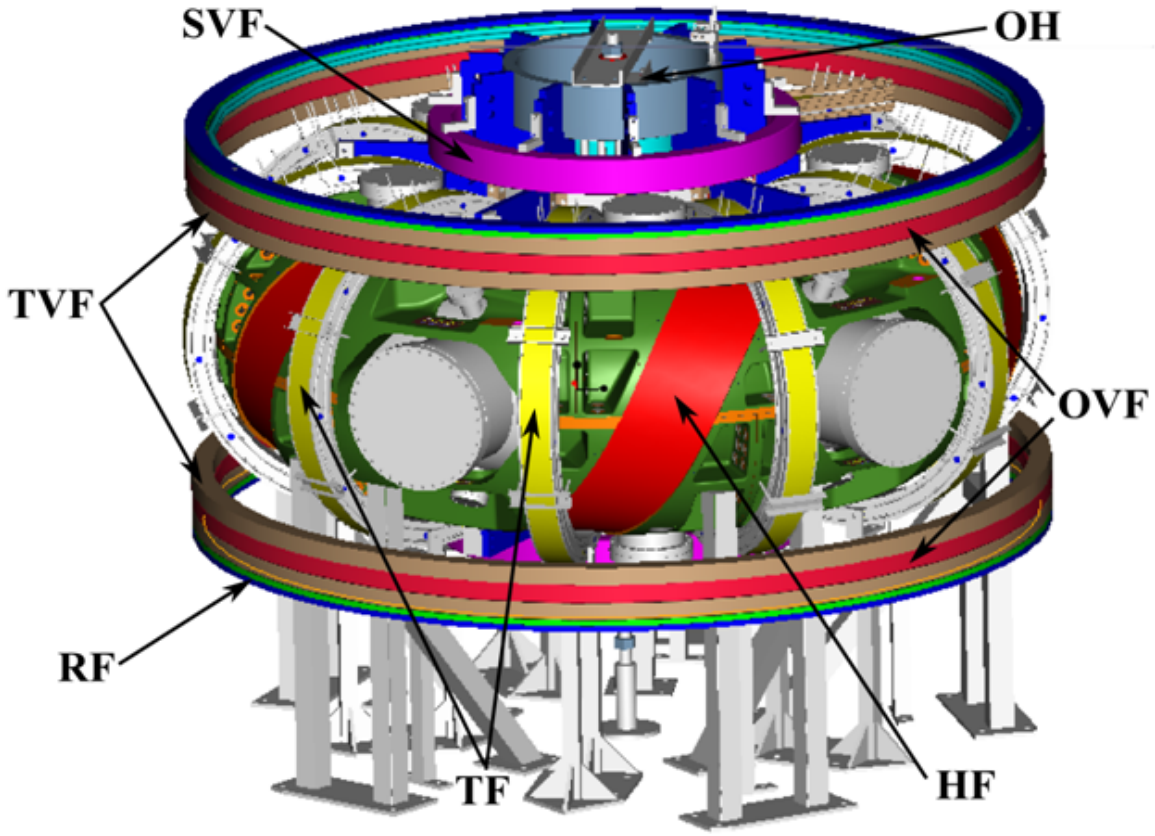

Figure 3.2: Magnet coils of the Compact Toroidal Hybrid: Helical field coil (HF) and main vertical field coils (OVF), connected in series, are shown in red. Additional poloidal field coils for trimming the vertical field (TVF) and radial field (RF) are shown in green and blue respectively. Auxiliary toroidal field (TF) coils are shown in yellow. The shaping vertical field coil (SVF) set for elongation and shear is shown in purple. The ohmic transformer solenoid and dedicated poloidal for ohmic flux expansion (OH) are indicated in green-blue. The vacuum vessel and support structure is shown in gray. Figure is reproduced from (2)

vessel currents or eddy currents are induced by the changing magnetic fluxes from the external coils and plasma current.

A single $\ell = 2$, $m = 5$ helical field coil (HF), consisting of 96 turns, is wound onto an aluminum frame that encloses the vacuum vessel. The coil makes two toroidal circuits (ℓ number) for every five poloidal circuits (m number) as it is wound around the vacuum vessel. The helical path followed by the center of the HF coil pack is defined in pseudo-toroidal coordinates (r, θ, ϕ) (6; 7). The winding law was selected by optimization with the IFT code (8) to maximize the volume of the region within the CTH vacuum vessel. Since the current in the HF

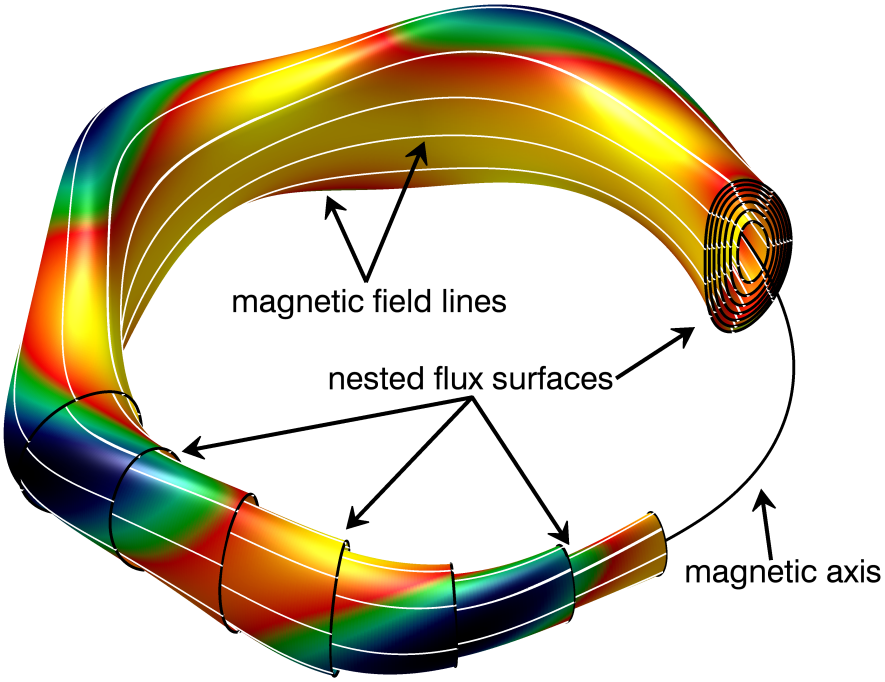

Figure 3.3: Nested magnetic flux surfaces on the Compact Toroidal Hybrid. The color gradient represents the magnetic field strength (blue is low, yellow is high) with some magnetic field lines in white. Reproduced from (2)

coil is unidirectional, the magnetic configuration of CTH is referred to as a torsatron within the class of stellarators.

The HF coil provides toroidal and poloidal components of the equilibrium helical field. In most torsatrons and CTH in particular, an additional poloidal/vertical field is required to produce a closed vacuum equilibrium within the volume of the vacuum vessel. The poloidal field coil set on CTH consists of four subsets:

1. The main vertical field (OVF) coils, electrically connected in series with the HF coil (and therefore with the same current as the HF coil), provides approximately 50% of the vertical field required for equilibrium.

2. A pair of trim vertical field (TVF) coils, is independently powered to further control the radial position of the plasma

3. A shaping vertical field (SVF) coil set, providing a quadrupole field, adjusts the vertical elongation as well as the magnetic shear of the plasma equilibrium.

4. A radial field (RF) coil set can shift the vertical position of the plasma and is typically used to maintain vertical stability during ohmic operation.

The total magnetic rotational transform (ι_{tot}) in CTH hybrid operation is produced by the external magnetic coil currents and the toroidal plasma current. As a proxy for the relative magnitude of the poloidal field due to the currents in the stellarator coils, we define a vacuum magnetic rotational transform ι_{vac} calculated from modeling the vacuum equilibrium present in absence of the plasma current. The total transform is then written as

$$\iota_{\mathrm{tot}} = \iota_{\mathrm{vac}} + \iota_{\mathrm{p}} \tag{3.3}$$

where ι_{p} reflects the contribution ascribed to the presence of the plasma current. The total and vacuum rotational transforms are computed with the VMEC (9) equilibrium code with the vacuum rotational transform being determined from reconstructions before plasma current is initiated, and the total rotational transform calculated during times when the plasma current is flowing. In practice, ι_{p} of a hybrid discharge is not a flux surface quantity and not calculable in VMEC, but serves as a measure of the relative contribution of the plasma current to the total rotational transform of the discharge. For comparison of CTH discharges to discharges on other experiments, We also define the relationship,

$$\iota_{\mathrm{frac}} = \iota_{\mathrm{vac}} / \iota_{\mathrm{tot}} \tag{3.4}$$

where the fractional rotational transform ι_{frac} is the ratio of the vacuum rotational transform to the total rotational transform. For a tokamak, $\iota_{\mathrm{frac}} = 0$; for a current free stellarator, $\iota_{\mathrm{frac}} = 1$. On CTH, the edge vacuum rotational transform can be varied from $\iota_{\mathrm{vac}} \simeq 0.02$ to $\iota_{\mathrm{vac}} \simeq 0.35$ with the use of auxiliary toroidal field coils. In current-carrying discharges, CTH can be operated such that the total rotational transform is dominated by the effect of the plasma current, with fractional transforms in the range $0.05 \leq \iota_{\mathrm{frac}} \leq 0.95$. The fractional transform

can be thought of as a indicator as to whether the discharge is more tokamak-like (for lower values) or more stellarator-like (for higher values).

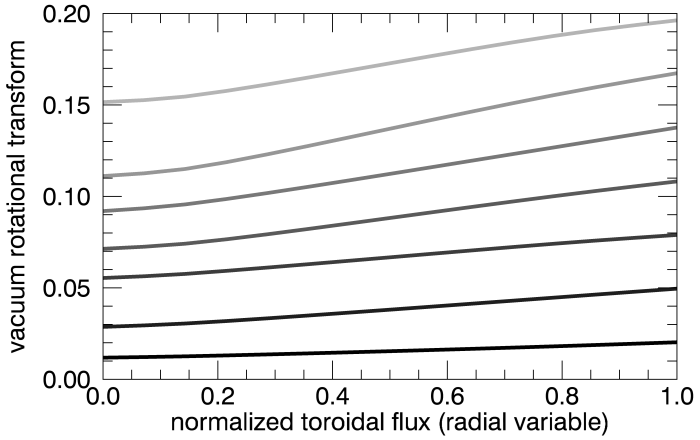

Figure 3.4: Vacuum rotational transform vs. radial-like coordinate Φ for several values of $I_{\mathbf{TF}}/I_{\mathbf{HF}}$. Positive values of $I_{\mathbf{TF}}/I_{\mathbf{HF}}$ correspond to the toroidal components of the TF and HF being parallel, negative to anti-parallel. The normalized toroidal flux is 1 at the last closed flux surface and 0 at the magnetic axis.

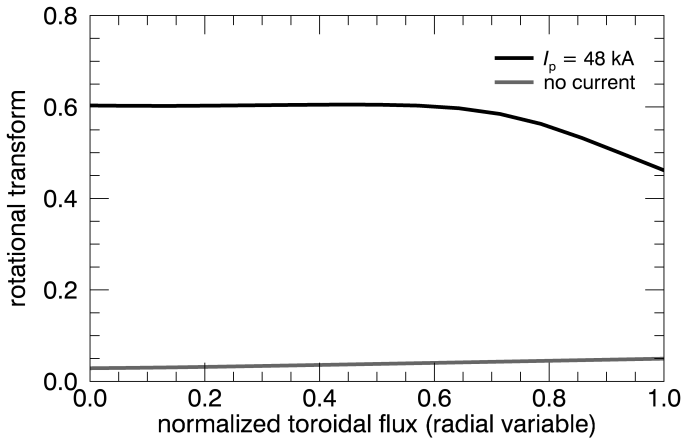

Figure 3.5: Toroidal plasma current substantially modifies the shape of the rotational transform profile. Bottom trace shows the monotonically increasing vacuum transform of ECRH only plasma, with vacuum rotational transform ~ 0.05. The top trace presents the changed total transform with 50kA of plasma current and total rotational transform ~ 0.45, showing a monotonically decreasing profile.

The vacuum rotational transform, ι_{vac}, can be varied with the use of ten auxiliary toroidal field (TF) coils (see Fig. 3.2) by adding to or subtracting from the toroidal field component

produced by HF coil. Various vacuum rotational transform radial profiles for different coil current ratios, $I_{\mathbf{TF}}/I_{\mathbf{HF}}$, are plotted in Fig. 3.4.

To operate as a hybrid tokamak/stellarator, a toroidal current is driven using the ohmic heating transformer within the pre-established ECRH plasma. The addition of plasma current substantially changes the transform profiles, as shown in Fig. 3.5.

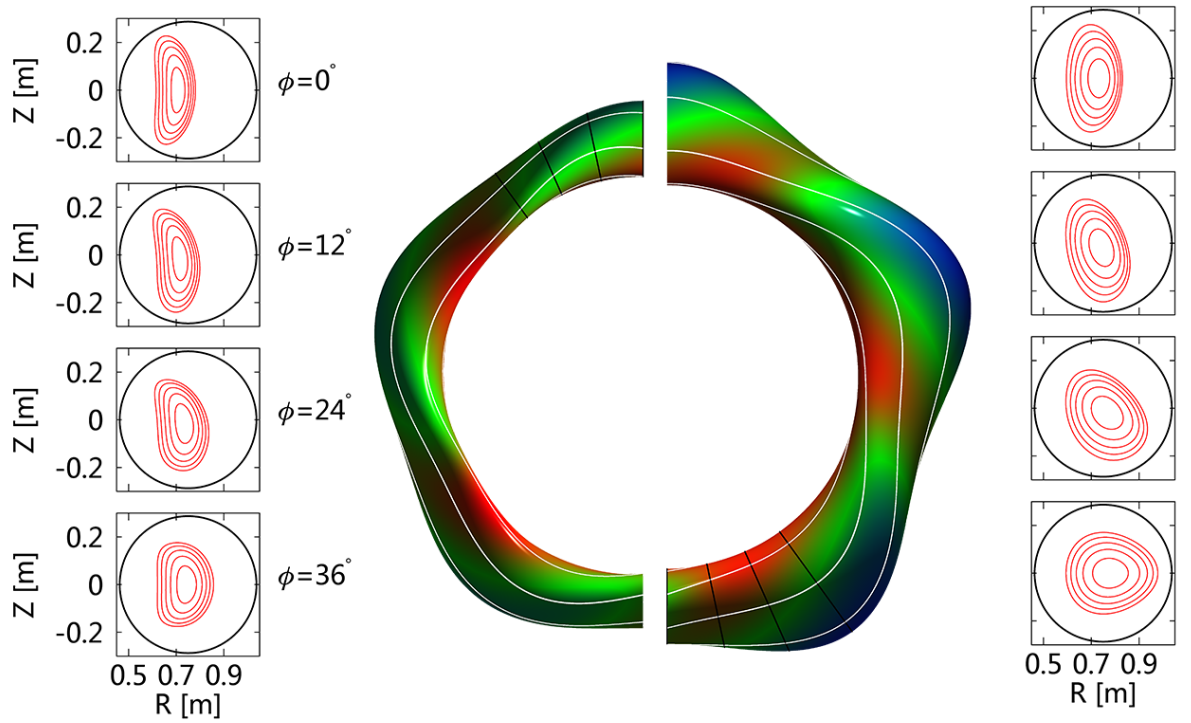

Figure 3.6: Poloidal cross-sections of magnetic flux surfaces and representations of the last closed flux surfaces of CTH plasmas without plasma current ($I_p = 0$)(left) and with $I_p = 53.6kA$. The color shading refers to magnetic field strength (blue lowest; red highest), and several field lines are indicated by white lines. Figure reproduced from (10).

In summary, the magnetic equilibria of CTH plasmas are predicted to be highly non-axisymmetric either with or without ohmic plasma current. The variation of the already non-axisymmetric magnetic flux surfaces with the inclusion of ohmic current can be seen in Fig. 3.6 where the shapes of the last closed flux surfaces are computed with VMEC. One half of a zero-current, ECRH-only plasma is depicted on the left side of the plot, along with poloidal cross-sections of flux surfaces at four different toroidal angles. The right side of the figure shows flux surfaces and plasma shape computed at a plasma current of $I_{\mathrm{p}} = 53.6kA$. While the poloidal cross-section of CTH discharges becomes less elliptical with the addition of driven

plasma current, the underlying toroidal $N = 5$ stellarator periodicity is enhanced. Thus even in hybrid discharges, the need for fully 3D computational tools for reconstruction remains clear.

3.3 CTH Diagnostics

Plasma diagnosis is a process that deduces properties of the state of plasma from experimental observations of physical processes and corresponding effects. Its principles are well discussed in numerous references (11; 12; 13), which set the foundation to understand experimental diagnostic data and to design and build new diagnostics. In this work, the plasma parameters of plasma shape, position, density, temperature, magnetic fluctuations as well soft x-ray (SXR) and bolometer emission, are important in performing equilibrium data reconstructions. A top view of CTH device and positions of various diagnostics available on CTH are shown in Fig. 3.7.

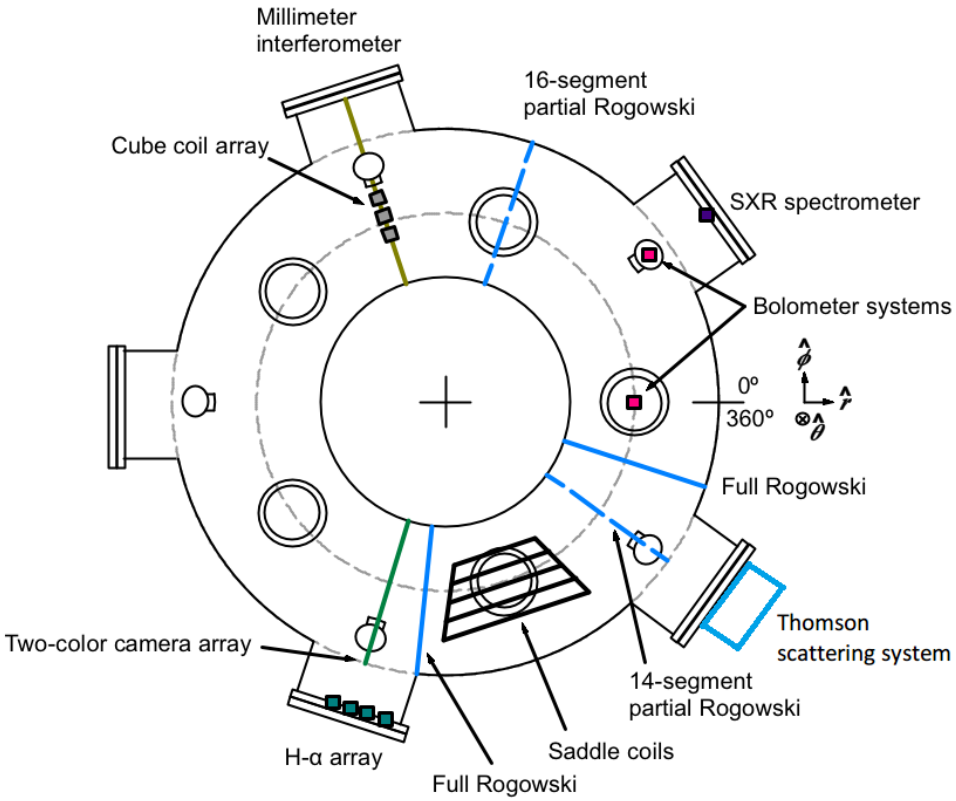

Figure 3.7: Top view of CTH device with a map showing various diagnostics available on CTH.

Magnetic diagnostics on CTH include full and segmented Rogowski coils, saddle-shaped flux loops, poloidal, toroidal, and radial magnetic pick up coils, and diamagnetic loops. A set of magnetic diagnostics that is important to the research done in this work is the B-dot probes assembled to detect poloidal and radial magnetic fields at the $\phi = 240$ toroidal location (14). Fig. 3.8 shows the 36 B-dot probe array or Mirnov coil on the lab bench (a) and mounted inside the vacuum vessel (b). On CTH, magnetic diagnostics are routinely used to determine plasma current, loop voltage, plasma shape and position (15), current distribution as well as magnetic fluctuations (14). They are used for equilibrium reconstructions together with other internal diagnostics such as the interferometer (16) and SXR cameras (17).

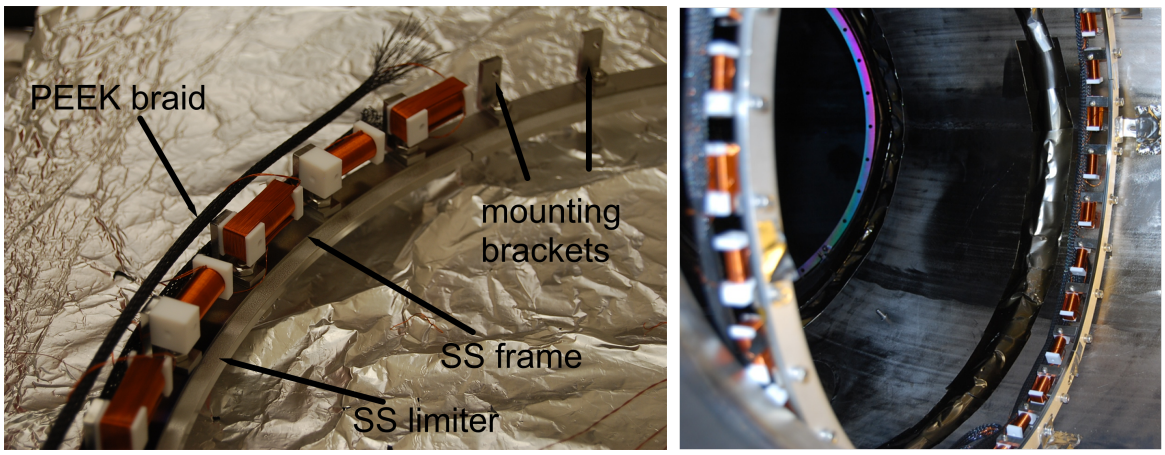

(a) (b)

Figure 3.8: (a) Photo of the partially assembled poloidal array on the bench. B-dot probes are mounted onto a SS 316 frame 1012 in diameter with L-shaped brackets also made out of SS 316 material. SS limiter 34 thick, prevents plasma from coming into contact with the frame. B-dot probes designed to measure both poloidal and radial field, and those designed to measure only the poloidal field are alternately positioned. The leads of the each probe is protected by a PEEK braid that runs along the circumference of the whole assembly. (b) The completed assembly is mounted inside the vacuum vessel in a plane nominally located at toroidal angle, $\Phi = 240°$. Figure reproduced from (18)

The line-integrated electron density is measured with a four-channel $1mm$ microwave interferometer system installed at $\phi = 108°$(16). One of the four chords passes through the horizontal mid-plane. Of the other three chords, one is oriented horizontally below the mid-plane with the two remaining chords positioned horizontally above the midplane.

CTH is also equipped with an extensive collection of emissivity diagnostics consisting of SXR cameras and bolometers. Three 20-channel two-color SXR cameras were developed and installed at the toroidal location of $\phi = 252°$ for electron temperature measurements (19) and SXR fluctuation analysis (20; 21). The arrangement of the system can be seen in Fig. 3.9 where the magnetic last closed flux surface (LCF) is shown in the solid red surface with several other flux surfaces plotted with the dashed red surfaces. In V3FIT reconstructions, the SXR cameras (part of the old two-color system) are routinely reconstructed as an internal diagnostic primarily to enhance the fitting of the radial distribution of the plasma current. For this application, the SXR signals are assumed to be flux surface quantities which has been proven elsewhere to be a safe assumption (22).

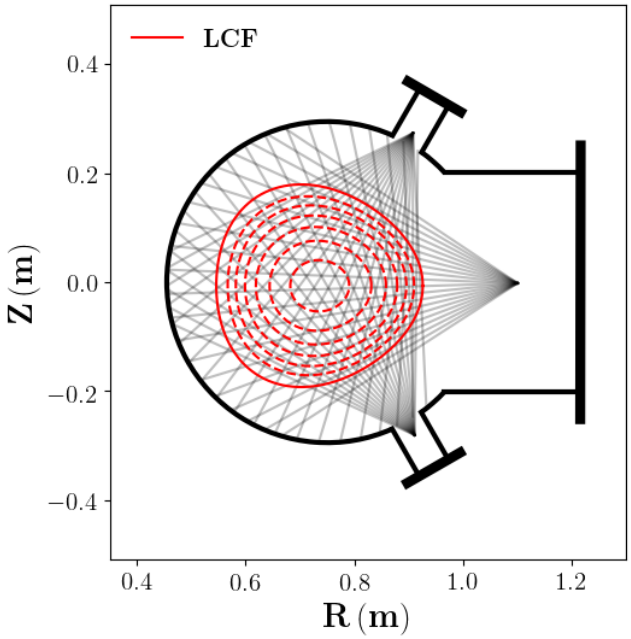

Figure 3.9: The orientation of the original two-color SXR cameras is shown with the 20 viewing chords of each camera plotted. The cameras are positioned at the $\theta = 0°, 60°$, and $300°$ poloidal positions. The last closed magnetic flux surface (LCF) is plotted (solid red) with additional magnetic flux surfaces (dashed red). The vacuum vessel is shown in black.

In an attempt to reinstall Beryllium filters ($1.8\,\mu m$ and $3.0\,\mu m$ thicknesses) on the two-color SXR system, several of the thick Beryllium filters were damaged in the process. Instead of waiting for more filters to arrive, we elected to operate the two-color system as a thin filter

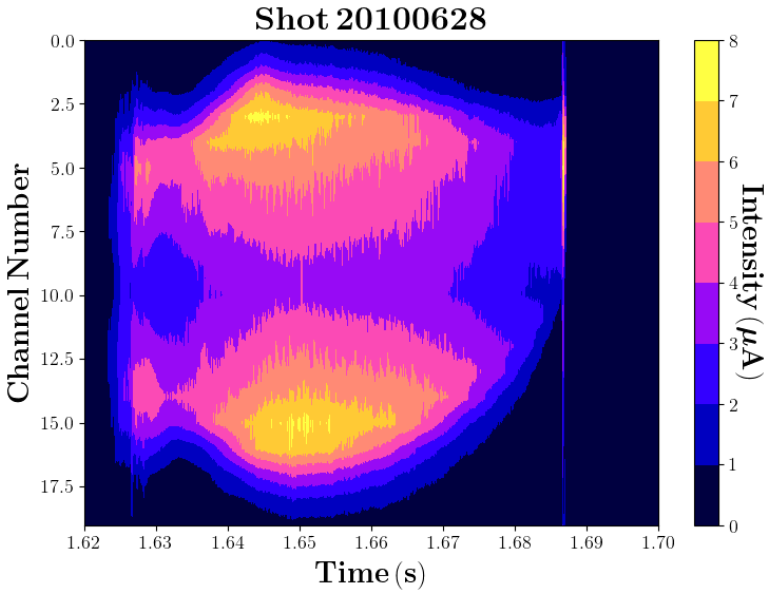

Figure 3.10: The raw midplane bolometer signals are plotted versus time for shot 20100628 which ends in a disruption. The bolometer signals are symmetric about the core of the plasma.

($1.8\,\mu m$ Beryllium) SXR camera and a bolometer (no filter) array. With the three bolometer array (midplane, top, and bottom), the overlap of the viewing chords (see Fig. 3.9) provides an opportunity to tomographically invert the measured emission from the plasma. Two additional bolometer-SXR systems are located at the $\phi = 36°$ with poloidal positions of $\theta = 14°$ and $\theta = 60°$.

For the new bolometer array, in contrast to the SXR cameras, the channels with the strongest signals are not the ones oriented to view the center of the plasma. This hollowness of the bolometer signals can be seen in Fig. 3.10 where the midplane bolometer, with up-down symmetric chords, is shown. The symmetry of the bolometer signals can be broken with high levels of gas puffing, typically needed for density limit disruptions on CTH. Fig. 3.11 shows back-to-back discharges where the programmed gas puffer settings are dramatically increased while holding all other control parameters constant. The increased gas puffing results in lower plasma currents, higher plasma densities, and stronger bolometer signals as well as an asymmetry in the bolometers as seen in Fig. 3.12.

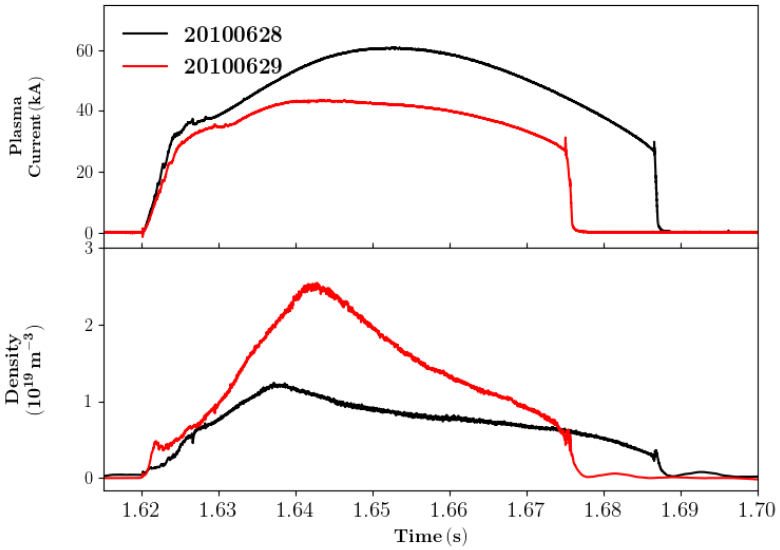

Figure 3.11: A comparison of the disrupting shots 20100628 and 20100629 that shows the affect of increasing the gas puffing without changing any other control parameters. The increased gas input results in higher densities and lower plasma currents as well as an asymmetry in the bolometer signals.

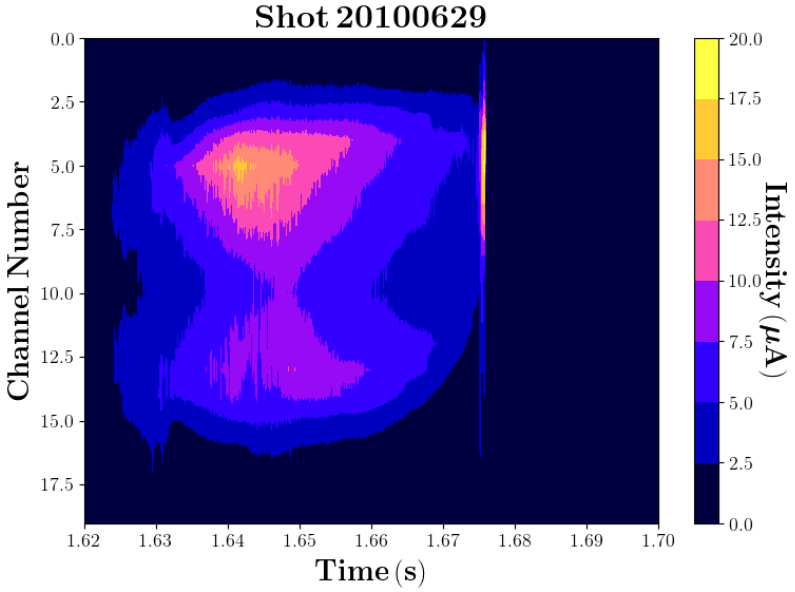

Figure 3.12: The raw midplane bolometer signals are plotted versus time for shot 20100629 which ends in a disruption. The bolometer signals are very asymmetric about the core of the plasma due to increased levels of gas puffing which results in higher plasma densities.

3.4 Equilibrium Reconstructions

The 3D equilibrium reconstructions performed for the work in this thesis were accomplished using V3FIT (23; 24) with the magnetic diagnostics, the thin-filter $1.8\,\mu m$ Be SXR cameras, and the interferometers. The V3FIT reconstructed flux surfaces provide the best estimate for chordal paths of the interferometer allowing for a proper calculation of the plasma density from the measured millimeter wave interferometer. Also, the magnetic flux surfaces serve as the starting point for all SXR and bolometer tomographic inversions as described in Chap. 4.

3.5 Density Limits on CTH

For this work, we routinely observed high density discharges by aggressively puffing deuterium or hydrogen on gas puffers 1 and 2. The best shots to illustrate this are shot 20100633 for low vacuum rotational transform and shot 20101331 for high vacuum rotational transform.

In general, the best approach was to start at low vacuum rotational transform and achieve density limits with care taken to not puff past the disruption (trial and error needed for this balance). Once that is achieved, then slowly vary the coil currents to increase the vacuum rotational transform as needed. This method produced consistent variation in the vacuum rotational transform and repeatable disrupting shots even at high vacuum rotational transform.

3.6 Summary

The Compact Toroidal Hybrid (CTH) is a low aspect ratio ($R_0/a_{\text{plasma}} \simeq 3.5$), low-beta ($\beta = 0.1\%$), five-field period torsatron that can operate as a traditional stellarator with ECRH heating or as a stellarator/tokamak hybrid with inductively generated plasma current. The maximum on-axis toroidal magnetic field is $B_0 = 0.7\,T$. The total rotational transform (ι_{tot}) in hybrid operation is produced by the external magnetic coil currents and the toroidal plasma current (see Eq. 3.3). On CTH, the vacuum rotational transform from the external magnetic coils can be varied from $\iota_{\text{vac}}(a_{\text{plasma}}) \simeq 0.02$ to $\iota_{\text{vac}}(a_{\text{plasma}}) \simeq 0.35$ with the use of auxiliary toroidal field coils. In current-carrying discharges, CTH can be operated such that the total rotational transform is dominated by the effect of the plasma current, with fractional transforms in the

range $0.05 \leq \iota_{\text{frac}} \leq 0.95$. The fractional transform can be thought of as a indicator as to whether the discharge is more tokamak-like (for lower values) or more stellarator-like (for higher values).

The magnetic equilibria in hybrid discharges are highly non-axisymmetric requiring fully three-dimenional equilibrium reconstruction for their interpretation. Three-dimensional equilibrium reconstructions are performed using V3FIT (23; 24). CTH is equipped with magnetic diagnostics (full and partial Rogowski coils, cube coils, Mirnov coils, and saddle coils), a double-pass four channel millimeter-wave interferometer (16), five 20-channel soft x-ray (SXR)/bolometer arrays (19), and SXR spectrometer. With the flexibility of its magnetic configuration, CTH has performed related experiments on low-q disruptions in hybrid plasmas (14), the impact of three-dimensional magnetic equilibriums on sawteething MHD modes (20; 21), the suppression of the vertical instabilities with applied vacuum transform (15), and, in this work, density limit disruptions.

References

[1] B. A. Stevenson, *3D Reconstruction of Plasma Equilibria using Magnetic Diagnostics on the Compact Toroidal Hybridtitle*. PhD thesis, Auburn University, 2011.

[2] J. L. Herfindal, *Control of Sawtooth Oscillation Dynamics using Externally Applied Stellarator Transform*. PhD thesis, Auburn University, 2016.

[3] F. Anderson, A. Almagri, D. Anderson, P. Matthews, J. Talmadge, and J. Shohet, "Helically symmetric experiment, (hsx) goals, design and status," *Fusion Techology*, vol. 27, no. 6, 1995.

[4] B. Nelson, L. Berry, A. Brooks, M. Cole, J. Chrzanowski, H.-M. Fan, P. Fogarty, P. Goranson, P. Heitzenroeder, S. Hirshman, G. Jones, J. Lyon, G. Neilson, W. Reiersen, D. Strickler, and D. Williamson, "Design of the national compact stellarator experiment (ncsx)," *Fusion Engineering and Design*, vol. 66, pp. 169 – 174, 2003. 22nd Symposium on Fusion Technology.

[5] V. Bykov, F. Schauer, K. Egorov, A. Tereshchenko, P. van Eeten, A. DÃ¼bner, M. Sochor, D. Zacharias, A. Dudek, W. Chen, P. Czarkowski, L. Sonnerup, J. Fellinger, D. Hathiramani, M. Ye, and W. DÃ¤nner, "Structural analysis of w7-x: Overview," *Fusion Engineering and Design*, vol. 84, no. 2, pp. 215 – 219, 2009. Proceeding of the 25th Symposium on Fusion Technology.

[6] S. F. K. J. D. H. R. K. C. M. Joshua T. Peterson, Greg J. Hartwell, "Initial vacuum magnetic field mapping in the compact toroidal hybrid," *Journal of Fusion Energy*, 2007.

[7] J. T. Peterson, *VACUUM MAGNETIC FLUX SURFACE MEASUREMENTS MADE ON THE COMPACT TOROIDAL HYBRID*. PhD thesis, Auburn University, 2008.

[8] J. Hanson and J. Cary, "Elimination of stochasticity in stellarators," *Plasma Physics and Fusion Techology*, vol. 15, no. 05, 1983.

[9] S. Hirshman and W. van RIJ, "Three-dimensinal free boundary calculations using a spectral green's function method," *Computer Physics Communications*, vol. 43, no. 1, pp. 143–155, 1986.

[10] X. Ma, M. R. Cianciosa, D. A. Ennis, J. D. Hanson, G. J. Hartwell, J. L. Herfindal, E. C. Howell, S. F. Knowlton, D. A. Maurer, P. J. Traverso, and et al., "Determination of current and rotational transform profiles in a current-carrying stellarator using soft x-ray emissivity measurements," *Physics of Plasmas*, vol. 25, no. 1, p. 012516, 2018.

[11] I. H. Hutchinson, *Principles of plasma diagnostics*. Cambridge, 2002.

[12] T. Equipe, "Tokamak plasma diagnostics," *Nuclear Fusion*, vol. 18, no. 5, p. 647, 1978.

[13] E. J. Strait, "Magnetic diagnostic system of the diii-d tokamak," *Review of Scientific Instruments*, vol. 77, no. 2, 2006.

[14] M. D. Pandya, M. C. ArchMiller, M. R. Cianciosa, D. A. Ennis, J. D. Hanson, G. J. Hartwell, J. D. Hebert, J. L. Herfindal, S. F. Knowlton, X. Ma, S. Massidda, D. A. Maurer, N. A. Roberds, and P. J. Traverso, "Low edge safety factor operation and passive

disruption avoidance in current carrying plasmas by the addition of stellarator rotational transform," *Physics of Plasmas*, vol. 22, no. 11, p. 110702, 2015.

[15] M. C. ArchMiller, M. R. Cianciosa, D. A. Ennis, J. D. Hanson, G. J. Hartwell, J. D. Hebert, J. L. Herfindal, S. F. Knowlton, X. Ma, D. A. Maurer, M. D. Pandya, and P. Traverso, "Suppression of vertical instability in elongated current-carrying plasmas by applying stellarator rotational transform," *Physics of Plasmas*, vol. 21, no. 5, p. 056113, 2014.

[16] M. C. Miller, J. D. Hanson, G. J. Hartwell, S. F. Knowlton, D. A. Maurer, and B. A. Stevenson, "Design and implementation of a multichannel millimeter wave interferometer for the compact toroidal hybrid experiment," *Review of Scientific Instruments*, vol. 83, no. 10, pp. –, 2012.

[17] X. Ma, D. A. Maurer, S. F. Knowlton, M. C. ArchMiller, M. R. Cianciosa, D. A. Ennis, J. D. Hanson, G. J. Hartwell, J. D. Hebert, J. L. Herfindal, M. D. Pandya, N. A. Roberds, and P. J. Traverso, "Non-axisymmetric equilibrium reconstruction of a current-carrying stellarator using external magnetic and soft x-ray inversion radius measurements," *Physics of Plasmas*, vol. 22, no. 12, 2015.

[18] M. D. Pandya, *Low edge safety factor disruptions in the Compact Toroidal Hybrid: Operation in the low-q regime, passive disruption avoidance and the nature of MHD precursors*. PhD thesis, Auburn University, 2016.

[19] J. Herfindal, J. Dawson, D. Ennis, G. Hartwell, S.D.Loch, and D. Maurer, "Design and initial operation of a two-color soft x-ray camera system on the compact toroidal hybrid experiment," *Review of Science Instrument*, vol. 85, no. 11, 2014.

[20] N. A. Roberds, L. Guazzotto, J. D. Hanson, J. L. Herfindal, E. C. Howell, D. A. Maurer, and C. R. Sovinec, "Simulations of sawtoothing in a current carrying stellarator," *Physics of Plasmas*, vol. 23, no. 9, 2016.

[21] J. L. Herfindal, D. A. Maurer, G. J. Hartwell, D. A. Ennis, J. D. Hanson, S. F. Knowlton, X. Ma, M. D. Pandya, N. A. Roberds, P. J. Traverso, and et al., "Sawtooth oscillation behavior with varying amounts of applied stellarator rotational transform," *Physics of Plasmas*, vol. 26, no. 3, 2019.

[22] J. Schilling, H. Thomsen, C. Brandt, S. Kwak, and J. Svensson, "Soft x-ray tomograms are consistent with the magneto-hydrodynamic equilibrium in the wendelstein 7-x stellarator," *Plasma Physics and Controlled Fusion*, vol. 63, p. 055010, mar 2021.

[23] J. D. Hanson, S. F. Knowlton, B. A. Stevenson, and G. J. Hartwell, "Equilibrium and stability of current-carrying discharges in the non-axisymmetric cth experiment," *Contributions to Plasma Physics*, vol. 50, no. 8, pp. 724–730, 2010.

[24] J. Hanson, D. Anderson, M. Cianciosa, P. Franz, J. Harris, G. Hartwell, S. Hirshman, S. Knowlton, L. Lao, E. Lazarus, L. Marrelli, D. Maurer, J. Schmitt, A. Sontag, B. Stevenson, and D. Terranova, "Non-axisymmetric equilibrium reconstruction for stellarators, reversed field pinches and tokamaks," *Nuclear Fusion*, vol. 53, no. 8, p. 083016, 2013.

Chapter 4

Machine Learning-Based Bolometer Inversion

4.1 Introduction

Achieving high spatial resolution tomography is the goal for the new bolometer arrays, former soft x-ray (SXR) cameras, on the Compact Toroidal Hybrid (CTH) experiment. Tomography is a longstanding technique in many areas, such as medicine, where the spatial information taken from the orientation and position of a series of cameras or using the same camera with multiple configurations is used to reconstruct an image with either a higher resolution or higher dimensionality than the original images. For example, computed tomography (CT scans) in medicine is the practice of taking thousands of x-ray images as the x-ray source and detector are rotated around the patient. Knowing the spatial information from each 2D image, a single 3D image is produced by tomography. Tomography for CTH purposes is the practice of relating the incident powers measured by the new bolometer detectors with their corresponding solid angles and spatial orientations to map out the source of the emission i.e. the emitted power density of the plasma.

Considering a simple bolometer arrangement having one detector viewing the plasma through a slit, as illustrated in Fig. 4.1, the incident power on the *i*th channel of the bolometer, p_i in units of W is given as

$$p_i = \int_V \frac{\Omega_i(\mathbf{r})}{4\pi} G(\mathbf{r}) dV \tag{4.1}$$

where the integration is done over the viewing volume of the detector, $\Omega_i(\mathbf{r})$ is the solid angle of the cone from the surface of the detector, and $G(\mathbf{r})$ is the emitted power density of the plasma in W/m^3.

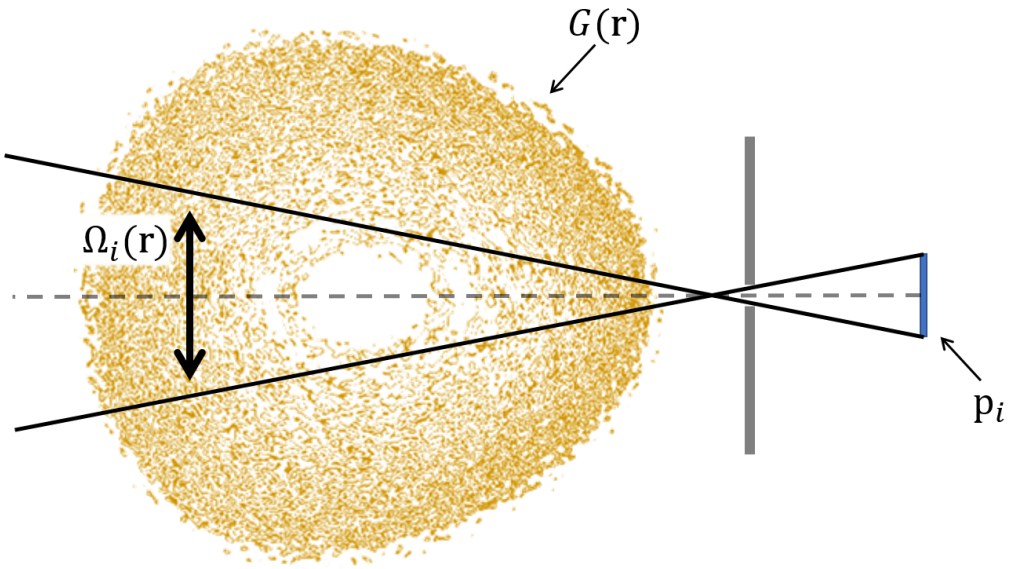

Figure 4.1: A bolometer showing the *i*th channel having an incident power p_i with a solid angle $\Omega_i(\mathbf{r})$ viewing the emitted power density of the plasma $G(\mathbf{r})$.

When working with a more complex bolometer arrangement, as illustrated in the two detector setup in Fig. 4.2, the bolometer brightness becomes important when comparing the data gathered from detectors having different positions and orientations. The bolometer brightness b_i (in units of W/m^2) can be found when both sides of Eq. 4.1 are normalized by 4π over the etendue or throughput of the detector. The etendue is defined as the product of the solid angle Ω_i and the area A_i perpendicular to axis of the cone Ω_i. For example, in Fig. 4.2, the etendue for the first detector is $\langle A_1\Omega_1\rangle = A_1 cos(\alpha_1)\Omega_1$. The bolometer brightness for the *i*th channel is then

$$b_i = p_i \frac{4\pi}{\langle A_i\Omega_i\rangle} = \int\int \frac{\Omega_i(R,Z)}{\langle A_i\Omega_i\rangle} G(R,Z)dRdZ \tag{4.2}$$

where R and Z are the horizontal and vertical coordinates for the poloidal cross section (located at toroidal angle ϕ) on CTH as viewed by the bolometer arrays. Since the toroidal viewing angles are small, the local variation of the emissivity in the toroidal direction is ignored.

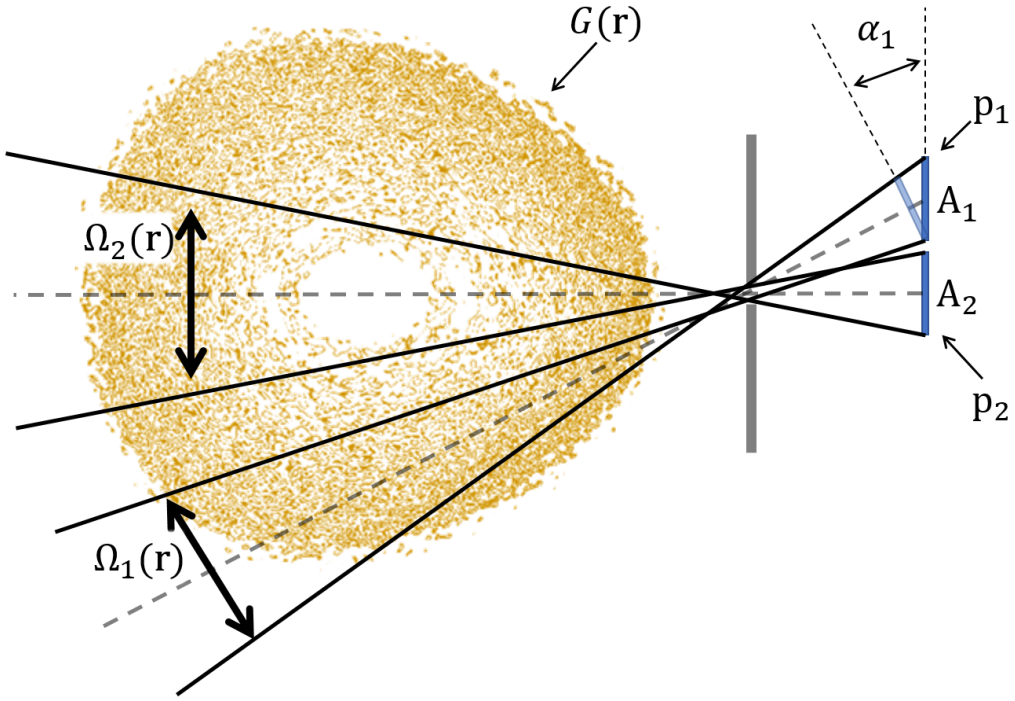

Figure 4.2: A two detector bolometer showing the incident powers (p_1, p_2) and solid angles (Ω_1, Ω_2) for each detector viewing the emitted power density of the plasma $G(\mathbf{r})$.

At this point, a projection operator can be used to introduce a 2D mapping of G, such as is shown in Fig. 4.3, to a discrete measurement b_i. This projection operator T_i is defined as

$$T_i(R, Z) = \int \frac{\Omega_i(R, Z)}{\langle A_i \Omega_i \rangle} dR dZ \tag{4.3}$$

and describes the geometric properties of the diagnostics.

Eq. 4.2 can now be discretized on a rectangular grid having pixels n. The resulting brightness of m number of bolometer detectors is

$$b_i = \sum_{j=1}^{n} T_{ij} g_j \qquad i \in 1, .., m \tag{4.4}$$

where $\mathbf{T} \in \mathbb{R}^{m,n}$ denotes a geometry matrix, defining the contribution of a pixel j to the measurement i and g_j is the local emissivity at the jth pixel in units W/m^3. For example, in Fig. 4.3, the brightness of the second detector is $b_2 = \sum_{j=1}^{25} T_{2j} g_j$. Retaining only the non-zero components, the brightness becomes $b_2 = T_{2,11} g_{11} + T_{2,12} g_{12} + T_{2,13} g_{13} + T_{2,14} g_{14} + T_{2,15} g_{15}$.

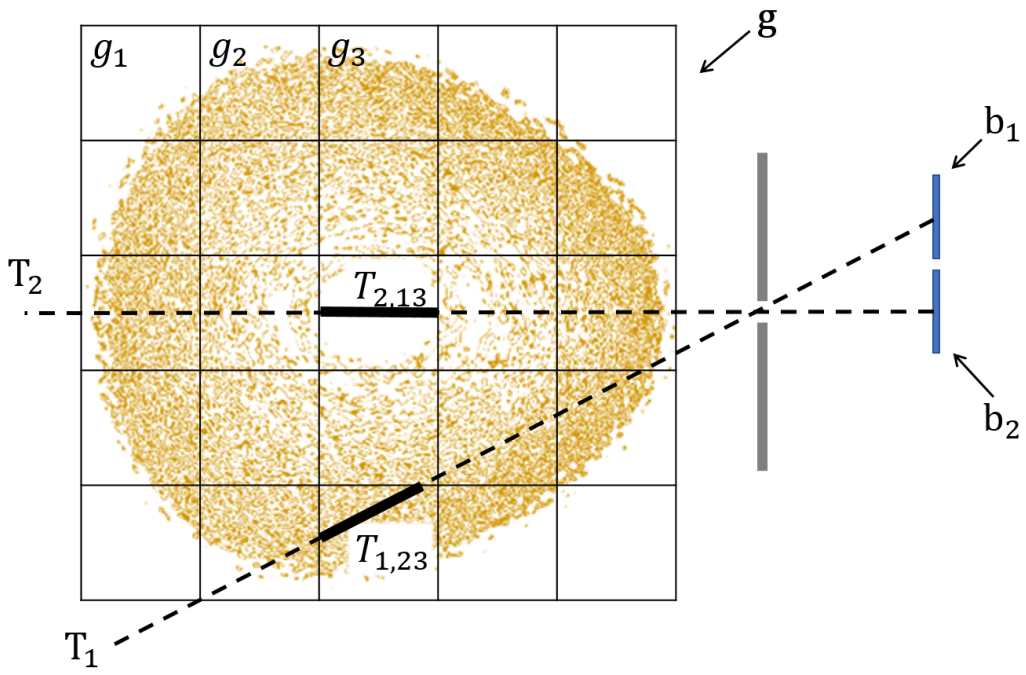

Figure 4.3: A two detector bolometer showing the brightness (b_1, b_2) and projection operators (T_1, T_2) for each detector viewing the emitted power density of the plasma $G(\mathbf{r})$ discretized on a 5 x 5 grid **g**.

Eq. 4.4 can be written in matrix form as

$$\mathbf{b} = \mathbf{Tg} \tag{4.5}$$

where **b** is the bolometer detector brightness vector and **g** is the pixel grid. With a pixel grid covering a poloidal slice of the plasma, the total radiated power can be approximated as

$$\mathbf{P}_{radiated} = \left(\sum_{j=1}^{n} g_j \right) \cdot 2\pi R_0 \tag{4.6}$$

where R_0 is the major radius of the plasma. In this approximation, the plasma emissivity is treated as toroidally symmetric. While this assumption is easily challenged, it provides the best available estimate of the total radiated power. Ideally, multiple pixel grids (**g**) covering different poloidal slices could be found providing an even better estimate of the total radiated power.

4.2 Review of Tomographic Inversion Techniques

The ultimate goal of inverting the bolometer measurements to obtain the local plasma emissivity can be expressed simply by rewriting Eq. 4.5 to be

$$\mathbf{g} = \mathbf{T}^{-1}\mathbf{b}. \tag{4.7}$$

In practice, this is a ill-posed problem (1). For any meaningful results having high spatial resolution $\mathbf{g} >> \mathbf{b}$, the result is a significantly underdetermined system. Therefore, most inversion or reconstruction algorithms seek to find a solution by varying $\mathbf{g}$ to minimize χ^2 which is defined as

$$\chi^2 = \left(\mathbf{T} * \mathbf{g} - \hat{\mathbf{b}}\right)^T * \left(\mathbf{T} * \mathbf{g} - \hat{\mathbf{b}}\right) \tag{4.8}$$

where $\hat{\mathbf{b}} = \mathbf{b}/\boldsymbol{\sigma}$ with $\boldsymbol{\sigma}$ being the uncertainty vector for the signal vector $\mathbf{b}$.

The question remains of how to find an initial $\mathbf{g}$ and how to vary it. Over the years, different reconstruction methods have been developed such as local and global basis functions (2), assumptions of smoothness on magnetic flux surfaces (commonly used for SXR inversion) (3), Tikhonov regularization (4), Minimum Fisher Regularization (5), and Bayesian Maximum Likelihood (6). Recently, work has been done on applying machine learning techniques such as neural networks and deep learning to bolometer tomography (7; 8).

4.2.1 Magnetic Flux Surface Inversion

With the inclusion of SXR diagnostics into V3FIT (9; 10; 11; 12), SXR measurements are routinely inverted to gain a 1D radial profile under the assumption that SXR emissivity is a magnetic flux surface quantity. This implementation has provided insight into constraining the rotational transform on the magnetic axis. While the validity of SXR emission being a flux surface quantity can be challenged, recent studies have shown good agreement between SXR emissivity and magnetic flux surfaces (13). However, bolometer emission on CTH under the same assumption can be much more problematic because of the presence of large asymmetries in the data that cannot be characterized by a magnetic flux surface quantity (see Fig. 3.12). Yet,

for sake of simplicity, bolometer inversions via fitting emissivity values constant on a magnetic flux surface are routinely used as a check for other methods on CTH.

Practically, the process is simple. First, a 3D reconstruction is performed using V3FIT typically with all available magnetic diagnostics, SXR diagnostics, and interferometer. Second, an initial 1D emission profile is selected in flux surface coordinates. This profile in principle can take any form, but generally, we use a 10 point spline where emission values at each point can be varied by our minimization routine. Third, the χ^2 is calculated based on Eq. 4.8. The values or parameters in the selected profile are then systematically varied to minimize χ^2. While this method is crude and can be improved with better profiles or imposed constraints (such as smoothness), it serves as a quickly computed baseline inversion with moderately good fits. Note, the total computation time for this inversion needs to take into account that a V3FIT reconstruction must be completed first which, depending upon the nature of the reconstruction and the utilized computer hardware, typically consumes the greatest portion of the computational time.

An application of the magnetic flux surface inversion method is shown in the remainder of this section. Fig. 4.4(a) provides the viewing chords of the SXR and bolometer configuration. Note, both the SXR cameras and bolometers share the same poloidal viewing chords with overlapping views in the toroidal direction. Several of the magnetic flux surfaces, from a V3FIT reconstruction at $t = 1.6374s$, including the last closed flux surface (LCF) are shown in red.

Fig. 4.4(b) gives some example SXR (top) and bolometer (bottom) data from Shot 20100633 for the midplane cameras. This high density shot produced strong SXR and bolometer signals. The SXR signals are largely symmetric with some core fluctuations that may be associated with a $m/n = 1/1$ sawtoothing MHD mode (14). The bolometric signals are very asymmetric and violate our assumptions for this inversion method. The large asymmetry in the bolometric data is only seen in high density discharges where either the hydrogen or the deuterium gas is aggressively puffed. At low densities, the bolometer signals are mostly symmetric. The probable source of this asymmetry is the physical location of our gas puffers. Both gas puffers used for this shot are located toroidally on either side of the bolometers with both positioned on the top of CTH.

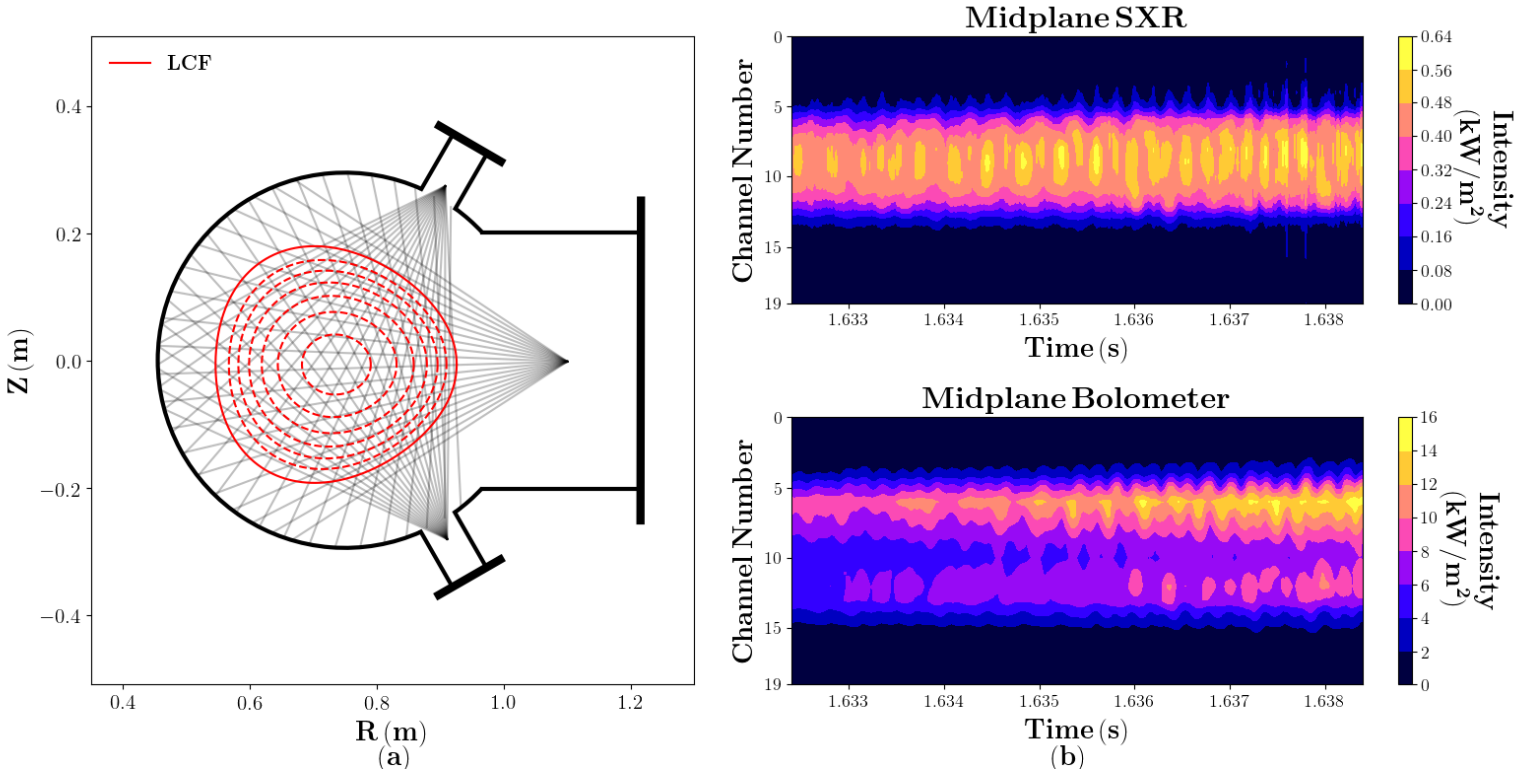

Figure 4.4: The positioning and orientation of the SXR cameras and bolometers is shown in (a). Example data from shot 20100633 for the midplane cameras is shown (b) for both the SXR and the bolometers.

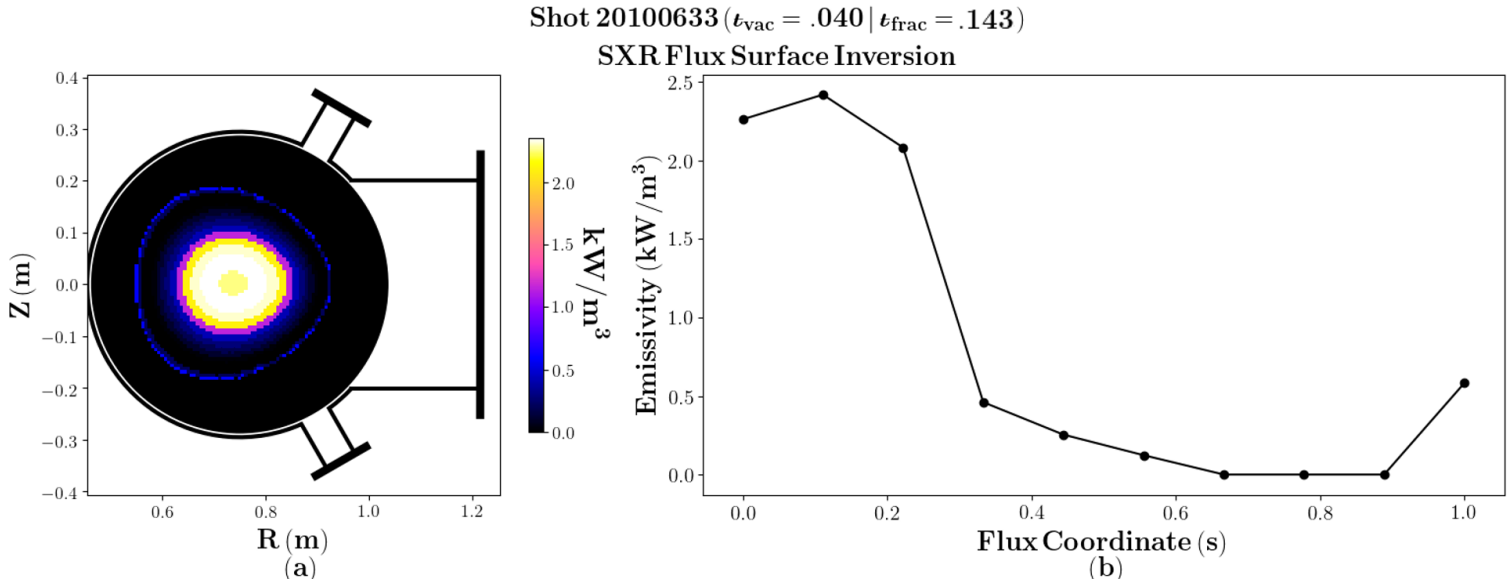

Figure 4.5: The inverted SXR signal at time $t = 1.6374$ from Fig. 4.4(b) is shown on the left (a) with the SXR profile in magnetic flux surface coordinates shown on the right (b).

Starting with the SXR inversion, Fig. 4.5 shows the inverted signals mapped to a pixel grid (a) as well as the fitted profile in flux surface coordinates (b). This inversion was performed using the V3FIT reconstructed flux surfaces shown in 4.4(a). The SXR data was averaged over a $100\mu s$ window at time $t = 1.6374s$. Fig. 4.6 shows the results from a similar inversion using the bolometer data averaged over the same time window.

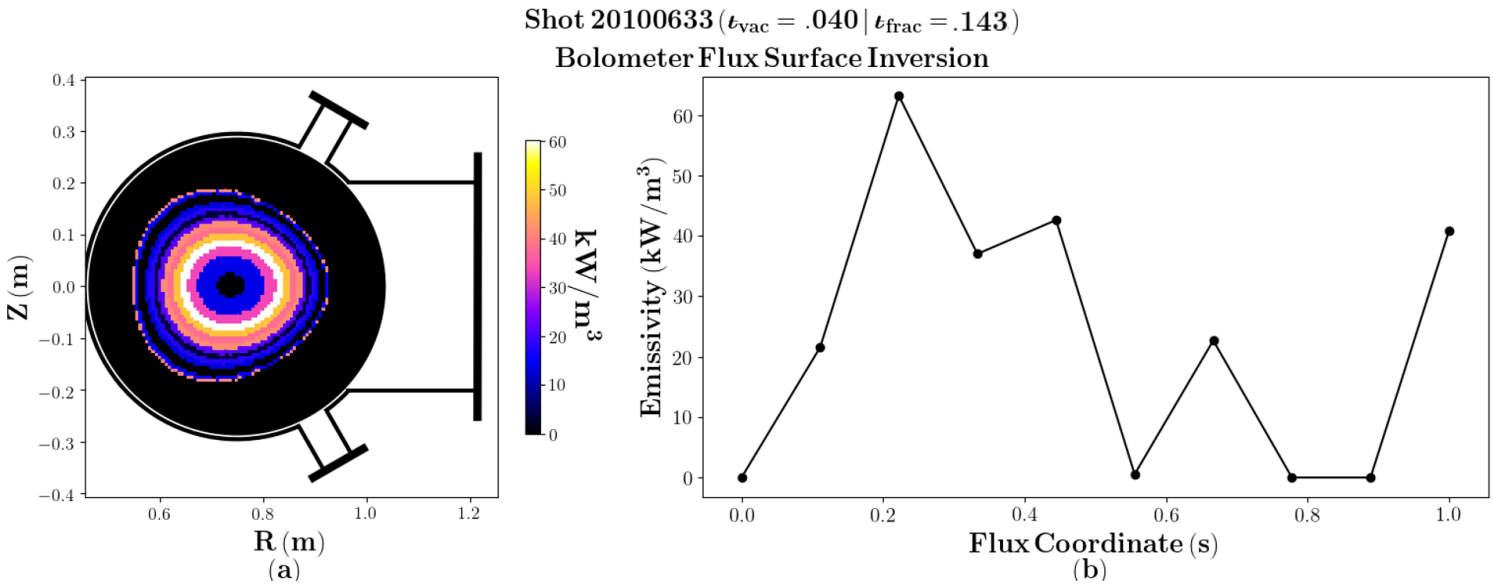

Figure 4.6: The inverted bolometer signal at time $t = 1.6374$ from Fig. 4.4(b) is shown on the left (a) with the bolometer profile in magnetic flux surface coordinates shown on the right (b).

For both inversions, the measured signals and the signals taken from the inversion are shown in Fig. 4.7. Overall, the SXR signals are reproduced more closely by this inversion method. The SXR inversion results as well as the well-behaved nature (aside from the artifact at the outermost radial position) of the emissivity profile (Fig. 4.5(b)) indicate a reasonable application of this method. In contrast, the bolometer is not well inverted. Poor behavior in the emissivity profile, which has large spatial variations and zero emission at the center of the plasma as seen in Fig. 4.6(b), coupled with the badly mismatched signals in Fig. 4.7(b) exemplify why this method is not suitable for bolometer inversions.

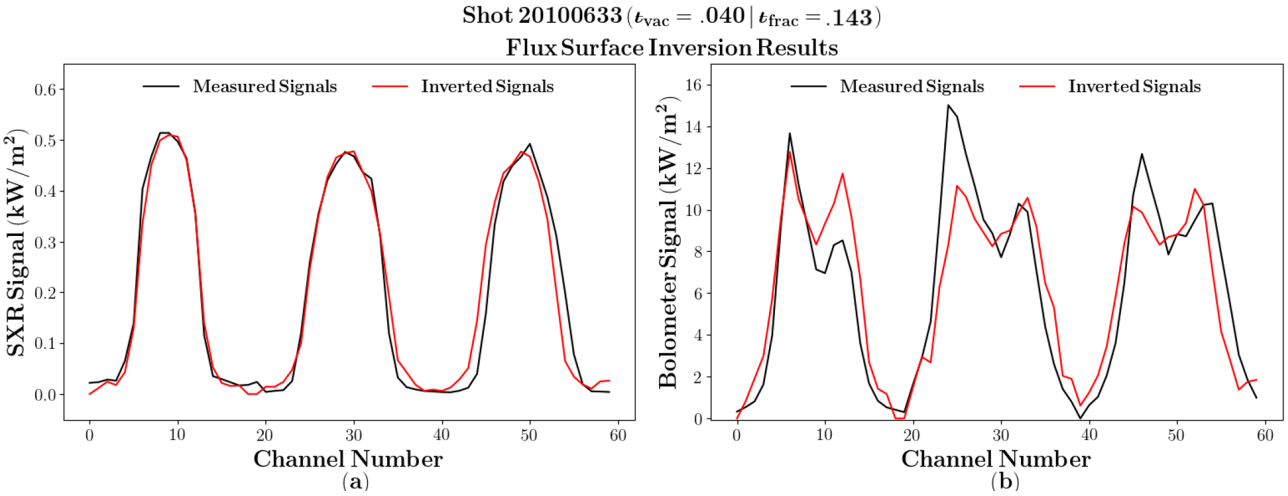

Figure 4.7: The measured and inverted signals taken from inversions plotted in Figs. 4.5 and 4.6 for the SXR (a) and bolometer (b) are show.

4.2.2 Tikhonov Regularization

A more advanced and commonly used method to solve the ill-posed problem in Eq. 4.5 is the Tikhonov-Phillips regularization (4). This section provides the mathematically framework for the implementation of this method for any tomography problem. Tikhonov regularization searches for the minimum of the objective functional $\Lambda(\mathbf{g})$ defined by

$$\Lambda(\mathbf{g}) = (\mathbf{Tg} - \hat{\mathbf{b}})^T \mathbf{\Sigma}^{-1} (\mathbf{Tg} - \hat{\mathbf{b}}) + \lambda O(\mathbf{g}) \tag{4.9}$$

where $\mathbf{\Sigma}$ is the expected covariance matrix, $O(\mathbf{g})$ is a regularization functional, and λ is a positive regularization parameter that balances the strength of *a priori* contraints with respect to the goodness of the fit. For simplicity, the $\mathbf{T}$ and $\mathbf{b}$ matrices can already be weighted by a square root of the covariance matrix

$$\mathbf{\Sigma}^{-\frac{1}{2}}\mathbf{T} \rightarrow \mathbf{T}, \qquad \mathbf{\Sigma}^{-\frac{1}{2}}\mathbf{b} \rightarrow \mathbf{b} \tag{4.10}$$

The purpose of $O(\mathbf{g})$ is to impose *a priori* knowledge about the emissivity profiles. This is often some kind of a roughness penalty and a boundary constraint. The regularization operator

is typically of quadratic form

$$O(\mathbf{g}) = \mathbf{g}^T \mathbf{H}(\mathbf{g}) \mathbf{g}, \tag{4.11}$$

with a symmetric and positive semi-definite operator $\mathbf{H} \in \mathbb{R}^{n,n}$, which can be a function of $\mathbf{g}$. A common boundary constraint is zero emissivity at the borders, enforced by adding sufficiently large positive values to the diagonal points of $\mathbf{H}$ corresponding to the pixels outside of the boundary. Therefore, the regularization operator includes all soft constraints for the solutions. Hard constraints can be imposed by introducing an orthonormal matrix $\mathbf{P} \in \mathbb{R}^{m,l}$ and performing the transformations $\hat{\mathbf{T}} = \mathbf{TP}$, $\hat{\mathbf{H}} = \mathbf{P}^T\mathbf{HP}$, and $\hat{\mathbf{g}} = \mathbf{P}^T\mathbf{g}$. The solution will be restricted to a linear subspace generalized by the columns of $\mathbf{P}$. An example of $\mathbf{P}$ is the orthonormalized Fourier-Bessel basis functions in the magnetic field line coordinate system.

A minimum of Eq. 4.9 can now be written as a quadratic optimization problem for a constant matrix $\mathbf{H}$ in the form

$$\Lambda(\mathbf{g}) = ||\mathbf{Tg} - \hat{\mathbf{b}}||^2 + \lambda \mathbf{g}^T \mathbf{Hg} \tag{4.12}$$

where the minimum is

$$\begin{aligned} \mathbf{g} &= (\mathbf{T}^{-1}\mathbf{T} + \lambda\mathbf{H})^{-1}\mathbf{T}^T\hat{\mathbf{b}} \\ \mathbf{g} &= \mathbf{M}\hat{\mathbf{b}} \end{aligned} \tag{4.13}$$

where $\mathbf{M} = (\mathbf{T}^{-1}\mathbf{T} + \lambda\mathbf{H})^{-1}\mathbf{T}^T$. A direct inversion of this equation is possible. However, due to the large dimension of the matrices ($n \times n$), the high computational complexity $\mathcal{O}(n^3)$ of the inversion, and the number of inversions required to find a proper λ, this procedure is highly impractical.

Nevertheless, the process is an iterative one. First, for a given $\mathbf{H}$ and $\hat{\mathbf{b}}$, an initial $\boldsymbol{\lambda}_0$ and $\mathbf{g}_0$ are guessed, and then $\mathbf{M}_0$ is calculated. Second, $\mathbf{g}_1$ is determined from the application of $\mathbf{M}_0$ to Eq. 4.13. Third, $\boldsymbol{\chi}^2$ is calculated from Eq. 4.8. If $\boldsymbol{\chi}^2$ is sufficiently close to unity, the inversion is deemed complete and $\mathbf{g}$ has been found. If not, and if the number of preceding iterations has not reached a predetermined maximum number of iterations, then $\boldsymbol{\lambda}_1$ can be estimated from $\mathbf{g}_1$

and $\mathbf{g}_0$ using Newton's method or gradient descent. Having then $\boldsymbol{\lambda}_1$ and $\mathbf{g}_1$, the next iteration can begin. This process continues until $\boldsymbol{\chi}^2$ is sufficiently close to unity or the maximum number of iterations is reached.

The optimization problem Eq. 4.12 has a unique solution if the null spaces of **T** and **H** have only a trivial intersection. In order to employ computationally efficient numerical algorithms, an invertible **H** matrix is required. Invertibility can be imposed by a proper definition of the boundary constraints or by adding an identity matrix $\epsilon\mathbf{I}$ to **H**, where ϵ has the size of the order of the smallest non-zero eigenvalues of **H**.

4.2.3 Minimum Fisher Information

The most common regularization operators (the functional to be minimized) are the identity operator, which suppresses the Euclidean norm of the solution, and the Laplace operator, which reduces the curvature of the emissivity profile. Nevertheless, the special features of the SXR profiles, like the peaked distribution of the SXR radiation, the sharp gradients, and the large dynamic range, make the nonlinear Minimum Fisher Information (MFI) regularization (5) an ideal candidate for the regularization functional used for both SXR and bolometers. This functional can be expressed in the following form:

$$O_{MFI}(G) = \int\int dS \frac{1}{G} (\nabla_{\mathbf{u}} G)^T \mathbf{J}_2 (\nabla_{\mathbf{v}} G) \tag{4.14}$$

where $\mathbf{u}(x, y)$ and $\mathbf{v}(x, y)$ are two locally orthogonal vector fields, $\mathbf{J}_2 \in \mathbb{R}^{2,2}$ represents a matrix of ones, and G is **g** transformed into the appropriate coordinate system for differentiation. If **u** is parallel with the Cartesian coordinates, the method is called *isotropic* MFI and if **u** is locally tangential to the magnetic flux surfaces, the *anisotropic* MFI regularization is obtained. More details about the implementation of the anisotropic MFI can be found in the literature (15). The regularization operator **H** here, representing a linearized and discretized functional (Eq. 4.14), is given by

$$\mathbf{H}^{(k)} = \sum_{\ell \in \{\mathbf{u},\mathbf{b}\}} \mathbf{B}_\ell^T \mathbf{W}^{(k)} \mathbf{B}_\ell \tag{4.15}$$

where $\mathbf{B}_\ell$ denotes a discretized gradient operator ∇_ℓ and $\mathbf{W}_{ij}^{(k)}$ is a weight matrix defined as the inverse of $\mathbf{g}^{(k)}$ and denoted by

$$W_{ij}^{(k+1)} = \delta_{ij}/max\{g_j^{(k)}, \epsilon\}. \tag{4.16}$$

The MFI regularization must be solved iteratively because the weight matrix $\mathbf{W}$ depends on the emissivity $\mathbf{g}$. The small positive constant ϵ prevents division by zero and, moreover, it serves as a weak positivity constraint for the Tikhonov regularization because the regions with the negative values are strongly smoothed and pushed closer to or above zero. Commonly, $\epsilon = 10^{-8}$ of the emissivity maximum is used, which is usually an adequate compromise between positivity and a numerical instability caused by a too low value of ϵ.

While other functionals have been developed for Tikhonov regularization, the MFI method has become the preferred choice when seeking to imposes spatial preferences (such as smoothness) on the resultant $\mathbf{g}$ (1). In an anisotropic implementation of MFI to enforce smoothness along magnetic flux surfaces, MFI is more recommended than the 1D Abel Inversion (1; 16) or magnetic flux surface inversions.

4.2.4 Review of Tomographic Methods

While novel tomographic methods other than what have already been discussed exist (such as a Bayesian approach (6; 17)), those mentioned here provide a framework for a discussion of practicality. The magnetic flux surface inversion provides a good solution to emission that is purely a flux surface quantity but suffers due to the necessary computational time needed for a V3FIT reconstruction. The Tikhonov regularization is a mathematically straight forward approach, but computational complex ($\mathcal{O}(n^3)$), and extremely dependent on the objective functional chosen for minimization. The Minimum Fisher Information provides a robust functional that is particularly good for SXR radiation by allowing peaks and sharp gradients while enforcing smoothness. Coupled with reconstructed flux surfaces, this method in anistropic form provides a solution that is better than an Abel inversion but still requires significant computational time.

For CTH bolometer inversions, to date, only the magnetic flux surface inversion technique from the list above has been performed, mainly because the SXR side had already been implemented. With the capabilities and limitations from the other options in mind, it was decided to pursue a different approach. Instead of choosing a straight forward mathematical formulation like the Tikhonov regularization, a less mathematically understandable yet potentially more practical solution was chosen in the form of machine learning.

4.3 Introduction to Convolutional Neural Networks

In recent years, deep machine learning (18) has become the go-to solution for many problems that have historically been difficult for computers to solve. From image processing to natural language understanding, deep learning has shown itself capable in solving computationally complex problems. Convolutional Neural Networks (CNN) in particularly have successfully been deployed for image classification (19; 20), image segmentation (21; 22), and object detection (23; 24). While CNN have a long history (25), advancements in training algorithms (26; 27) and parameter initialization techniques (28) coupled with improvements on computer hardware, especially with the use of graphics processing units (GPUs) (29; 30), and software, with development of libraries such as Theano (31), Tensorflow (32), Caffe (33), and Keras (34), have allowed an explosion of ground breaking results and applications. With the available increased complexity of models, developments such as dropout (35) and batch normalization (36) were needed to improve overfitting.

At the most basic level, neural networks are made of artificial "neuron". Fig. 4.8 shows an artificial neuron. The weights w_i and bias b are known as free or learnable parameters (25) and are varied by the training algorithm. The activation function $\Phi(a)$ is needed because otherwise, when stacking consecutive neurons, one would solely apply consecutive linear transformations which is equivalent to a single linear transformation. The success of neural networks lies with the activation function, which allows the training algorithm to "turn off" or "turn on" the neuron restricting or allowing the consecutive flow of information. This ability, to dynamically map out a new path or regression, gives the neural network its almost "magical" problem solving capabilities.

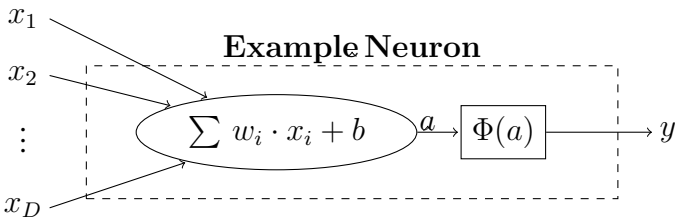

Figure 4.8: Example of an artificial neuron having inputs (x_1, x_2, $\cdots$, x_D) and their associative parameters or weights w_i in addition to the bias b. The summation is followed by the non-linear activation function $\Phi(a)$ with the neuron output being y.

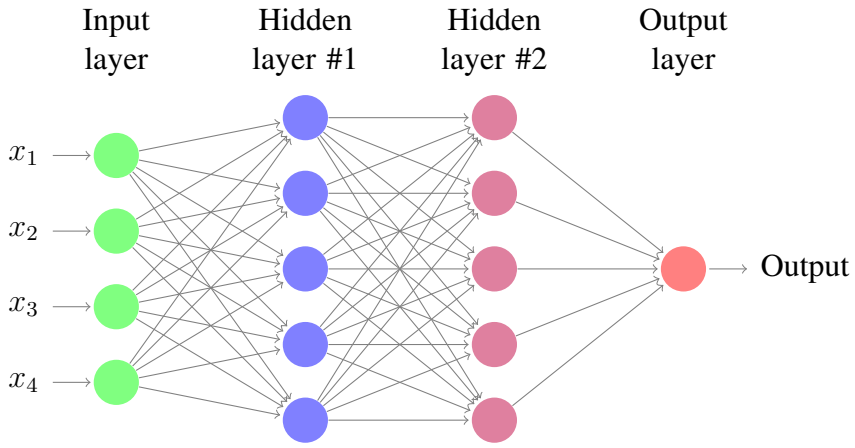

Figure 4.9: Example of a deep neural network having 4 inputs, 2 hidden layers each with 5 neurons, and one output.

Having defined a neuron, a definition of a neural network can be given. Fig. 4.9 shows an example neural network having four inputs (x_1, x_2, x_3, x_4) with two hidden layers each with five neurons, and one output. A hidden layer is simply a grouping of neurons that is not visible or controllable to the outside user. The layers shown in Fig. 4.9 are called fully connected or dense layers because every neuron receives as inputs all of the outputs from the previous layers. This simple example has 50 trainable weights w_i and 11 trainable biases b totalling 61 trainable parameters.

Convolutional Neural Networks (CNN) add one or more additional layers called convolutional layers. Each node in a convolutional layer is a convolution that produces a feature map. Fig. 4.10 gives an example convolution. As the filter is stepped across the input image or matrix, the filter multiplies its weights and sums to create one pixel or matrix element. Unless the input image is padded with zeros that surround the original, the output image size will be

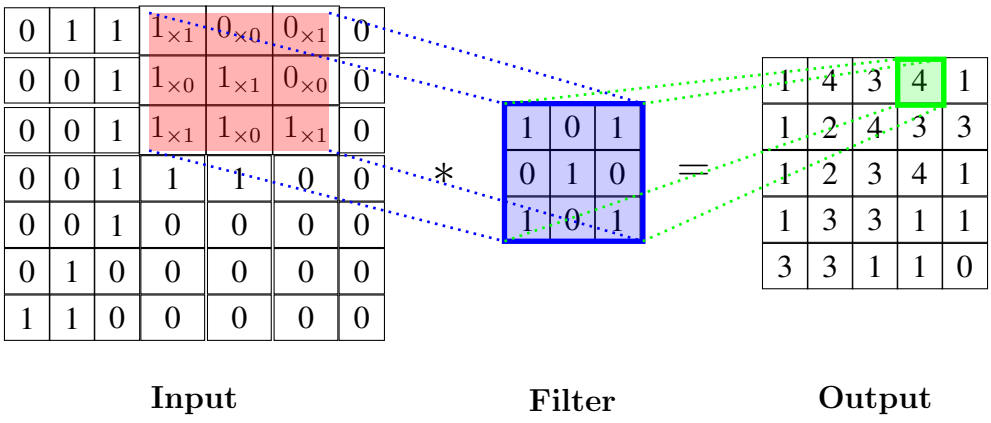

Figure 4.10: Example of a convolution.

reduced. Convolutions have been used for image processing such as edge detection and feature sharpening.

A convolutional layer takes a traditional convolution filter and allows the weights to be varied. In addition, an activation function is added to allow the capability of a convolution to be switched on or off. For a convolutional layer, the output is known as a feature map of the input. Depending on the structure of the CNN, one or more feature maps can be used as the input for the next layer. Fig. 4.11 shows a CNN with two convolutional layers. The first layer has four filters producing four feature maps. All of the feature maps are used as the input for the second layer which has five filters and produces five feature maps. In practice, after several convolutional layers, the output is fed into a series of fully connected layers before producing a result. An example CNN is one, that once trained on labeled images of dogs and cats, takes any image input, runs it through the network and outputs a probability that a dog or a cat was in the image. Images go in; probabilities come out.

CNNs have been used successfully for object detection in images, facial recognition, handwriting interpretation, and many other applications. The power of this method lies in the CNNs ability to switch on and off both the neurons in the fully connected layers and the filters in the convolutional layers.

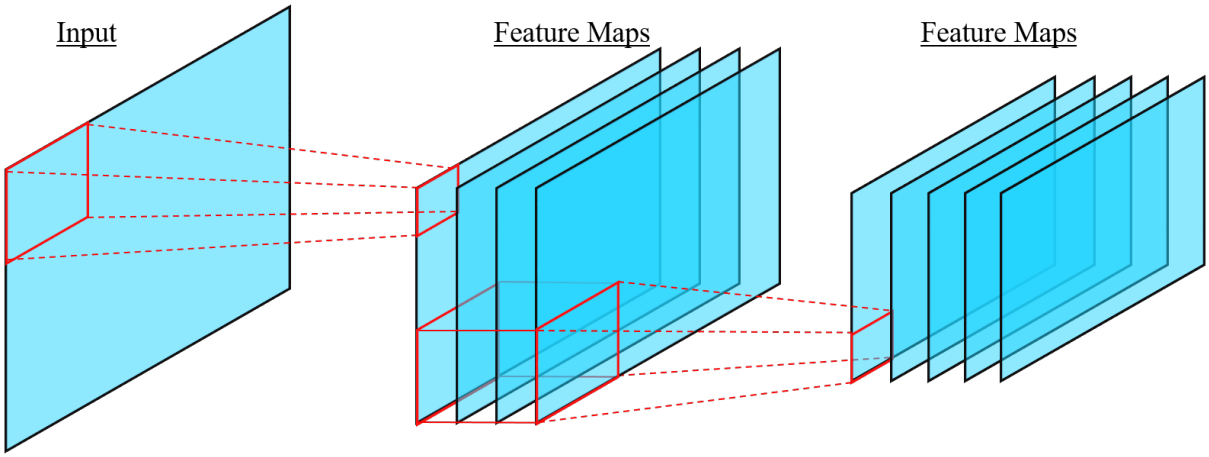

Figure 4.11: An example Convolutional Neural Network (CNN) having to two convolutional layers. The first has four filters producing four feature maps. The second convolutional layer uses all of the feature maps from the previous layer. The second layer has five filter producing five feature maps

4.4 De-Convolutional Neural Networks (DeCNN)

Inspired by the success of CNNs on image-based challenges, researchers at JET (7; 8) inverted a CNN. Instead of inputting an image and getting a set of probabilities out, a set of values is given (bolometer signals) and an image is produced. This novel approach is shown in Fig. 4.12. The input consists of 56 bolometer signals with an output pixel grid of 120 by 200 pixels and has approximately 56 million trainable parameters. The lines of sight for the JET bolometers used for the DeCNN are shown in Fig. 4.13.

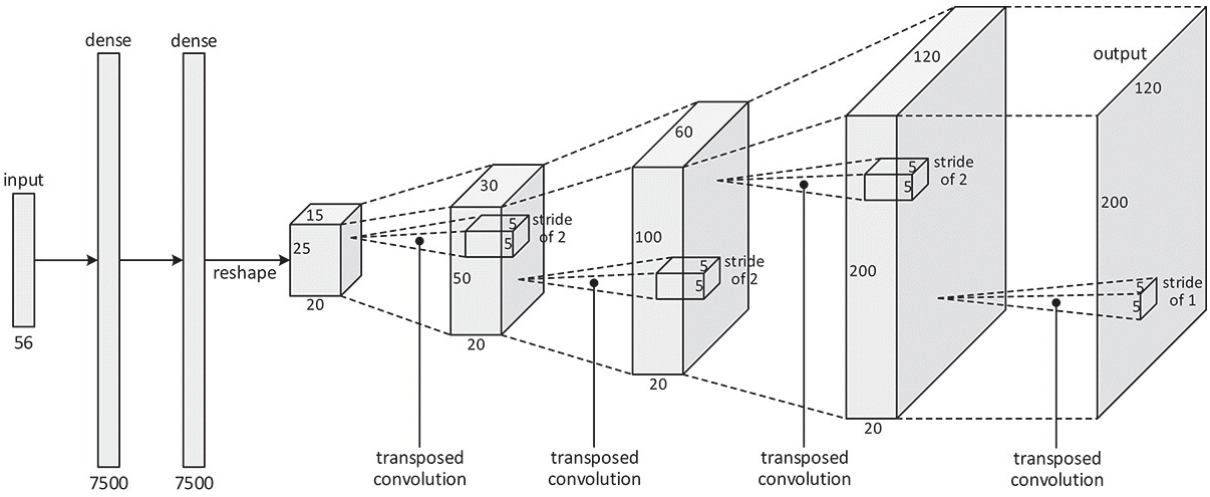

Figure 4.12: DeCNN developed by researchers at JET for bolometer tomography(7).

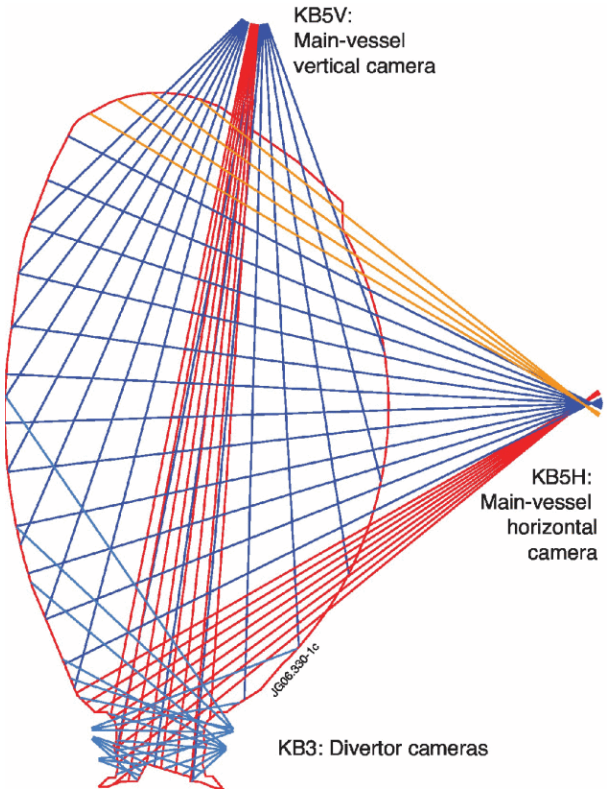

Figure 4.13: Bolometer chords on JET that were used with the DeCNN (8).

In Fig. 4.12, a transposed convolution refers to a convolutional layer were the images are first artificially increased to higher resolution without adding any information (for example, a single pixel becomes four pixels all having the same value as the original). Following the transposing of the images, the convolutional filters are applied. Essentially, a transposed convolution is the inverse of a regular, unpadded convolution in the sense that if a sliding window would be applied to the output, the result would be the feature map given as the input. This resolution enhancement action coupled with convolutional layers allows this method to work and is frequently used in image resolution enhancement neural networks (37; 38).

The JET DeCNN was then trained on over 27k bolometer inversions that were produced from taken data from 2011 to 2016 and inverted using advanced methods such as the Tikhonov regularization discussed above. The trained DeCNN was able to accurately reproduce inversions taken from a set of data that was not used for training. The computational benefit of the DeCNN was showcased in that the bolometer signals were inverted in milliseconds as compared to the approximate hour needed for the traditional methods.

4.5 CTH DeCNN

Having discovered the success of the DeCNN bolometer inversion method, a similar effort was undertaken for the new CTH bolometers. Using the known chordal arrangement of CTH bolometers (see Fig. 4.4), a DeCNN was constructed having an architecture mimicking the JET DeCNN. The CTH DeCNN is visualized in Fig. 4.14 with 60 input signals and an output of 96 x 96 pixel emissivity grid. First, there are two fully connected (FC) layers with 4320 neurons each. The output of the second FC layer is reshaped into a 30 x 12 x 12 matrix effectively creating 30 feature maps each being 12 x 12 pixels. This reshaping is followed by three consecutive transposed convolutions where in each step the feature maps have their resolution artificially increased (quadrupling the number of pixels) followed by a convolution. After the three transposed convolutions, which results in 30 feature maps each having 96 x 96 pixels, a final convolution collapses the 30 feature maps into one 96 x 96 output image. The CTH DeCNN has a total of 19,065,451 trainable parameters. The final resolution of the output image (96 x 96 pixels) was selected to be able to fully fit a complete training set of images onto the available training GPU which possesses significantly less memory than the one used by the researchers at JET.

4.5.1 Synthetic Data Trained DeCNN

Having constructed a DeCNN for CTH bolometers, the remaining step is to train the DeCNN. However, unlike the researchers at JET, no previously existing, high quality bolometer inversions of real data are available. Because of the long computational times (typically up to an hour) needed for each bolometer inversion using a high quality technique such as Tikhonov regularization (which currently has not been applied to the CTH bolometers), the decision was made to attempt to train the DeCNN using synthetic data, a method that has been explored in CNNs (39; 40) but not in DeCNNs.

The goal of synthetic data, meant for training purposes, is that of domain randomization (40). Domain randomization means randomly sampling each data sample's domain attributes from a predefined space of domain attributes while creating a dataset for training purposes. For

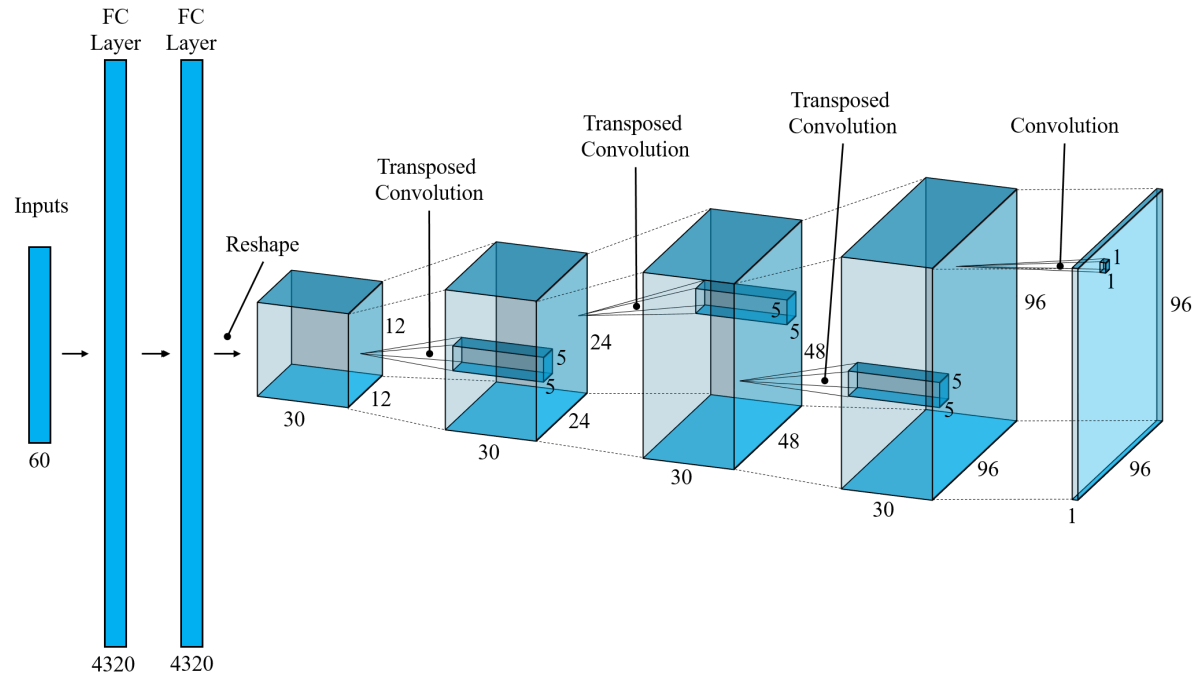

Figure 4.14: De-Convolutional Neural Network (DeCNN) for the CTH bolometer arrays.

example, while training a CCN to recognizes hand-written letters of the alphabet, we would produce a training set that contains hand-written letters samples taken from the full alphabet (the full domain) not just from a subset of the alphabet (such as the first ten letters).

However, while pure randomization can achieve sufficient results given a large enough training set, for computational efficiency, a model can be developed such that the design of the model allows the randomization of its parameters that produces enough domain randomization to solve the problem at hand. Some researchers have drawn the conclusion that neural networks trained on synthetic data are examples of model-based reasoning drawing formal connections with Bayesian modeling (39). In that, training a neural network with synthetic data is equivalent to performing proposal adaptation for importance sampling inference in the synthetic data generative model.

For the CTH DeCNN, we follow the model based approach. After many iterations, this model took the form of a magnetic flux surface hollow profile with a single randomized Gaussian hotspot. Fig. 4.15 gives two examples of flux surfaces commonly found in CTH. In practice, we took a set of 20 reconstructed flux surfaces from which one can be randomly selected.

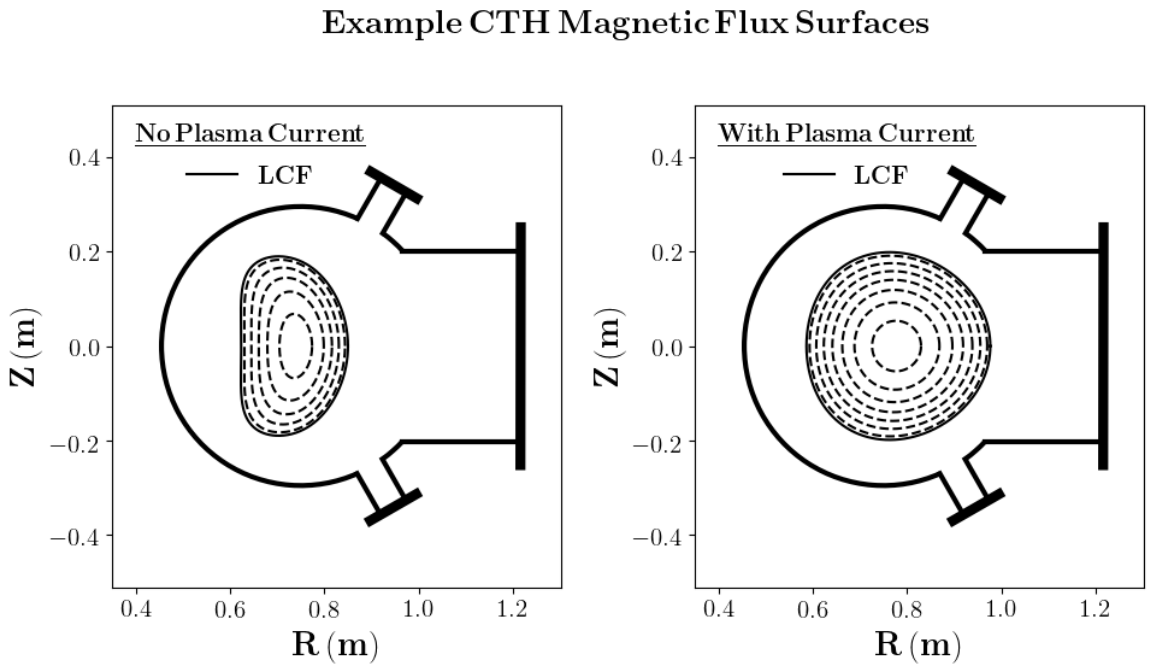

Figure 4.15: CTH magnetic flux surfaces reconstructed by V3FIT having zero and modest plasma current levels.

The selected flux surface was additionally randomly scaled radially in addition to being horizontally and vertically translated. Next, a hollow profile was randomized in magnetic flux surfaces coordinates and projected onto the flux surfaces. Finally, a random hotspot was added to account for the known appearance of non constant flux surface bolometer emission on CTH.

Figs. 4.16 and 4.17 give four randomly sampled examples from the training set of synthetic images. For each example, the pixel grid was produced according to the randomization algorithm detailed above and then, knowing the projections matrix (**T** from Eq. 4.5), the synthetic signals were calculated. Both synthetic pixels grids and their corresponding signals are used to train the DeCNN in a supervised fashion.

In total, sixty thousand synthetic samples were generated. Some statistics from the training examples are shown in Fig. 4.18. The average and median values produce an expected hollow profile with a large standard deviation. The deviation is beneficial because the ultimate goal is domain randomization allowing the trained DeCNN to be adequately generalized.

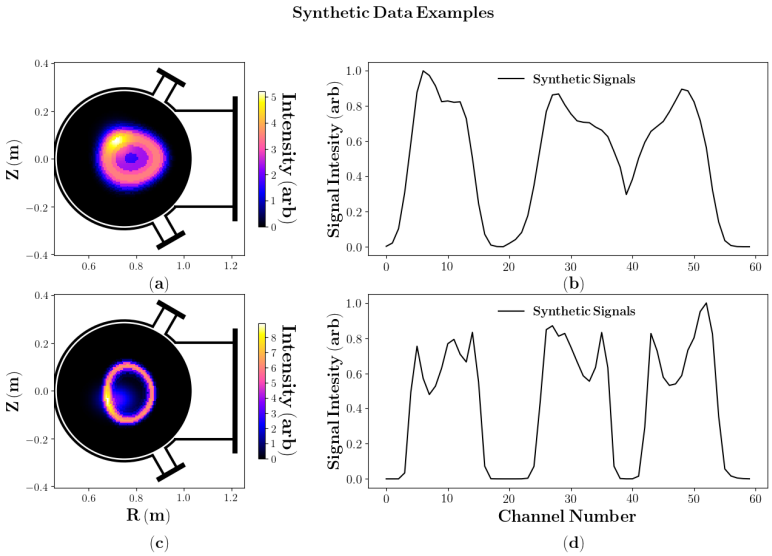

Figure 4.16: First set of example synthetic data produced for training the DeCNN for CTH bolometers. This set demonstrates the impact of the plasma emissivity randomness on the resulting synthetic signals.

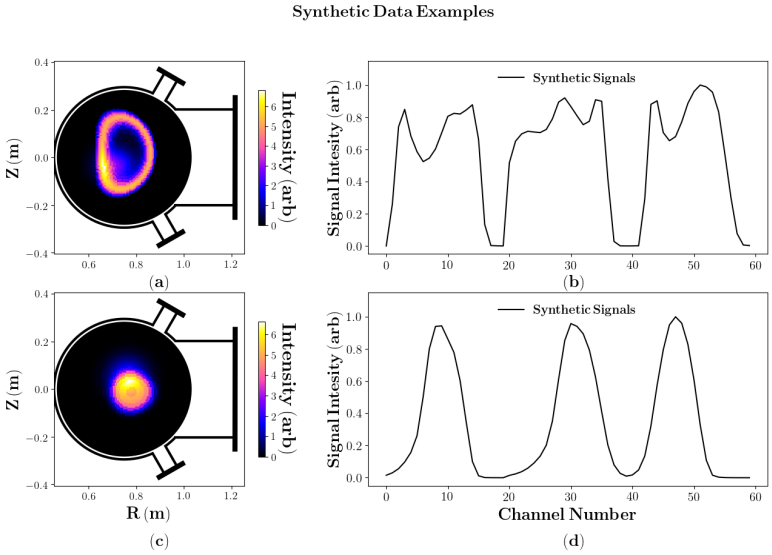

Figure 4.17: Second set of example synthetic data produced for training the DeCNN for CTH bolometers. This set demonstrates how a slightly hollow emissivity (c) produces synthetic signals (d) that are indistinguishable from peaked profile.

4.5.2 Customizing Loss Functions for Enhanced Training

Having assembled the synthetic data, the DeCNN was trained using a GTX 970 graphics card (41) over 400 epochs. An epoch is one complete cycle through the training data. The training

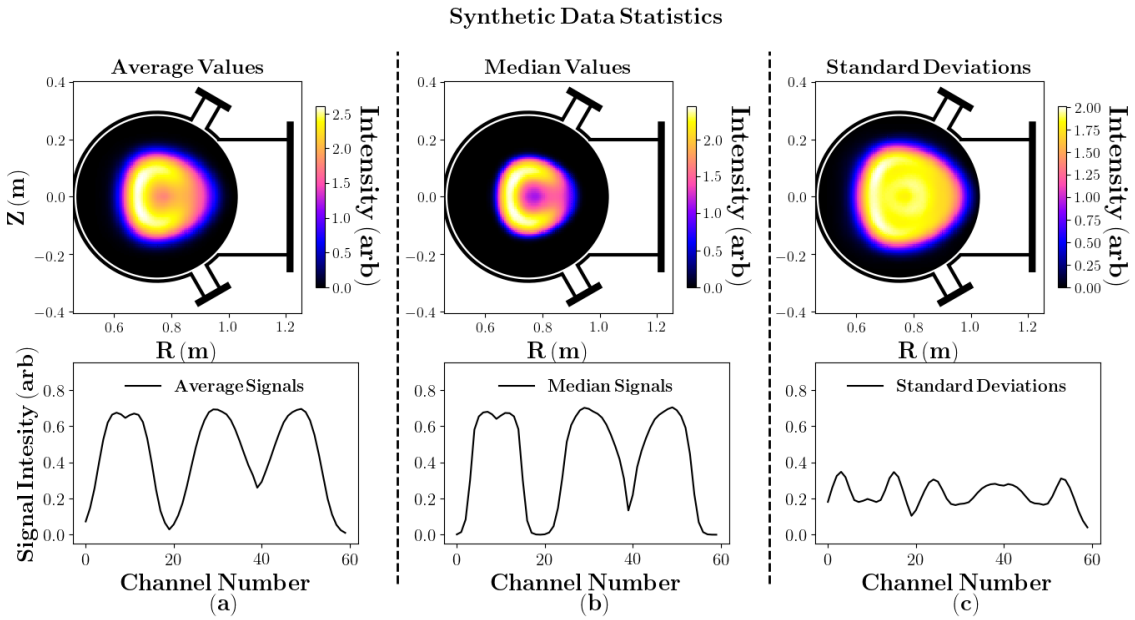

Figure 4.18: Statistics of the synthetic data used to train the CTH DeCNN. On the left (a) is the average values for the pixel grids as well as the average signals, middle (b) has the median values, and right (c) has the standard deviation of the data set.

duration of 400 epochs was based on the Jet DeCNN work training example and proved to be sufficient for this work. In order to evaluate the training progress, the data set was split in a 9-1 way between the training set (90%) and validation set (10%). As the training algorithm progresses, the DeCNN and its parameters are only saved if there is improvement in the loss of the validation set. The loss function is the object to be minimized by the training and can take any form. For this work, the Mean Absolute Error (MAE) was used. MAE is defined as

$$MAE = \frac{1}{n}\left(\sum_{i=1}^{n} |y_i - x_i|\right) \tag{4.17}$$

where y_i is the prediction, x_i is the true value, and n is the number of comparisons.

For training, two runs were performed. The first loss function used MAE to compare the training pixel grids to the grids output by the DeCNN and is as follows

$$\mathcal{L}_{\mathbf{G}} = \frac{1}{n}\left(\sum_{i=1}^{n} |\mathbf{g}_{\text{DeCNN},i} - \mathbf{g}_{\text{Training},i}|\right) \tag{4.18}$$

where $\mathcal{L}_{\mathbf{G}}$ is the loss, $\mathbf{g}_{\text{DeCNN},i}$ is the emissivity grid output by the DeCNN, and $\mathbf{g}_{\text{Training},i}$ is the corresponding training example.

The second training run implemented a custom loss function that incorporated the comparison of the training signals and the signals evaluated using Eq. 4.5 on the DeCNN output. The custom loss is defined as

$$\mathcal{L}_{\textbf{custom}} = \mathcal{L}_{\mathbf{G}} + \mathcal{L}_{\mathbf{b}} \tag{4.19}$$

where the custom loss $\mathcal{L}_{\textbf{custom}}$ is the sum of the previous loss function $\mathcal{L}_{\mathbf{G}}$ (Eq. 4.18) and $\mathcal{L}_{\mathbf{b}}$ is the MAE signal loss calculated from training signals and the DeCNN output. The signal loss $\mathcal{L}_{\mathbf{b}}$ is defined as

$$\mathcal{L}_{\mathbf{b}} = \frac{1}{n}\left(\sum_{i=1}^{n} |\mathbf{T}\mathbf{g}_{\text{DeCNN},i} - \mathbf{b}_{\text{Training},i}|\right) \tag{4.20}$$

where $\mathbf{T}$ is the projection matrix (Eq. 4.3), $\mathbf{g}_{\text{DeCNN},i}$ is the DeCNN output, and $\mathbf{b}_{\text{Training},i}$ is the training example signal.

Fig. 4.19 shows the comparison of the training histories for the two different training runs. While the total loss for the custom loss function training (Fig. 4.19(b)) is higher, this loss is the sum of two loss functions. If we compare same grid MAE from each run, we see in Fig. 4.20 the custom loss function training actually reaches a lower validation set loss indicating a better generalization of the DeCNN.

In order to prevent overfitting of the training data, it is customary to declare a CNN or DeCNN as trained when the validation set loss becomes relatively flat. Past that point, the training set loss may continue to decrease, but it is past the practical point of generalization and starts overfitting the training data. For this work, we selected epoch 250 for the built-in loss function and epoch 300 for the custom loss function as the points where the DeCNNs were considered trained.

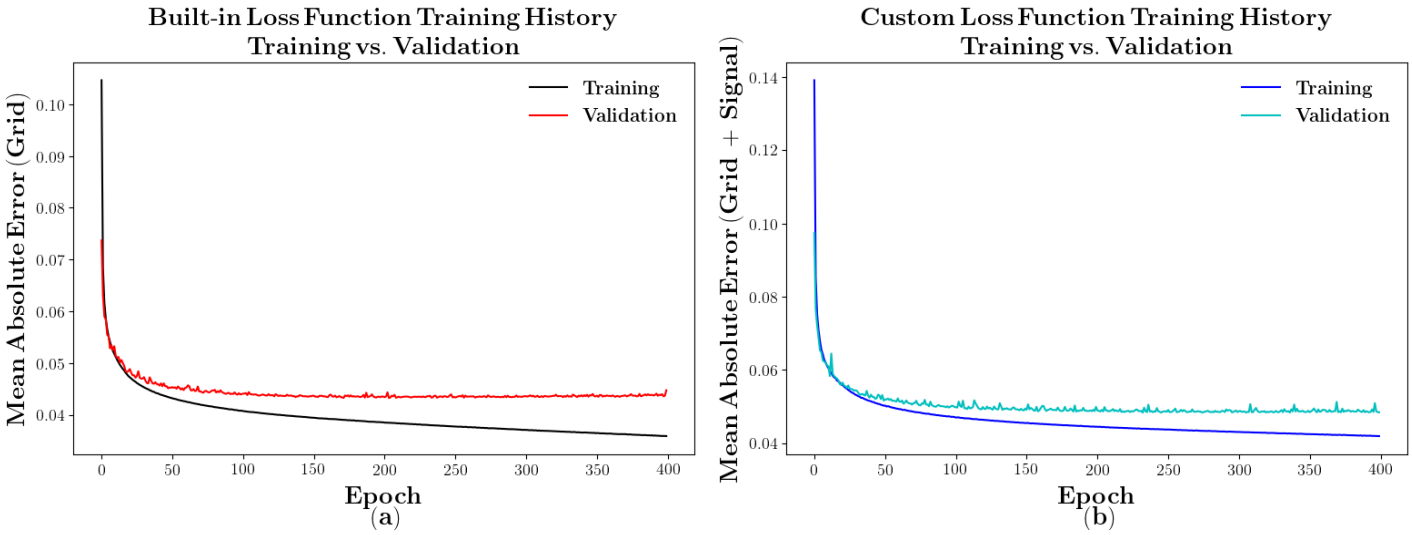

Figure 4.19: The training histories are plotted using the built-in loss function (a) and the custom loss function (b).

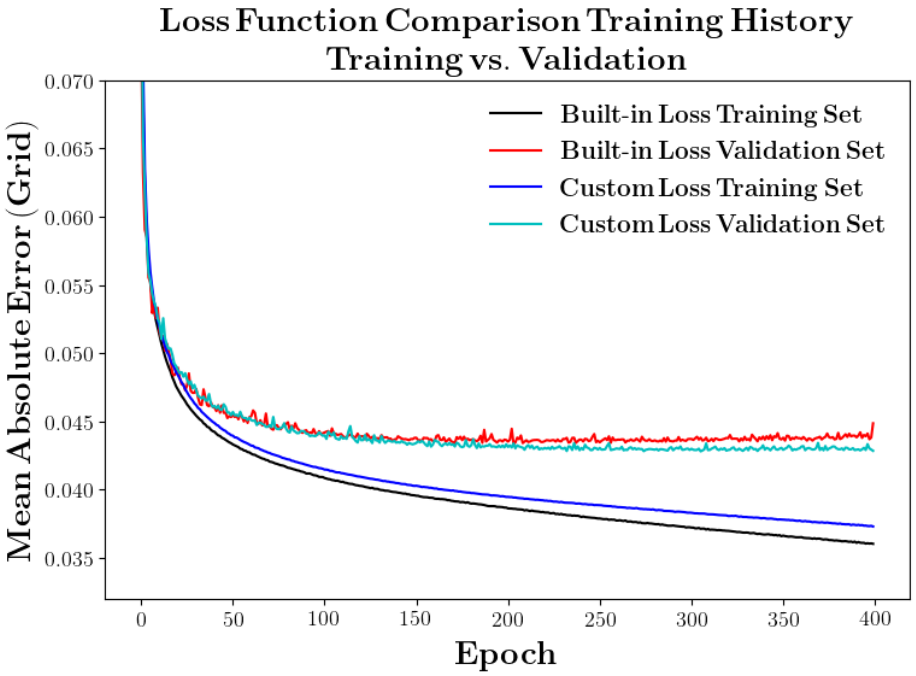

Figure 4.20: A direct comparison of the Mean Absolute Errors between the output pixel grid and its target for the built-in loss function and custom loss function training.

4.5.3 CTH DeCNN Applied to Real Data

Possessing two trained DeCNNs, we can compare their performance on real bolometer data. Fig. 4.21 shows the magnetic flux surface inversion (a), the built-in loss function DeCNN inversion (b), and the custom loss function DeCNN inversion (c). As anticipated, the DeCNN

inversions produces a significantly different emissivity grid than the magnetic flux surface inversion. The asymmetry of the bolometer emission seen in Fig. 4.4 is captured by the increased plasma emissivity at the top of plasma for the DeCNN inversions. Confirming this, the measured and inverted signals across the bottom row of Fig. 4.21 show a much closer fit than the magnetic flux surface inversion.

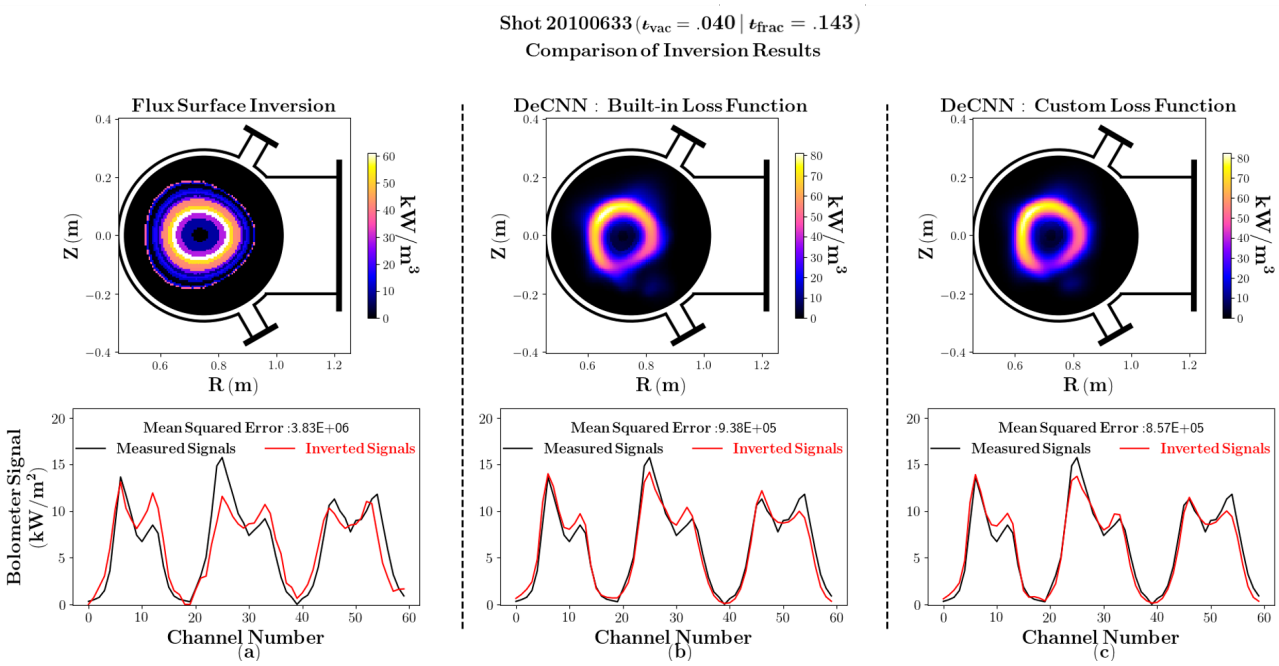

Figure 4.21: A comparison of the De-Convolutional Neural Networks (DeCNNs) trained for the CTH bolometers. With the magnetic flux surface inversion being shown (a) as a comparison, the two trained DeCNN inversions are shown. The Mean Squared Error (MSE) is calculated for the input signals and signals calculated from the inversion output.

Looking at the measured and inverted signals in Fig. 4.21, the custom loss function DeCNN produces the lowest Mean Squared Error (MSE) which is defined as

$$MSE = \frac{1}{n}\left(\sum_{i=1}^{n}(y_i - x_i)^2\right) \tag{4.21}$$

where y_i is the prediction, x_i is the true value, and n is the number of comparisons. This evidence validates what was seen in Fig. 4.20, namely that the DeCNN trained with the custom loss function was more generalized (ie. better trained) than the one using the built-in loss function. With this conclusion, unless otherwise specified, the custom loss function DeCNN is the one being used in the following sections.

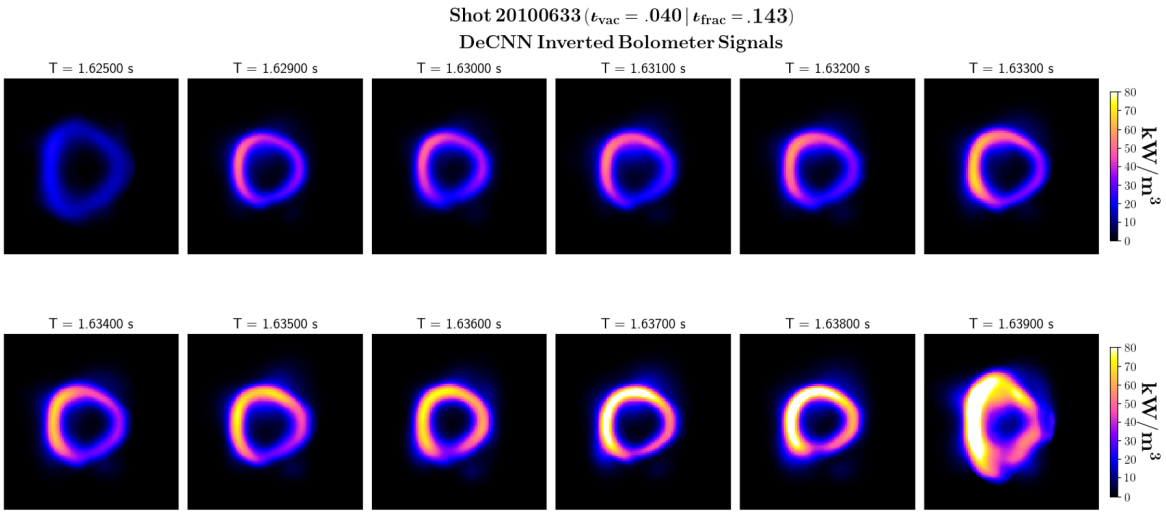

Figure 4.22: The DeCNN inverted bolometer signals are shown twelve times across a disrupting discharge on CTH. For this shot, the plasma density is continuously increasing until the disruption ($T = 1.6384\,s$).

Utilizing the quick inversion times of the DeCNN (each inversion is less than a second), the bolometer signals for a complete plasma discharge can be inverted. Fig. 4.22 shows twelve bolometer inversions taken from a plasma discharge that ends in a density limit disruption. In the first inversion ($T = 1.625\,s$), the plasma current is still ramping up producing a ring of emission that has a larger radius than the following inversions. Going forward in time, the shape solidifies, and as the density of the plasma increases so does emission. Leading up to the disruption ($T = 1.6384\,s$), the ring of emission appears to slowly contract radially inward. Just after the disruption, the bolometer emission reaches its highest intensity (inversion at $T = 1.639\,s$) as the plasma confinement is lost.

In Fig. 4.4, fluctuations can been seen in the bolometer signals. To invert only the bolometer fluctuations and not the total signal, the bolometer signal's background (slowly or non-varying component) was determined using singular value decomposition (SVD) to find the strongest non-varying spatial and temporal mode. A more detailed discussion of SVD is provided in Sec. 5.3. Inputting both the background signal and the total signal into the DeCNN, two inversions were produced. Subtracting the background inversion from the total signal inversion, the inverted bolometer fluctuations were isolated. Fig. 4.23 shows the inverted fluctuations at ten consecutive, even-spaced times. The resulting fluctuations at the outermost radial

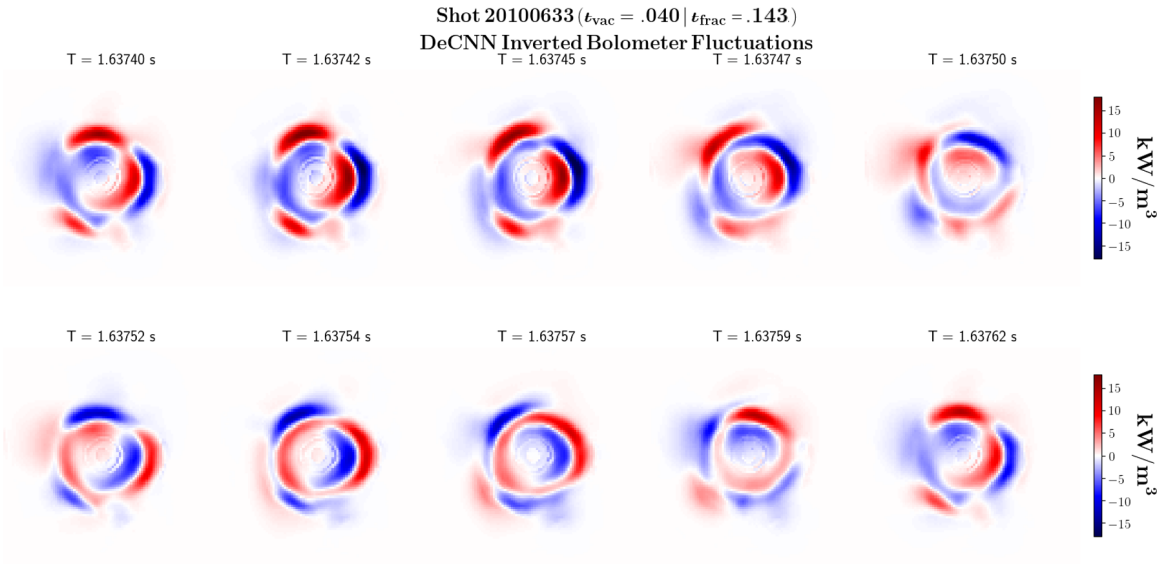

Figure 4.23: Inverted bolometer fluctuation resulting from the subtraction of a SVD calculated background, inverted by DeCNN, from the total bolometer DeCNN inverted emissivity.

position (away from the center of the plasma) have two hotter spots (red in plot) and two cooler spots (blue in plot). This pattern, with the outermost fluctuations having a $m = 2$ structure and the innermost fluctuations having a $m = 1$ structure, rotates counter-clockwise, the positive poloidal angle direction, about the magnetic axis. A second fluctuation pattern can be seen at a more radially inward location and possesses one peak and one valley, This second pattern appears to rotate synchronously with the first.

In addition to gaining spatial information from bolometer signal fluctuations, the inverted bolometer signals can be used to estimate the total radiated power from the plasma. Using Eq. 4.6, the inverted bolometer emissivity can be summed then multiplied by the major radius circumference to get the total radiated power approximation. Fig. 4.24 compares the total radiated power calculated from the magnetic flux surface inversion and the DeCNN inversion. The database of shots used in Fig. 4.24 is taken from density limit disruptions performed with deuterium. In general, the powers are close to each other and well within the diagnostic uncertainties (not shown). This result serves to validate the usefulness of the DeCNN inversion method for total radiated power estimates. With its quick computational times, the DeCNN-based approach could quickly produce the total radiated power for a complete discharge even

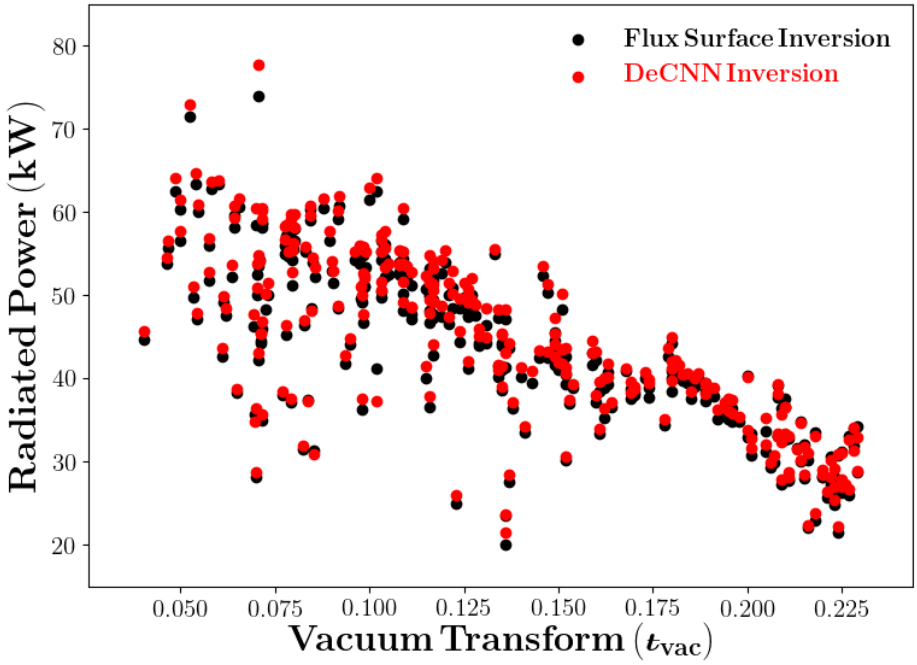

Figure 4.24: The total radiated power estimate is shown using the magnetic flux surface inversion and the DeCNN inversion versus the vacuum rotational transform of CTH.

doing so between typical CTH discharges allowing another tool for CTH operators and coordinators.

4.6 Summary and Future Work

A De-Convolution Neural Network (DeCNN) has been developed for the bolometer arrays on the Compact Toroidal Hybrid (CTH) at Auburn University. This DeCNN, while structurally similar to DeCNNs developed elsewhere, is fundamentally different because of the absence of pre-existing bolometer emissivity reconstructions. Without pre-existing high quality bolometer inversions available, the DeCNN was trained using synthetic data. With a goal of domain randomization, synthetic data was developed that produced a trained DeCNN that was well generalized and produced better results on real bolometer data than a magnetic flux surface inversion. In addition, a custom loss function was introduced that produced a better trained DeCNN than one that used the built-in loss function.

This new DeCNN approach allows for quicker bolometer inversions and the ability to study the fluctuations seen in the bolometer data. The fluctuation pattern rotates in the positive poloidal angle direction with a frequency of approximately $5kHz$. Using the DeCNN inversion, the total radiated power can be calculated quickly and was found to be in good agreement with previous methods.

In the future, without the long computational times, the DeCNN based total radiated power could be used as a runday diagnostic for CTH operators and coordinators. Seeing a ring of emissivity in the background bolometer inversion, it might be possible extract contours of constant bolometer emissivity to use as a proxy for magnetic flux surfaces to invert the interferometer (42) density measurements to get a plasma density profile.

A DeCNN meant for SXR inversions could also be trained using synthetic data that allowed peak profiles. In addition, a Tikhonov regularization using various functionals, such as the Minimum Fisher Information, could be developed to provide a higher quality check of the DeCNN inversions. Also, because domain randomization of synthetic data has been linked to model-based Bayesian formalism, the developement of a Bayesian inversion method, with or without a model basis, would further illustrate the potential of the synthetically-trained DeCNN inversion method.

The inclusion of additional bolometer arrays, such as a six bolometer (each with 20 channels) array setup to be poloidally symmetric and at a different toroidal location than the existing array, with its subsequently trained DeCNN inversion, would allow both an even more accurate total radiated power estimate and an opportunity to track bolometer emission moving toroidally across the plasma. This additional bolometer information could be coupled with magnetic diagnostics using a Siesta-based V3FIT (43; 44) reconstruction to attempt to map magnetic islands with bolometer emission.

References

[1] J. Mlynar, T. Craciunescu, D. R. Ferreira, P. Carvalho, O. Ficker, O. Grover, M. Imrisek, and J. Svoboda, "Current research into applications of tomography for fusion diagnostics," *Journal of Fusion Energy*, vol. 38, no. 3-4, p. 458–466, 2019.

[2] A. M. Cormack, "Representation of a function by its line integrals, with some radiological applications," *Journal of Applied Physics*, vol. 34, no. 9, pp. 2722–2727, 1963.

[3] I. H. Hutchinson, *Principles of plasma diagnostics*. Cambridge, 2002.

[4] A. Tikhonov, *Soviet Mathmatics Doklady*, vol. 5. USSR Academy of Sciences, 1963.

[5] M. Anton, H. Weisen, M. J. Dutch, W. von der Linden, F. Buhlmann, R. Chavan, B. Marletaz, P. Marmillod, and P. Paris, "X-ray tomography on the TCV tokamak," *Plasma Physics and Controlled Fusion*, vol. 38, pp. 1849–1878, nov 1996.

[6] T. Wang, D. Mazon, J. Svensson, D. Li, A. Jardin, and G. Verdoolaege, "Gaussian process tomography for soft x-ray spectroscopy at west without equilibrium information," *Review of Scientific Instruments*, vol. 89, no. 6, p. 063505, 2018.

[7] D. R. Ferreira, P. J. Carvalho, H. Fernandes, and J. Contributors, "Full-pulse tomographic reconstruction with deep neural networks," *Fusion Science and Technology*, vol. 74, no. 1-2, pp. 47–56, 2018.

[8] D. R. Ferreira, P. J. Carvalho, and H. Fernandes, "Deep learning for plasma tomography and disruption prediction from bolometer data," *IEEE Transactions on Plasma Science*, vol. 48, no. 1, pp. 36–45, 2020.

[9] J. D. Hanson, S. F. Knowlton, B. A. Stevenson, and G. J. Hartwell, "Equilibrium and stability of current-carrying discharges in the non-axisymmetric cth experiment," *Contributions to Plasma Physics*, vol. 50, no. 8, pp. 724–730, 2010.

[10] J. Hanson, D. Anderson, M. Cianciosa, P. Franz, J. Harris, G. Hartwell, S. Hirshman, S. Knowlton, L. Lao, E. Lazarus, L. Marrelli, D. Maurer, J. Schmitt, A. Sontag, B. Stevenson, and D. Terranova, "Non-axisymmetric equilibrium reconstruction for stellarators, reversed field pinches and tokamaks," *Nuclear Fusion*, vol. 53, no. 8, p. 083016, 2013.

[11] J. Herfindal, J. Dawson, D. Ennis, G. Hartwell, S.D.Loch, and D. Maurer, "Design and initial operation of a two-color soft x-ray camera system on the compact toroidal hybrid experiment," *Review of Science Instrument*, vol. 85, no. 11, 2014.

[12] X. Ma, M. R. Cianciosa, D. A. Ennis, J. D. Hanson, G. J. Hartwell, J. L. Herfindal, E. C. Howell, S. F. Knowlton, D. A. Maurer, P. J. Traverso, and et al., "Determination of current and rotational transform profiles in a current-carrying stellarator using soft x-ray emissivity measurements," *Physics of Plasmas*, vol. 25, no. 1, p. 012516, 2018.

[13] J. Schilling, H. Thomsen, C. Brandt, S. Kwak, and J. Svensson, "Soft x-ray tomograms are consistent with the magneto-hydrodynamic equilibrium in the wendelstein 7-x stellarator," *Plasma Physics and Controlled Fusion*, vol. 63, p. 055010, mar 2021.

[14] J. L. Herfindal, D. A. Maurer, G. J. Hartwell, D. A. Ennis, J. D. Hanson, S. F. Knowlton, X. Ma, M. D. Pandya, N. A. Roberds, P. J. Traverso, and et al., "Sawtooth oscillation behavior with varying amounts of applied stellarator rotational transform," *Physics of Plasmas*, vol. 26, no. 3, 2019.

[15] M. Odstrcil, J. Mlynar, T. Odstrcil, B. Alper, and A. Murari, "Modern numerical methods for plasma tomography optimisation," *Nuclear Instruments and Methods in Physics Research Section A: Accelerators, Spectrometers, Detectors and Associated Equipment*, vol. 686, pp. 156–161, 2012.

[16] A. N. Henrik, "Résolution dun probleme de mécanique," *J. Reine u. Angew. Math*, 1826.

[17] W. H. Richardson, "Bayesian-based iterative method of image restoration," *Journal of the Optical Society of America*, vol. 62, pp. 55–59, 1972.

[18] Y. LeCun, Y. Bengio, and G. Hinton, "Deep learning," *Nature*, vol. 521, pp. 436–444, May 2015.

[19] A. Krizhevsky, I. Sutskever, and G. E. Hinton, "Imagenet classification with deep convolutional neural networks," in *Advances in Neural Information Processing Systems* (F. Pereira, C. J. C. Burges, L. Bottou, and K. Q. Weinberger, eds.), vol. 25, Curran Associates, Inc., 2012.

[20] K. He, X. Zhang, S. Ren, and J. Sun, "Delving deep into rectifiers: Surpassing human-level performance on imagenet classification," in *2015 IEEE International Conference on Computer Vision (ICCV)*, pp. 1026–1034, 2015.

[21] H. Noh, S. Hong, and B. Han, "Learning deconvolution network for semantic segmentation," in *2015 IEEE International Conference on Computer Vision (ICCV)*, pp. 1520–1528, 2015.

[22] O. Ronneberger, P. Fischer, and T. Brox, "U-net: Convolutional networks for biomedical image segmentation," in *Medical Image Computing and Computer-Assisted Intervention – MICCAI 2015* (N. Navab, J. Hornegger, W. M. Wells, and A. F. Frangi, eds.), (Cham), pp. 234–241, Springer International Publishing, 2015.

[23] Y. P. Chen, Y. Li, and G. Wang, "An enhanced region proposal network for object detection using deep learning method," *PloS one*, vol. 13, pp. e0203897–e0203897, Sep 2018. 30235238[pmid].

[24] K. He, X. Zhang, S. Ren, and J. Sun, "Deep residual learning for image recognition," in *2016 IEEE Conference on Computer Vision and Pattern Recognition (CVPR)*, pp. 770–778, 2016.

[25] I. Goodfellow, Y. Bengio, and A. Courville, *Deep Learning*. MIT Press, 2016. http://www.deeplearningbook.org.

[26] J. Duchi, E. Hazan, and Y. Singer, "Adaptive subgradient methods for online learning and stochastic optimization," *Journal of Machine Learning Research*, vol. 12, no. 61, pp. 2121–2159, 2011.

[27] D. P. Kingma and J. Ba, "Adam: A method for stochastic optimization," in *3rd International Conference on Learning Representations, ICLR 2015, San Diego, CA, USA, May 7-9, 2015, Conference Track Proceedings* (Y. Bengio and Y. LeCun, eds.), 2015.

[28] X. Glorot and Y. Bengio, "Understanding the difficulty of training deep feedforward neural networks," in *Proceedings of the Thirteenth International Conference on Artificial*

Intelligence and Statistics (Y. W. Teh and M. Titterington, eds.), vol. 9 of *Proceedings of Machine Learning Research*, (Chia Laguna Resort, Sardinia, Italy), pp. 249–256, PMLR, 13–15 May 2010.

[29] R. Raina, A. Madhavan, and A. Y. Ng, "Large-scale deep unsupervised learning using graphics processors," in *Proceedings of the 26th Annual International Conference on Machine Learning - ICML '09*, ACM Press, 2009.

[30] A. Coates, B. Huval, T. Wang, D. Wu, B. Catanzaro, and N. Andrew, "Deep learning with cots hpc systems," in *Proceedings of the 30th International Conference on Machine Learning* (S. Dasgupta and D. McAllester, eds.), vol. 28 of *Proceedings of Machine Learning Research*, (Atlanta, Georgia, USA), pp. 1337–1345, PMLR, 17–19 Jun 2013.

[31] T. T. D. Team, R. Al-Rfou, G. Alain, A. Almahairi, C. Angermueller, D. Bahdanau, N. Ballas, F. Bastien, J. Bayer, A. Belikov, A. Belopolsky, Y. Bengio, A. Bergeron, J. Bergstra, V. Bisson, J. B. Snyder, N. Bouchard, N. Boulanger-Lewandowski, X. Bouthillier, A. de Brébisson, O. Breuleux, P.-L. Carrier, K. Cho, J. Chorowski, P. Christiano, T. Cooijmans, M.-A. Côté, M. Côté, A. Courville, Y. N. Dauphin, O. Delalleau, J. Demouth, G. Desjardins, S. Dieleman, L. Dinh, M. Ducoffe, V. Dumoulin, S. E. Kahou, D. Erhan, Z. Fan, O. Firat, M. Germain, X. Glorot, I. Goodfellow, M. Graham, C. Gulcehre, P. Hamel, I. Harlouchet, J.-P. Heng, B. Hidasi, S. Honari, A. Jain, S. Jean, K. Jia, M. Korobov, V. Kulkarni, A. Lamb, P. Lamblin, E. Larsen, C. Laurent, S. Lee, S. Lefrancois, S. Lemieux, N. Léonard, Z. Lin, J. A. Livezey, C. Lorenz, J. Lowin, Q. Ma, P.-A. Manzagol, O. Mastropietro, R. T. McGibbon, R. Memisevic, B. van Merriënboer, V. Michalski, M. Mirza, A. Orlandi, C. Pal, R. Pascanu, M. Pezeshki, C. Raffel, D. Renshaw, M. Rocklin, A. Romero, M. Roth, P. Sadowski, J. Salvatier, F. Savard, J. Schlüter, J. Schulman, G. Schwartz, I. V. Serban, D. Serdyuk, S. Shabanian, Étienne Simon, S. Spieckermann, S. R. Subramanyam, J. Sygnowski, J. Tanguay, G. van Tulder, J. Turian, S. Urban, P. Vincent, F. Visin, H. de Vries, D. Warde-Farley, D. J. Webb, M. Willson, K. Xu, L. Xue, L. Yao, S. Zhang, and Y. Zhang, "Theano: A python framework for fast computation of mathematical expressions," 2016.

[32] M. Abadi, A. Agarwal, P. Barham, E. Brevdo, Z. Chen, C. Citro, G. S. Corrado, A. Davis, J. Dean, M. Devin, S. Ghemawat, I. Goodfellow, A. Harp, G. Irving, M. Isard, Y. Jia, R. Jozefowicz, L. Kaiser, M. Kudlur, J. Levenberg, D. Mane, R. Monga, S. Moore, D. Murray, C. Olah, M. Schuster, J. Shlens, B. Steiner, I. Sutskever, K. Talwar, P. Tucker, V. Vanhoucke, V. Vasudevan, F. Viegas, O. Vinyals, P. Warden, M. Wattenberg, M. Wicke, Y. Yu, and X. Zheng, "Tensorflow: Large-scale machine learning on heterogeneous distributed systems," 2016.

[33] Y. Jia, E. Shelhamer, J. Donahue, S. Karayev, J. Long, R. Girshick, S. Guadarrama, and T. Darrell, "Caffe: Convolutional architecture for fast feature embedding," in *Proceedings of the 22Nd ACM International Conference on Multimedia*, MM '14, (New York, NY, USA), pp. 675–678, ACM, 2014.

[34] F. Chollet *et al.*, "Keras." https://keras.io, 2015.

[35] N. Srivastava, G. Hinton, A. Krizhevsky, I. Sutskever, and R. Salakhutdinov, "Dropout: A simple way to prevent neural networks from overfitting," *Journal of Machine Learning Research*, vol. 15, no. 56, pp. 1929–1958, 2014.

[36] S. Ioffe and C. Szegedy, "Batch normalization: Accelerating deep network training by reducing internal covariate shift," *CoRR*, vol. abs/1502.03167, 2015.

[37] X. Mao, C. Shen, and Y. Yang, "Image denoising using very deep fully convolutional encoder-decoder networks with symmetric skip connections," *CoRR*, vol. abs/1603.09056, 2016.

[38] C. Ledig, L. Theis, F. Huszár, J. Caballero, A. Cunningham, A. Acosta, A. Aitken, A. Tejani, J. Totz, Z. Wang, and W. Shi, "Photo-realistic single image super-resolution using a generative adversarial network," in *2017 IEEE Conference on Computer Vision and Pattern Recognition (CVPR)*, pp. 105–114, 2017.

[39] T. A. Le, A. G. Baydin, R. Zinkov, and F. D. Wood, "Using synthetic data to train neural networks is model-based reasoning," *CoRR*, vol. abs/1703.00868, 2017.

[40] J. Tremblay, A. Prakash, D. Acuna, M. Brophy, V. Jampani, C. Anil, T. To, E. Cameracci, S. Boochoon, and S. Birchfield, "Training deep networks with synthetic data: Bridging the reality gap by domain randomization," *CoRR*, vol. abs/1804.06516, 2018.

[41] NVIDIA, P. Vingelmann, and F. H. Fitzek, "Cuda, release: 10.2.89," 2020.

[42] M. C. Miller, J. D. Hanson, G. J. Hartwell, S. F. Knowlton, D. A. Maurer, and B. A. Stevenson, "Design and implementation of a multichannel millimeter wave interferometer for the compact toroidal hybrid experiment," *Review of Scientific Instruments*, vol. 83, no. 10, pp. –, 2012.

[43] M. Cianciosa, S. P. Hirshman, S. K. Seal, and M. W. Shafer, "3d equilibrium reconstruction with islands," *Plasma Physics and Controlled Fusion*, vol. 60, p. 044017, mar 2018.

[44] H. Peraza-Rodriguez, J. M. Reynolds-Barredo, R. Sanchez, J. Geiger, V. Tribaldos, S. P. Hirshman, and M. Cianciosa, "Extension of the siesta mhd equilibrium code to free-plasma-boundary problems," *Physics of Plasmas*, vol. 24, no. 8, p. 082516, 2017.

Chapter 5

Density Limit Disruptions on Compact Toroidal Hybrid Experiment

5.1 Introduction

The flexibility of the magnetic configuration of CTH has enabled the performance of experiments on low-q disruptions in hybrid plasmas (1), the impact of three-dimensional magnetic equilibria on sawteething MHD modes (2; 3), and the suppression of vertical instabilities with applied vacuum transform (4). It has allowed an unique opportunity to study density limit disruptions. Density limit disruptions can be observed in plasma discharges ranging from low levels of vacuum rotational transform (tokamak-like CTH) to high levels of vacuum rotational transform (stellarator-like CTH). The goal of this chapter is to extend findings from the previous work on density limit disruptions in CTH and to present recent developments using new diagnostics implemented in this thesis work.

5.2 Reproducibility and Variation of CTH Disruptions

With reproducible parameters, density limit disruptions can be systematically generated in CTH. Fig. 5.1 shows two discharges with similar vacuum transforms but different programmed loop voltages, that disrupt at the same plasma current and density, and exhibit comparable disruption behaviors. The characteristic signature of a tokamak disruption is a positive plasma current spike and negative loop voltage dip which indicate a restructuring of the magnetic flux surfaces and most likely a complete loss of magnetic confinement.

As the vacuum rotational transform is increased, the disruption behavior also changes. Fig. 5.2 shows a comparison of two discharges, one at low vacuum rotational transform (Shot

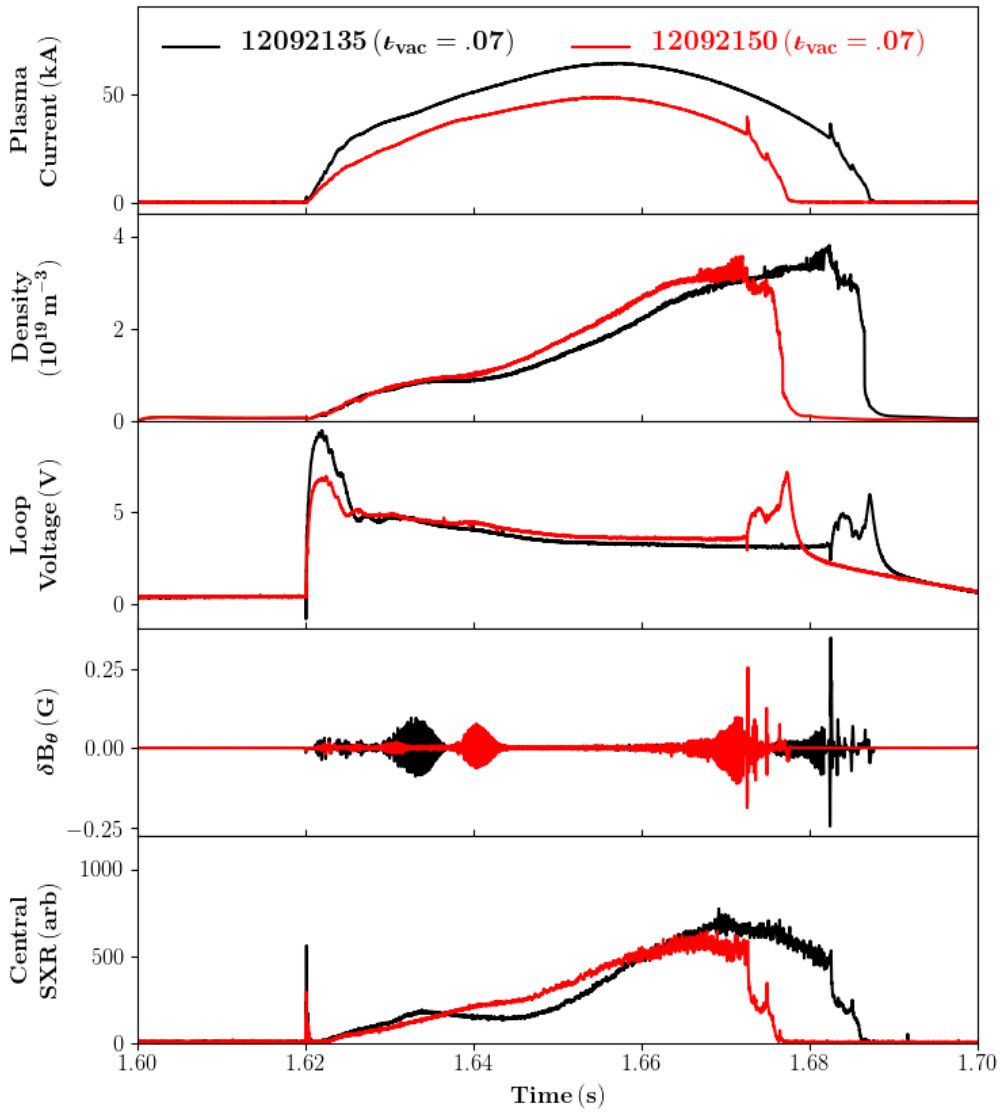

Figure 5.1: Two CTH discharges, having similar values of vacuum transform ($\iota_{vac} = 0.07$), are compared having their plasma current, loop voltage, poloidal magnetic field fluctuations, and core SXR traces plotted. While the discharges have significantly different plasma current evolutions, the disruptions occur at similar plasma currents and densities.

14092626, $\iota_{\text{vac}} = 0.02$) and one at higher vacuum rotational transform (Shot # 14110713, $\iota_{\text{vac}} = 0.11$). While both disrupt at similar densities, the plasma current of the high vacuum transform shot is significantly less at the time of disruption.

In the high transform case, the positive plasma current spike and negative loop voltage dip are significantly weaker than those observed during a low vacuum transform discharge. In addition, all MHD activity, as is seen in the magnetic field fluctuations, is considerably weakened and in some cases undetectable. In the next sections, we will present a case study analysis starting with the low vacuum rotational transform discharges, which exhibit strong tokamak-like phenomena, and ending with the high vacuum rotational transform discharges.

5.3 Low Vacuum Rotational Transform CTH Termination

We find that plasmas exhibit characteristics very similar to density limit disruptions in tokamaks at low vacuum rotational transform ($\iota_{\text{vac}} < 0.1$). The loop voltage and plasma current in CTH are driven by discharging a capacitor bank through an ohmic heating transformer. Fig. 5.3(a) shows a typical low vacuum rotational transform disruption. In CTH, density limit disruptions are initiated by ramping the density as high as possible. The disruptions normally occur as the density is increasing and the plasma current has started to decrease following the peak plasma current. As in tokamaks, CTH disruptions exhibit the signatures of a strong negative loop voltage spike and a positive current spike, followed by a complete collapse of the plasma current.

The bottom two traces in Fig. 5.3(a) show the time evolution of q_{edge} and full-width at half-maximum (*FWHM*) of the plasma current profile, reconstructed with V3FIT from magnetics and soft X-ray data. (5; 6; 7; 8). A narrowing of the reconstructed current profile is observed concurrently with a slight increase in the q_{edge} before the disruption.

To highlight the growth in activity just before the disruption, Fig. 5.3(b) shows plots of the poloidal magnetic field fluctuations, density, and central SXR emission right before the disruption over an expanded time scale. The amplitude of the poloidal magnetic field fluctuations, determined by subtracting the average background field from the total field, grows prior to the disruption. In addition, the chordal density is observed to oscillate synchronously with the

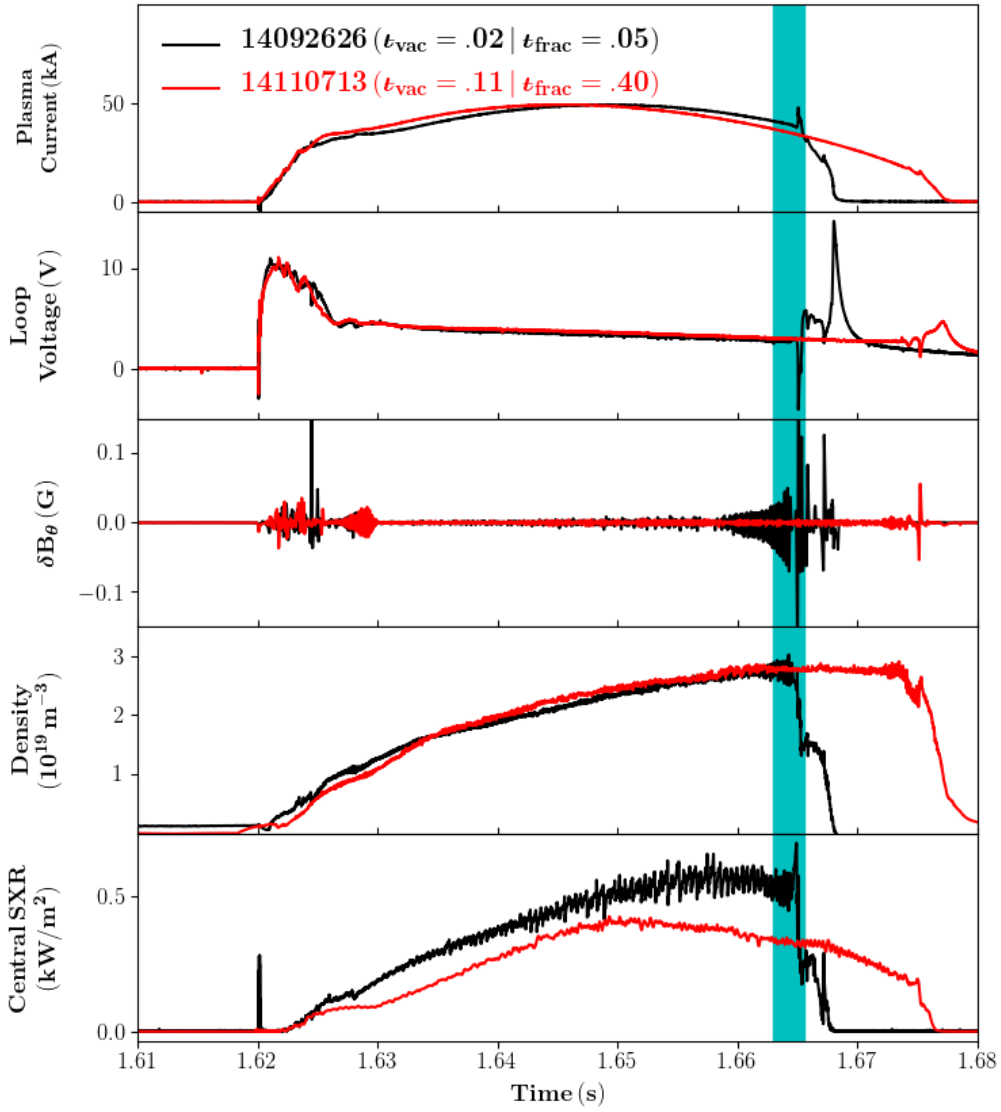

Figure 5.2: Two CTH discharges, one at low vacuum transform ($\iota_{vac} = 0.02$) and one at higher vacuum transform ($\iota_{vac} = 0.11$) Plotted are plasma current, loop voltage, poloidal magnetic field fluctuations, and core SXR traces. While the discharges have similar plasma current evolutions, the terminations occur at similar densities but significantly different plasma currents.

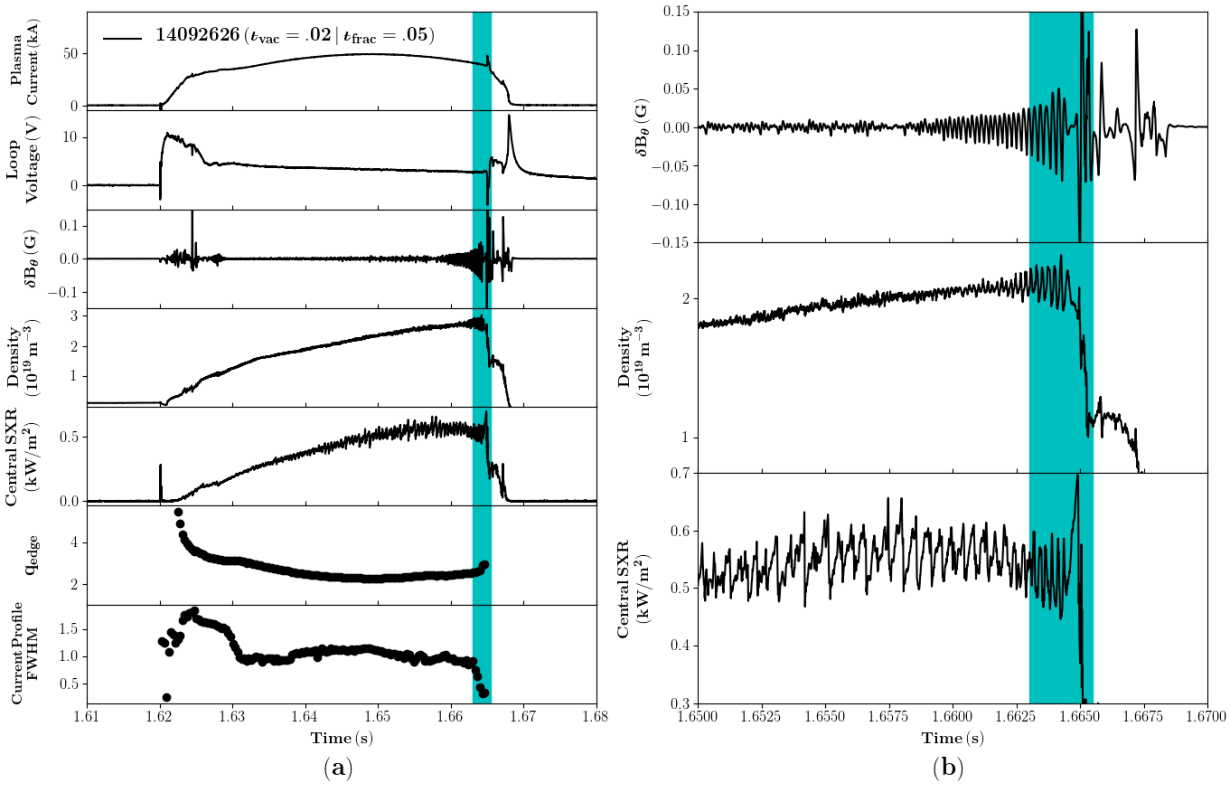

Figure 5.3: CTH disruption having $t_{\text{vac}} = 0.02$ and $t_{\text{frac}} = 0.05$. From top to bottom for (a), are the plasma current I_p, the loop voltage, the poloidal magnetic field fluctuations δB_θ, the line-averaged density n_e, the central soft x-ray (SXR) signal, the V3FIT reconstructed q_{edge}, and the V3FIT reconstructed *FWHM* of the current profile. For (b), the magnetic field fluctuations, the density, and the SXR signals are zoomed-in in time to highlight the fluctuations. The disruption is highlighted in cyan.

magnetic activity. Similarly, the sawtooth activity of the core SXR signal (2; 3) becomes more sinusoidal and also is synchronized with the magnetic oscillations just before the disruption.

The mode numbers of the MHD oscillation are determined with the use of the full array of toroidally and poloidally-distributed Mirnov coils. Fig. 5.6 shows contours plots for the poloidal magnetic field fluctuations from these arrays. The strongest mode observed is the poloidal $m = 2$ mode and the toroidal $n = 1$ mode. This $m/n = 2/1$ mode is the primary edge mode typically seen as precursors to CTH density limit disruptions with low vacuum transform. We note that this behavior is different than that observed previously for low-q disruptions at lower density in CTH in which the $m/n = 2/1$ mode was only rarely observed

and the $m/n = 3/2$ was the dominant mode seen just before disruptions (1). The spatial and temporal information of the MHD modes can be interpreted by biorthogonal decomposition using Singular Value Decomposition (SVD) (9; 10; 11) on the poloidal Mirnov array data.

The singular value decomposition (SVD) technique, also known as biorthogonal decomposition (BD), is used in plasma physics to investigate the spatial and temporal structure of magnetic perturbations (1; 9; 11; 12; 13; 14; 15; 16). SVD decomposes a set of signals evolving in space and time into orthogonal spatial and temporal modes (17), with each spatio-temporal pair weighted by a singular value. This method has been demonstrated to be a robust tool to analyze fluctuations measured by multichannel diagnostics like poloidally and toroidally separated magnetic probes and multi-chord SXR cameras (9; 10; 12; 13; 15). An important feature of this method is that it does not require any assumptions about the spatial structure of the MHD magnetic or SXR mode. If the signals are sinusoidal in both space and time then the result of SVD and Fourier analysis will be identical. Some properties of the SVD method are summarized as follows (12):

1. Rotating modes in the data are represented by degenerate singular values, each with its own spatio-temporal structure;

2. Two or more spatial modes with different structures but rotating with same frequency are identified as single mode by SVD with distorted spatial structure, meaning that SVD cannot distinguish between different MHD modes of same frequency;

3. The singular values that are not related to a coherent spatial or temporal behavior are small in amplitude, and lie in the noise of the signal.

The SVD breaks a rectangular, $m \times n$ matrix, A, into two rectangular matrices, U and V, and a diagonal, $n \times n$ matrix, Σ,

$$A = U\Sigma V^{\dagger}. \tag{5.1}$$

The columns of the signal matrix contain time history of individual channels, while each row is the measured signal by all channels at one instance of time. Consider a signal matrix

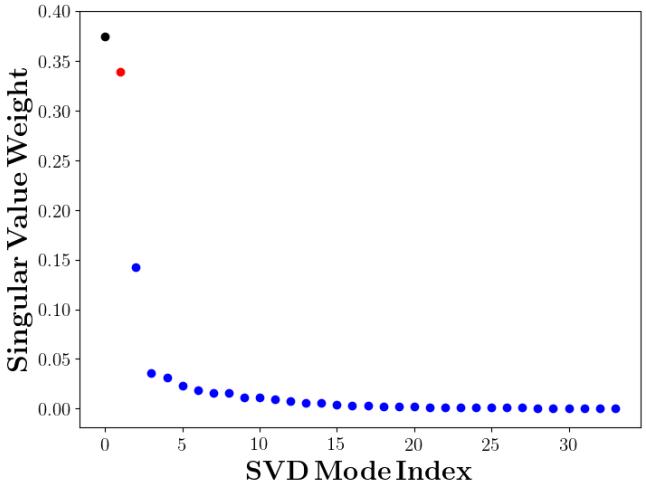

Figure 5.4: The singular values taken from the SVD of the poloidal magnetic field array from shot 14092626 are plotted. The first and second singular values (black and red respectively) appear degenerate possibly indicating a traveling wave.

composed of n channels with m sample points in time, then U can be thought of as a set of n column vectors, u_i, each of length m, while $V^\dagger$ is a set of n row vectors, v_i, again of length m. This can be illustrated in the following way:

$$\underbrace{\begin{bmatrix} \uparrow & \uparrow & & \uparrow \\ s_1 & s_2 & \cdots & s_n \\ \downarrow & \downarrow & & \downarrow \end{bmatrix}}_{Signal\ Matrix} = \underbrace{\begin{bmatrix} \uparrow & \uparrow & & \uparrow \\ u_1 & u_2 & \cdots & u_n \\ \downarrow & \downarrow & & \downarrow \end{bmatrix}}_{Temporal\ Modes} \underbrace{\begin{bmatrix} \sigma_1 & & & \\ & \sigma_2 & & \\ & & \ddots & \\ & & & \sigma_n \end{bmatrix}}_{Singular\ Values/Weights} \underbrace{\begin{bmatrix} \leftarrow & v_1 & \rightarrow \\ \leftarrow & v_2 & \rightarrow \\ & \vdots & \\ \leftarrow & v_n & \rightarrow \end{bmatrix}}_{Spatial\ Modes} \tag{5.2}$$

The result of the decomposition is a set of temporal modes, u_i, arranged in columns, with corresponding singular values or weights, σ_i, and a corresponding set of spatial modes, v_i. The matrix Σ contains the singular values arranged in a descending order. The condition of bi-orthonormality implies that spatial modes are orthonormal, $u_i \cdot u_j = \delta_{i,j}$, and so are temporal modes, $v_i \cdot v_j = \delta_{i,j}$. SVD generates the same number of biorthogonal modes as the number of diagnostic signals used, with the first mode being the most coherent mode in the measurement, and the last mode in most cases is uncorrelated background noise.

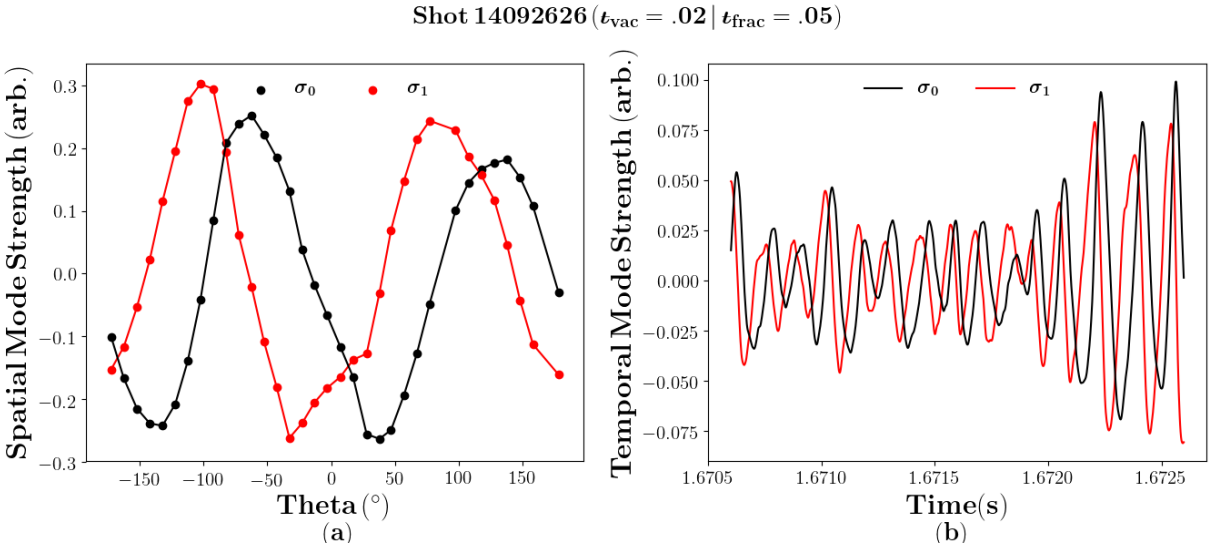

Figure 5.5: The spatial modes (a) and temporal modes (b) for the strongest two SVD modes taken from the SVD of the poloidal magnetic field array from shot 14092626 are shown. The first and second singular values (black and red respectively) exhibit the same spatial (a) and temporal structures (b) with an offset between them confirming that this is a traveling wave.

Applying this SVD technique to the poloidal magnetic field data from shot 14092626, the resulting singular values can be seen in Fig. 5.4. The two strongest SVD modes are degenerate, possibly indicating a traveling mode. Exploring this method further, the temporal and spatial modes for the two strongest SVD modes are shown in Fig. 5.5. Both spatial and temporal modes have similar structure yet offset by about half a phase which confirms that these two SVD modes are a single traveling wave.

To highlight the spatial structure of the traveling wave in the poloidal magnetic field, the right side of Fig. 5.6 shows the spatial structure of these modes in a poloidal cross-section of CTH. On the left of Fig. 5.6, the contour plots of the poloidal magnetic field fluctuations taken from the poloidal and toroidal arrays can be seen. The rotating mode identified by SVD analysis agrees well with the $m = 2$ MHD poloidal mode number of the perturbation seen in the poloidal array.

As shown in Fig. 5.3(b), the magnetic, density, and SXR fluctuations appear to oscillate at the same frquency just prior to the disruption. The density and SXR fluctuations are analyzed using the same SVD technique as for the poloidal magnetic field fluctuations. Fig. 5.7(a) shows the principal frequencies taken from the SVD temporal structure for the strongest SVD modes

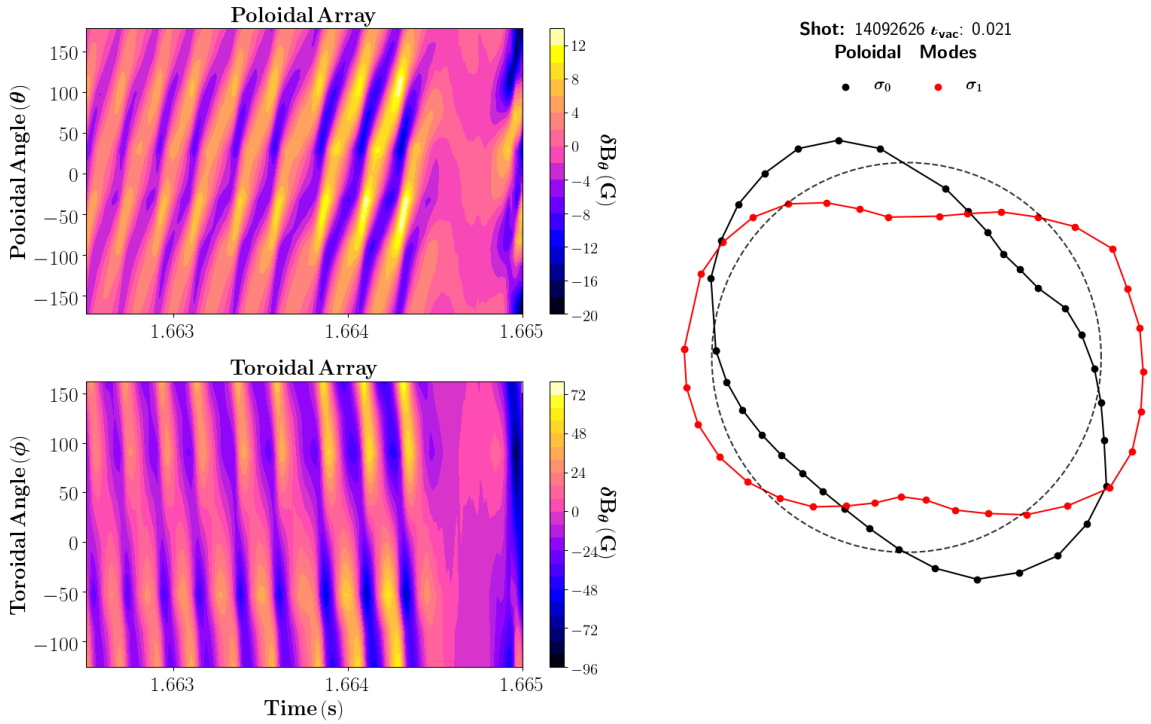

Figure 5.6: (Left) contour plot of fluctuations measured by the poloidal (upper) and toroidal (lower) Mirnov coil arrays s prior to the disruption. (Right), spatial structures from SVD of the poloidal Mirnov array data; each dot represents a B-dot probe. The poloidal structure is represented by a polar plot where the radial excursion is proportional to magnitude of the perturbation and dashed circle represents zero perturbation. The spatial structures are identified by their corresponding singular values (σ_0 and σ_1, degenerate in value).

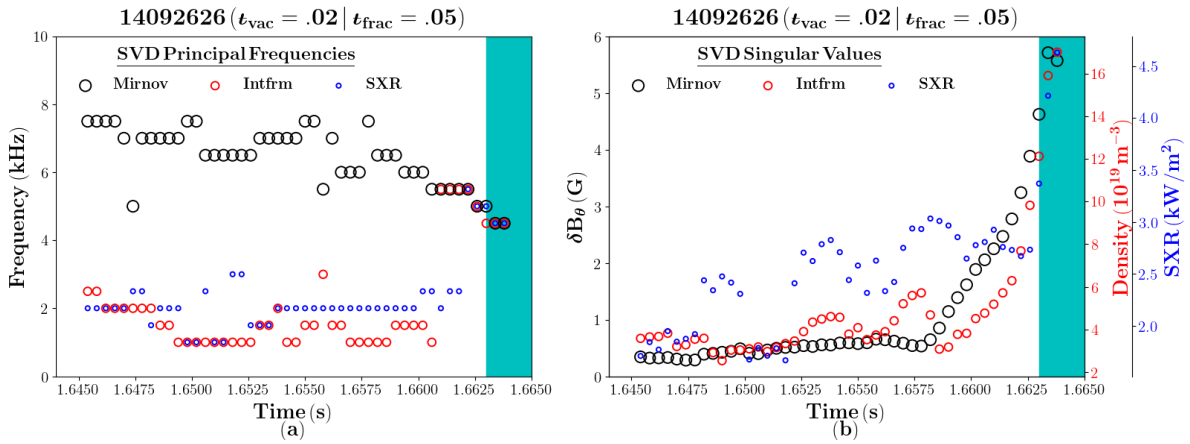

Figure 5.7: The results from the Singular Value Decomposition (SVD) analysis of the magnetic, density, and SXR diagnostics using a moving $2\,ms$ window for shot 14092626 from Fig. 5.3 are shown. For (a), the principal frequencies of the strongest SVD mode for each diagnostic are plotted. For (b), the singular values for the strongest SVD modes are plotted leading up to the disruption. The disruption is highlighted in cyan.

for the magnetic, density, and SXR diagnostics. These frequencies were determined using a Fast Fourier Transform (FFT) on the SVD temporal structures. Fig. 5.7(b) shows the strength of the singular values of the strongest modes in the magnetic, density, and SXR fluctuations. As shown in Fig. 5.7(b), the mode strengths of the three sets of diagnostics increase synchronously just before the disruption. The principal frequencies in Fig. 5.7(a) start to match each other at the same time that the modes start to grow together in Fig. 5.7(b). Our observation is that for low vacuum rotational transform CTH density limit disruptions, the edge MHD $m/n = 2/1$ mode appears to grow until it couples with the core MHD modes (as seen in the sawtooth central SXR signal in Fig. 5.3(b)) which would destroy the nested magnetic flux surfaces and disrupt the plasma.

Because this investigation of low vacuum rotational transform disruptions indicates the apparent growth of a $m/n = 2/1$ MHD mode at the edge of the plasma, the bolometers installed for the work in this thesis were used to study the emission at the plasma edge leading up to a disruption. A recent disruption at low vacuum rotational transform is shown in Fig. 5.8 that includes bolometric data. The activity just before the disruption is consistent with Shot 14092626 (Fig. 5.3) with the magnetic fluctuations growing and the chordal density and central SXR signals oscillating together just before the disruption.

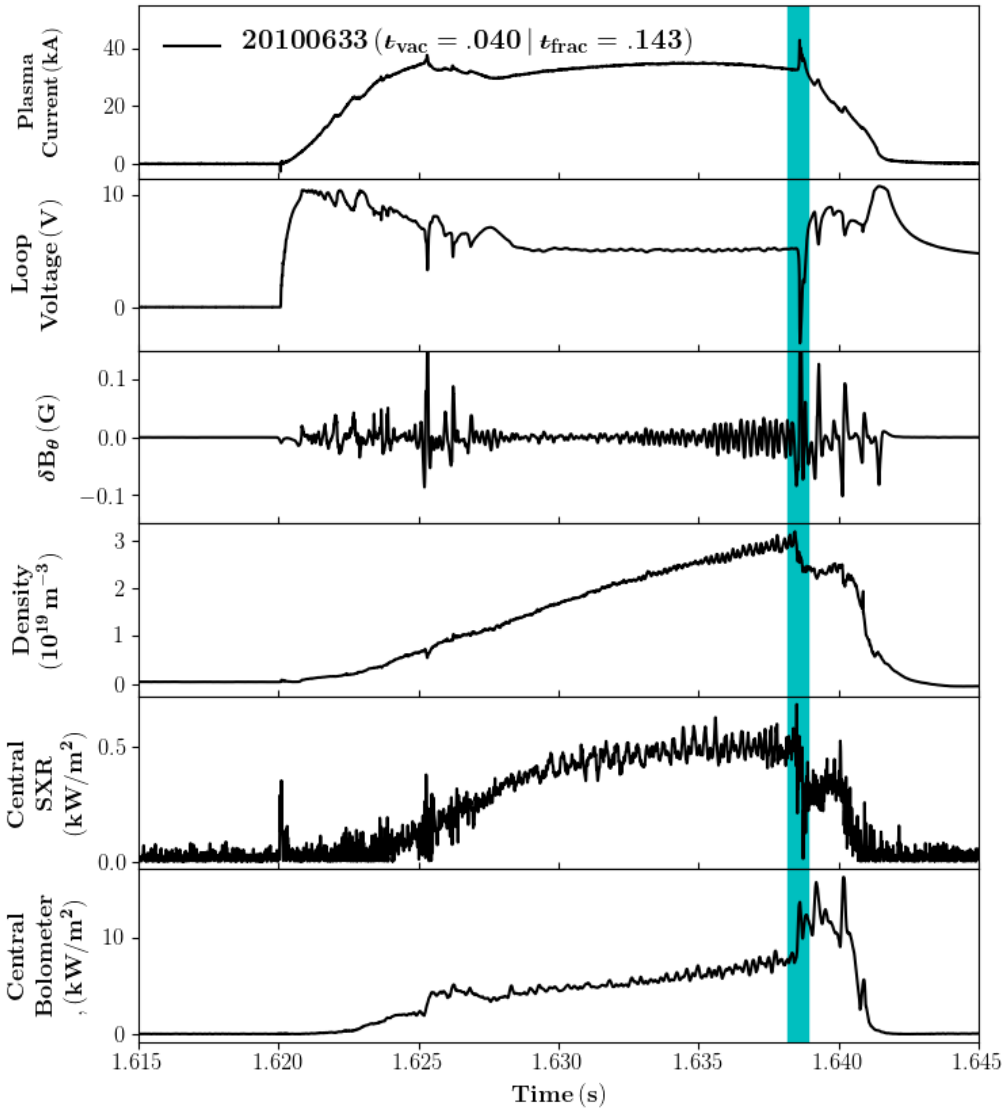

Figure 5.8: CTH disruption 20100633 having $t_{\text{vac}} = 0.040$ and $t_{\text{frac}} = 0.143$. From top to bottom are plasma current I_{p}, the loop voltage,the poloidal magnetic field fluctuations δB

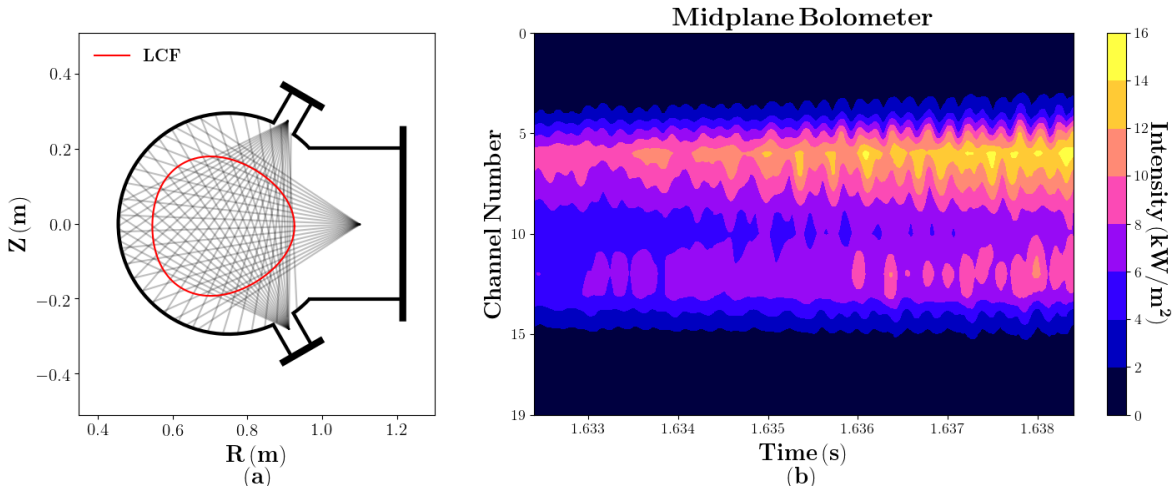

Figure 5.9: Side (a) shows the chords from the newly installed bolometer array with the V3FIT reconstructed last closest flux surface (LCF) in red. Each bolometer possesses 20 chords. For the bolometer located at the midplane ($Z = 0.0\,m$), the top most chord is channel 0 (most upward angled) and the bottom most chord is channel 19 (most downward angled). Side (b) shows the bolometer data in a $6\,ms$ window leading up to the disruption seen in Fig.5.8

Fig. 5.9(a) shows the geometry of the three camera bolometer/SXR array on CTH. The bolometers are located at the poloidal angles of $0°$,$60°$, and $300°$ as measured from the outboard, midplane. Each bolometer has 20 chords. The chord channels for the midplane bolometer are measured top-down with the top most chord being channel 0 (most upward angled) and the bottom most chord being channel 19 (most downward angled). Also plotted in Fig. 5.9(a) is a typical Last Closed Flux surface (LCFS) as generated by VMEC, and the poloidal view of the CTH vacuum vessel at the location of the bolometers. Fig. 5.9(b) provides the up-down chordally-symmetric view of the plasma taken by the midplane bolometer. Because the highest signals from the bolometers are at the upper and lower edges of the plasma, we can infer a hollow profile for the plasma emissivity. We also note the emission at these edges is fluctuating. Seen in Fig. 5.9(b), the channels that view the top of CTH plasmas (channels 0-9) produce an overall stronger signal than that from the bottom-viewing channels (channels 10-19). Density-limit disruptions generally require strong gas puffing to build up the density within the limited time set by the available volt-second ohmic capability of the CTH capacitor bank. The observed bolometer asymmetry, which is only evident in high density discharges, results from the physical location of the gas puffers which are located at the top of CTH.

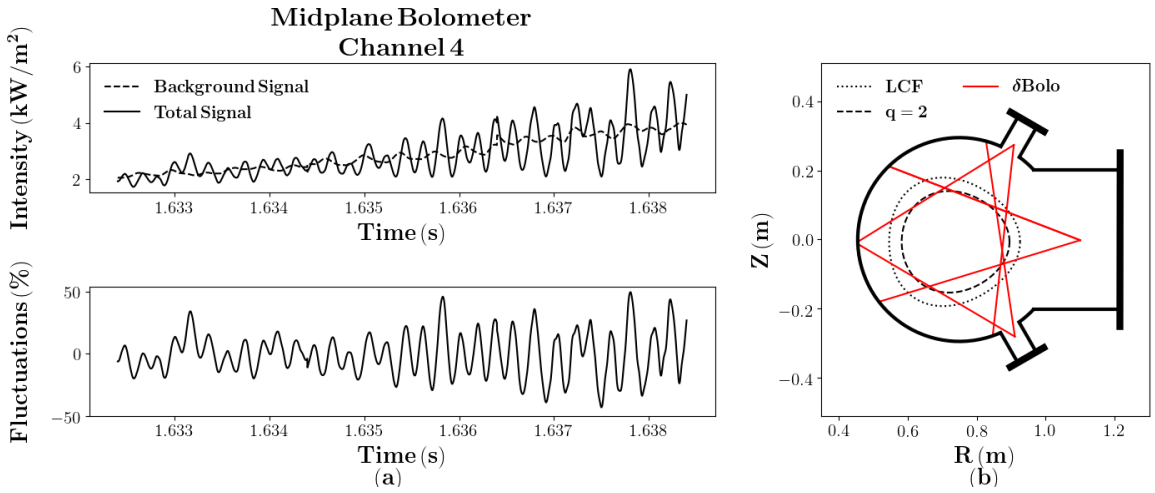

Figure 5.10: The midplane bolometer channel with the largest normalized fluctuations is plotted (a) showing the total signal, the SVD calculated background, and the normalized fluctuations. Using this method, the six channels of largest normalized fluctuations were determined. Two channels for each camera is a result of the hollow nature of the bolometer emissivty. Plotted in (b), red lines indicate the channels for these six channels. The V3FIT-reconstructed $q = 2$ magnetic flux surface is plotted along with the last closed flux surface (LCF).

Using the bolometer data seen in Fig. 5.9(b), the fluctuations can be analyzed by subtracting the background emission calculated using SVD. The top panel of Fig. 5.10(a) shows the bolometer signal with the SVD background plotted for channel 4 of the midplane bolometer. On the bottom panel, the same fluctuations are normalized to the background by dividing the fluctuations by the background signal. Channel 4 was selected because it possesses the largest normalized fluctuations on the midplane bolometer. Using the inference that the plasma emission is hollow, the two channels viewing either side of the center of the plasma that have the largest normalized fluctuations can be found for each bolometer in our array. The six total channels (two for each bolometer) have their chords plotted in Fig. 5.10(b). These chords, that represent the channels possesing the largest normalized bolometer fluctuations, primarily fall on the V3FIT reconstructed $q = 2$ flux surface which is plotted in Fig. 5.10(b) along with the last closed flux surface (LCF). The bolometer fluctuations oscillate at the same frequency as the MHD activity ($m/n = 2/1$), as determined from magnetic diagnostics in Fig. 5.8, just before the disruption.

Using a De-Convolutional Neural Network (DeCNN) (18) trained for CTH bolometer tomography, the bolometer signals can be inverted to resolve the plasma emission cross-section. Fig. 5.11 shows the inverted bolometer fluctuations along with the poloidal magnetic field fluctuations as determined by the Mirnov coils located twelve degrees toroidally away from the bolometers (see Fig. 5.6 for the poloidal placement of the B-dot coils).

The reconstructed emission fluctuations appear to have two distinct structures, with one being closer to the magnetic axis and one close to the $q = 2$ surface (dashed line). The emissivity fluctuations near the magnetic axis and core plasma have a predominantly $m = 1$ mode structure. The radially outermost fluctuation is significant given is location close to the $q = 2$ surface and its dominant $m = 2$ poloidal structure. We therefore postulate that this $m = 2$ bolometer fluctuation is associated with the rotating $m/n = 2/1$ tearing mode involved in the density limit disruption as measured by the magnetics. Given that the SVD analysis shows that the bolometer and magnetic fluctuations oscillate at the same frequency, we next map the $m = 2$ magnetic fluctuations from the toriodal position they are measured to the location of the bolometric arrays for comparison of the relative phase of the maxima and minima of the two signals. Fig. 5.11 shows that the peak poloidal magnetic fluctuations correlate closely with the peak emission fluctuations as both rotate. Peak poloidal magnetic field fluctuations are associated with the O-points of the magnetic island and hence we conclude that the peak emission as measured by the bolometers comes from the $m/n = 2/1$ island O-points during these density limit disruptions The evidence points to the source of the plasma emission fluctuations being the rotating magnetic island seen in the magnetic diagnostics as a $m = 2$ mode. This result appears to qualitatively agree with the theory of thermo-resistive magnetic islands being the driving mechanism of density limit disruptions in tokamaks (19; 20; 21; 22; 23). An investigation into quantitatively understanding the thermo-resistive magnetic islands theory for CTH is needed to further confirm this conclusion.

In summary, at low vacuum transform, we have found that CTH density limit disruptions behave similarly to tokamak disruptions. The characteristic signs are a positive spike in plasma current and a corresponding dip in loop voltage followed by a collapse of plasma current. Other phenomena include a growth in MHD activity particularly a $m/n = 2/1$ mode that becomes

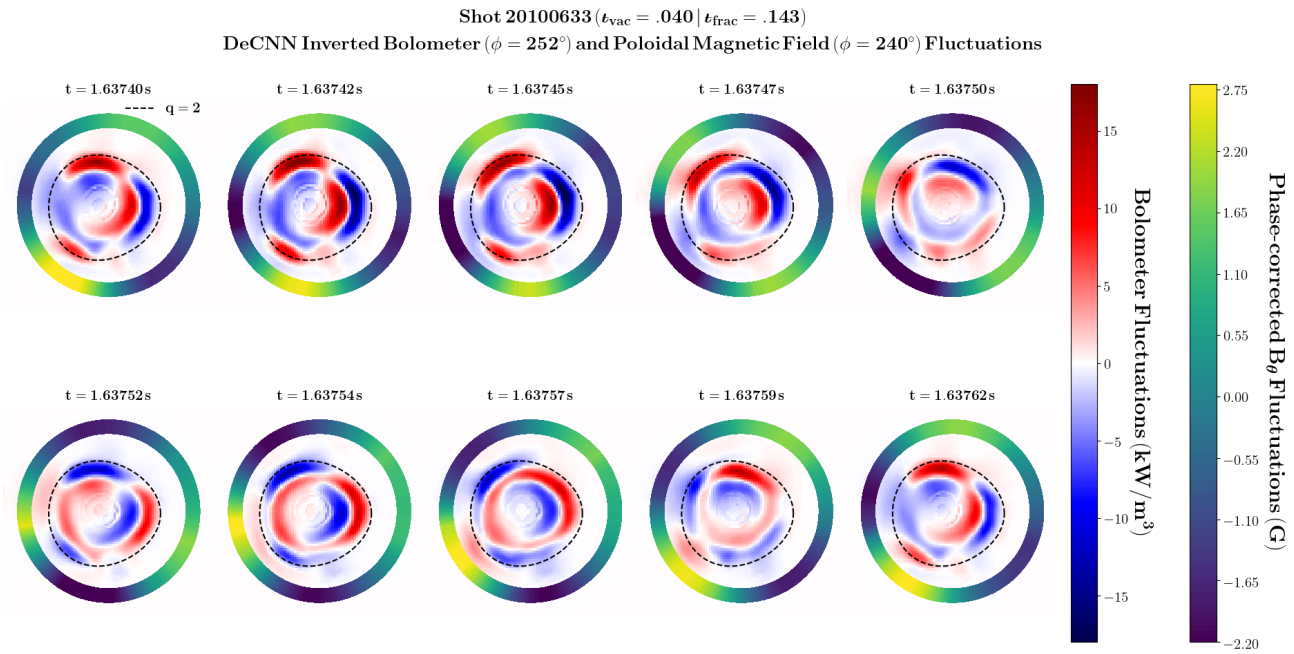

Figure 5.11: A time history of the De-Convolutional Neural Network (DeCNN) inverted bolometer fluctuations is shown with the poloidal magnetic field fluctuations. The bolometers are located at the toroidal angle $\phi = 252°$ and the Mirnov coils at $\phi = 240°$. The magnetic diagnostic consists of 34 Mirnov coils positioned on the inside of CTH's vacuum vessel which has a circular cross-section. The V3FIT reconstructed $q = 2$ flux surface is shown with dashed lines.

strong enough to be seen in the integrated density, SXR, and bolometer signals as indicated by synchronous fluctuation growth and the apparent coupling of principal fluctuation frequencies. Using the bolometers, the spatial location of the strongest fluctuations was determined to lie on the V3FIT-reconstructed, $q = 2$ magnetic flux surface. Inverting the bolometer fluctuations, the peak plasma emission fluctuations were found to correlate with the peaking peak poloidal magnetic field fluctuations as both rotated poloidally. These results indicate that in tokamak-like CTH density limit disruptions, radiating $m/n = 2/1$ magnetic islands grow significantly in strength and radiated emission just before the disruption.

5.4 High Vacuum Rotational Transform CTH Termination

Plasma termination at high vacuum transform differs substantially from that observed at low vacuum rotational transform. A typical high vacuum transform discharge evolution and termination is depicted in Fig. 5.12(a).

The dynamics of the reconstructed q_{edge} and current profile show that the current profile is slowly contracting and peaking in the core due to the plasma current ramp down as is shown in the two lower panels of Fig. 5.12(a). No rapid profile contraction is observed prior to the discharge termination as is seen at low vacuum transform. This slow contraction at high vacuum transform, coupled with the plasma current, loop voltage, and decreasing SXR signals indicates that the plasma is simply cooling down as the density is increased.

Missing are the growing poloidal magnetic field fluctuations, the sinusoidal oscillations seen in the density and central SXR traces, and the large amplitude sawteeth in the central SXR Fig. 5.12(b). The lack of large amplitude sawteeth seen in central SXR channels at high vacuum rotational transform CTH discharges has been previously reported (3). Some high transform plasma terminations still exhibit a small positive current spike as well as a small negative loop voltage dip, but these characteristics are significantly weaker as compared to the low vacuum rotational transform disruptions and do not appear to be driven by rearrangement of the current profile due to large amplitude MHD activity.

While visually seen in Fig. 5.12 to be much smaller than those a low vacuum rotational transform, the magnetic, density, and SXR fluctuations can be analyzed with the same SVD

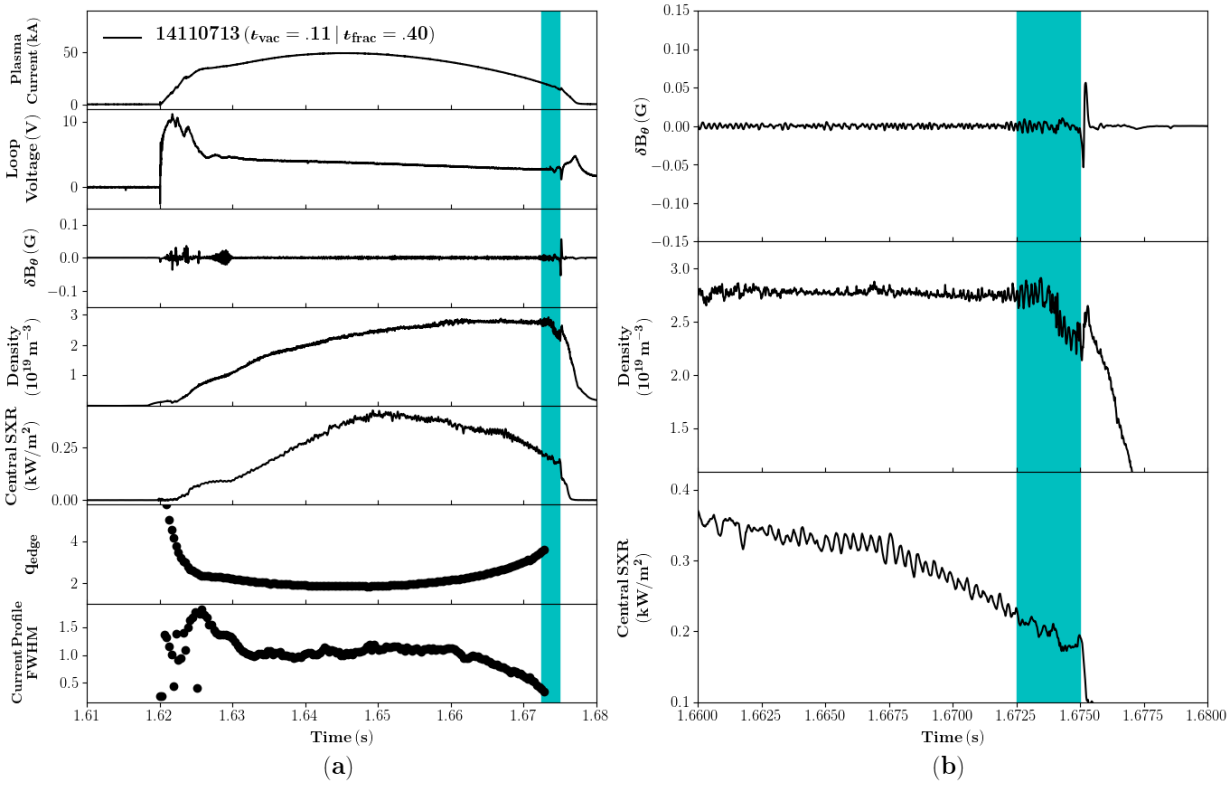

Figure 5.12: CTH disruption having $t_{\text{vac}} = 0.11$ and $t_{\text{frac}} = 0.40$. From top to bottom for (a), are the plasma current I_{p}, the loop voltage, the poloidal magnetic field fluctuations δB_θ, the line-averaged density n_e, the central soft x-ray (SXR) signal, the V3FIT reconstructed q_{edge}, and the V3FIT reconstructed *FWHM* of the current profile. For (b), the magnetic field fluctuations, the density, and the SXR signals are zoomed-in in time to highlight the absence of large fluctuations as compared to Fig. 5.3. The disruption is highlighted in cyan.

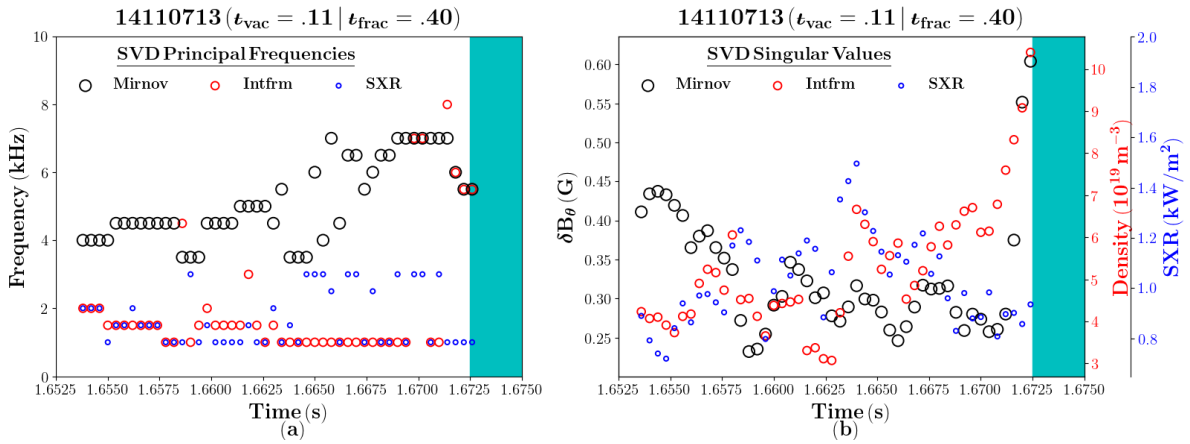

Figure 5.13: The results from the Singular Value Decomposition (SVD) analysis of the magnetic, density, and SXR diagnostics using a moving $2\,ms$ window for shot 14110713 from Fig. 5.12 are shown. For (a), the principal frequencies of the strongest SVD mode for each diagnostic are plotted. For (b), the singular values for the strongest SVD modes are plotted leading up to the disruption. The disruption is highlighted in cyan.

technique used above. The result in Fig. 5.13 shows an absence of matching principal frequencies (Fig. 5.13(a)) and synchronous growth in the SVD mode strength (Fig. 5.13(b)) just before the disruption. The analysis of the bolometer signals for shots at high vacuum rotational transform showed there was no correlation found between the bolometer fluctuations and any flux surface activity, which is not surprising considering the lack of coupling discussed above for high vacuum rotational transform disruptions.

In summary, CTH density related terminations at high vacuum rotational transform differ substantially from those at low vacuum rotational transform. There is no large growth in magnetic activity and no large amplitude SXR sawteeth or core oscillations. A systematic study of the frequency behavior between the poloidal magnetic field fluctuations, the density measurements, and the SXR signals, reveals no evidence of synchronous oscillations due to coupled MHD activity at high vacuum rotation transform. Instead these terminations appear to be linked to the natural plasma current ramp down due to the discharge nearing its end as the loop voltage ramps down. These relatively cold plasmas also have higher ($\sim 50\%$) radiated power fractions as discussed in the next session. These high transform terminations are determined by CTH operational characteristics and limitations as the plasma current is decreasing naturally.

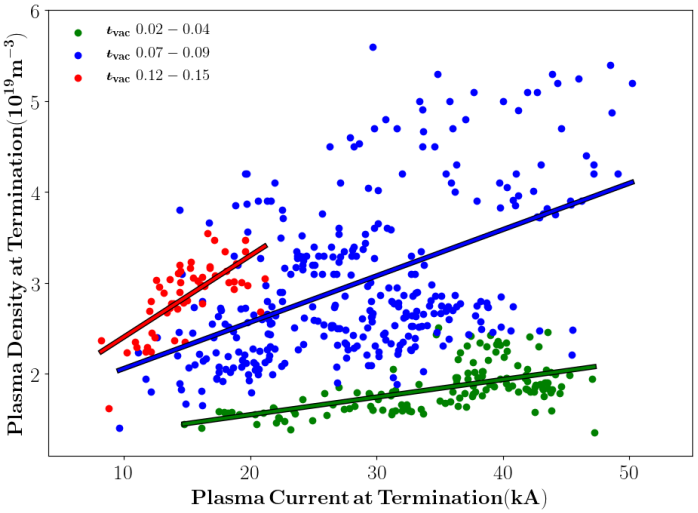

Figure 5.14: Plasma current and density at plasma termination for an ensemble of CTH density limit terminations. Results are binned according to ranges of the vacuum rotational transform ι_{vac}.

5.5 The Effect of Varying Vacuum Rotational Transform

The impact of increasing the level of vacuum transform on CTH density limit terminations is illustrated in Fig. 5.14. The V3FIT-reconstructed densities of terminating hydrogen and deuterium discharges are plotted versus the plasma current immediately prior to termination of each of these discharges. For consistency, the termination is determined as the point in time just before the positive plasma current spike and the negative loop voltage dip. The data in Fig. 5.14 are binned in three ranges of vacuum transform, low vacuum transform ($\iota_{vac} = .02 - .04$), medium vacuum transform ($\iota_{vac} = .07 - .09$), and high vacuum transform ($\iota_{vac} = .12 - .15$).

For CTH, the plasma current in high vacuum transform discharges is typically lower for a given density than in lower vacuum transform plasmas. Nonetheless, the density at termination for a given plasma current (e.g. $I_{\mathrm{p}} = 20\,kA$) increases with higher vacuum transform. As shown in Fig. 5.14, the slopes of lines fit to the three groups of vacuum transform increase as the transform increases.

The termination densities are normalized to the Greenwald density in Eq. 1.3 using the experimental plasma current and plasma minor radius calculated from V3FIT reconstructions and plotted in Fig. 5.15. Because CTH has fully 3D flux surfaces, the minor radius is taken

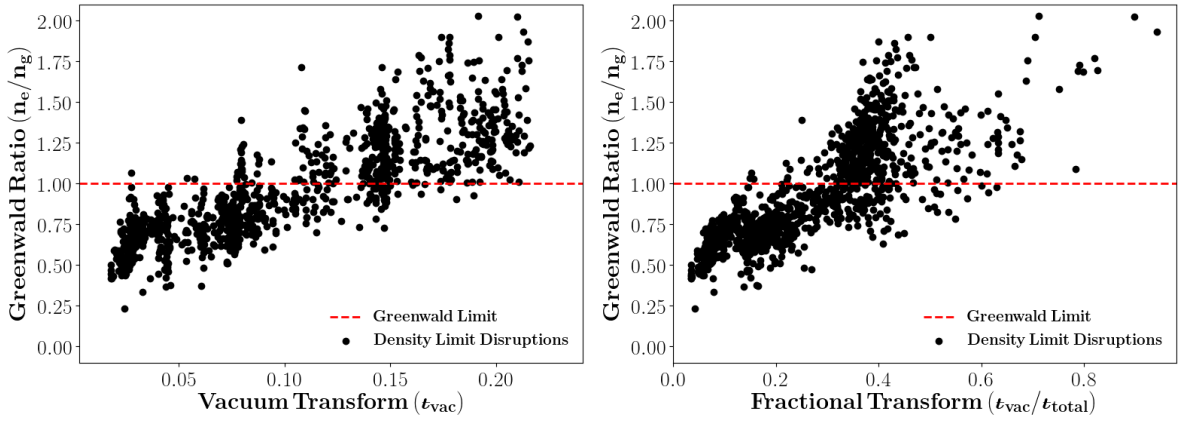

Figure 5.15: Density at termination normalized to the Greenwald density for CTH disrupting discharges is plotted versus the vacuum transform (ι_{vac}) and the fractional transform (ι_{frac}) at the termination.

to be the average minor radius. As the vacuum rotational transform in CTH discharges is increased, the density at termination relative to the Greenwald density is found to increase from a value of 1/2 the empirical limit to levels close to two times the limit. At high levels of vacuum rotational transform ($\iota_{vac} > 0.15$) and fractional rotational transform ($\iota_{frac} > 0.40$), the densities can consistently surpass the Greenwald density limit.

In an attempt to understand how CTH can surpass the Greenwald limit, a subset of the data was analyzed. This subset represents the most recent density limit campaign completed in 2020 using deuterium for all the shots. To try to fit this data with the other density limit scalings from both tokamaks and stellarators, we resorted to the three main density limit scaling described earlier (Greenwald, Hugill, and Sudo limits), the respective ratios for each are plotted in Fig. 5.16. The Hugill scaling factor C_H is set to the most widely accepted value of $C_H = 1.14$ (24) and the q used is the VMEC calculated equilibrium q not the cylindrical q, so this is a modified form of the Hugill limit using the actual MHD q. The Sudo limit scales linearly primarily because the input power for CTH is ohmic (ie. $P_{in} \propto I_P^2$). However, the Hugill ratio stays mostly below unity which is the desired outcome for a density limit scaling. We mean by this that if we were to base our selection of empirical density limit scalings on this plot, we would choose the Hugill limit as it is not systematically surpassed and the density ratio flattens off just underneath unity. However, at low levels of vacuum and fractional rotational

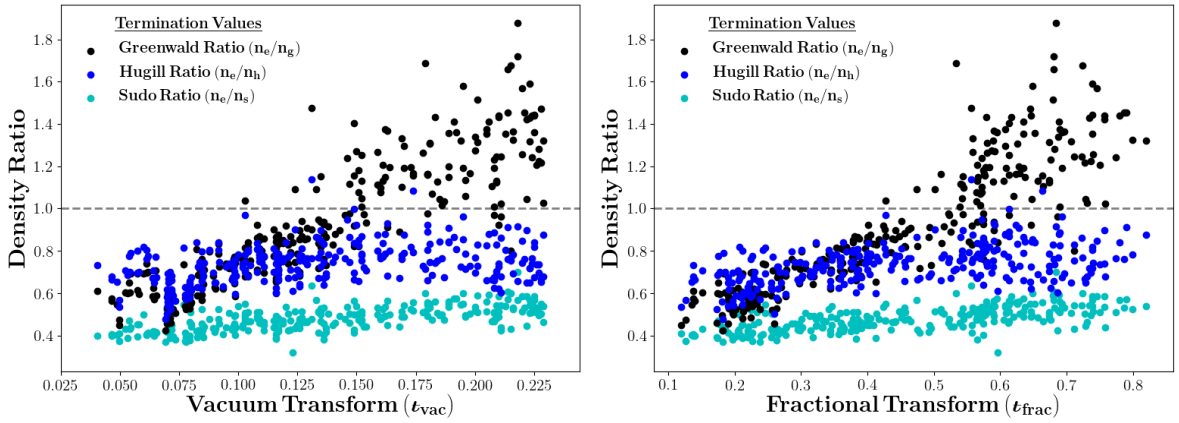

Figure 5.16: Density at disruption normalized to Greenwald density, Hugill density, and Sudo density for CTH disrupting discharges vs. vacuum transform (ι_{vac}) and fractional transform (ι_{frac}) at the disruption.

transform, the values for the Greenwald and Hugill densities are close to each other. They only begin to deviate as the the vacuum rotation transform reaches a value of $\iota_{\text{vac}} = 0.125$ as seen in Fig. 5.16.

An explanation of the similarity of the Hugill and Greenwald limits at low vacuum rotational transform, which is a more tokamak-like regime for CTH, as well as their deviation at high levels of vacuum rotational transform, which is more stellarator-like, can be shown by rewriting the Hugill limit in Eq. 1.2 to have the form:

$$n_{\text{H}} = C_{\text{H}} \frac{B_{\text{T}}}{R_0} (\iota_{\text{plasma}} + \iota_{\text{vac}}) \tag{5.3}$$

using the definition of $q = 1/\iota$ and the total rotational transform from Eq. 3.3. If the cylindrical plasma definition for the rotational transform is used (instead of the fully 3D flux surface averaged one gained from V3FIT reconstructions), Eq. 5.3 can be rewritten as

$$n_{\text{H}} = C_{\text{H}} \left(\frac{B_{\text{T}}}{R_0} \frac{\mu_0 R_0 I_{\text{P}}}{2\pi a^2 B_{\text{T}}} + \frac{\tau_{\text{vac}} B_{\text{T}}}{R_0} \right) = C_{\text{H}} \left(\frac{\mu_0 I_{\text{P}}}{2\pi a^2} + \frac{\tau_{\text{vac}} B_{\text{T}}}{R_0} \right)$$

$$n_{\text{H}} \approx n_{\text{G}} + \frac{\tau_{\text{vac}} B_{\text{T}}}{R_0} \tag{5.4}$$

At low levels of ι_{vac}, CTH is tokamak-like and the Hugill and Greenwald limits qualitatively agree. But, as more ι_{vac} is applied, the second term in Eq. 5.4 becomes more impactful which is evident in CTH as densities surpass the Greenwald limit (Fig. 5.16).

While the above discussion helps to qualitatively explain the results shown in Fig. 5.16, before an empirical scaling can be declared more beneficial for predicting tokamak density limits, a case study must performed for individual shots. Fig. 5.17 shows the the low transform discharge discussed in Sec. 5.3 and a high vacuum rotational transform discharge. Focusing on the third panel down, we see the evolution of the densities in addition to the Greenwald and Hugill densities which are calculated using V3FIT reconstructed values at each time. For both of these shots, the Hugill density is closer to the plasma density than the Greenwald at the time of the termination. For the low vacuum rotational transform termination, the density reaches the calculated Hugill limit before reaching the Greenwald limit. For the high vacuum rotational transform termination, the Greenwald density is surpassed by the plasma densities, but the termination does not occur until the Hugill and plasma densites are almost the same. It is only as the plasma density comes to the Hugill density that the tokamak-like disruption characteristics, namely a plasma current spike and loop voltage dip, appear. Comparing the results of Fig. 5.16 and Fig. 5.17, the Hugill limit, calculated using the V3FIT reconstructed rotational transforms (Eq. 5.3), possesses greater density limit termination prediction ability than the Greenwald limit.

5.6 The Driving Mechanism of Density Limit Terminations at High Vacuum Rotational Transform

While the Hugill limit may be more beneficial in predicting the tokamak-like appearance of the positive plasma current spike and corresponding loop voltage dip at high vacuum rotational transform, the termination of these plasmas is not determined by this phenomena. These plasmas are slowly contracting due to the decreasing plasma current and only happen to exhibit the tokamak-like disruption characteristics of a loop voltage dip and plasma current spike during their collapse.

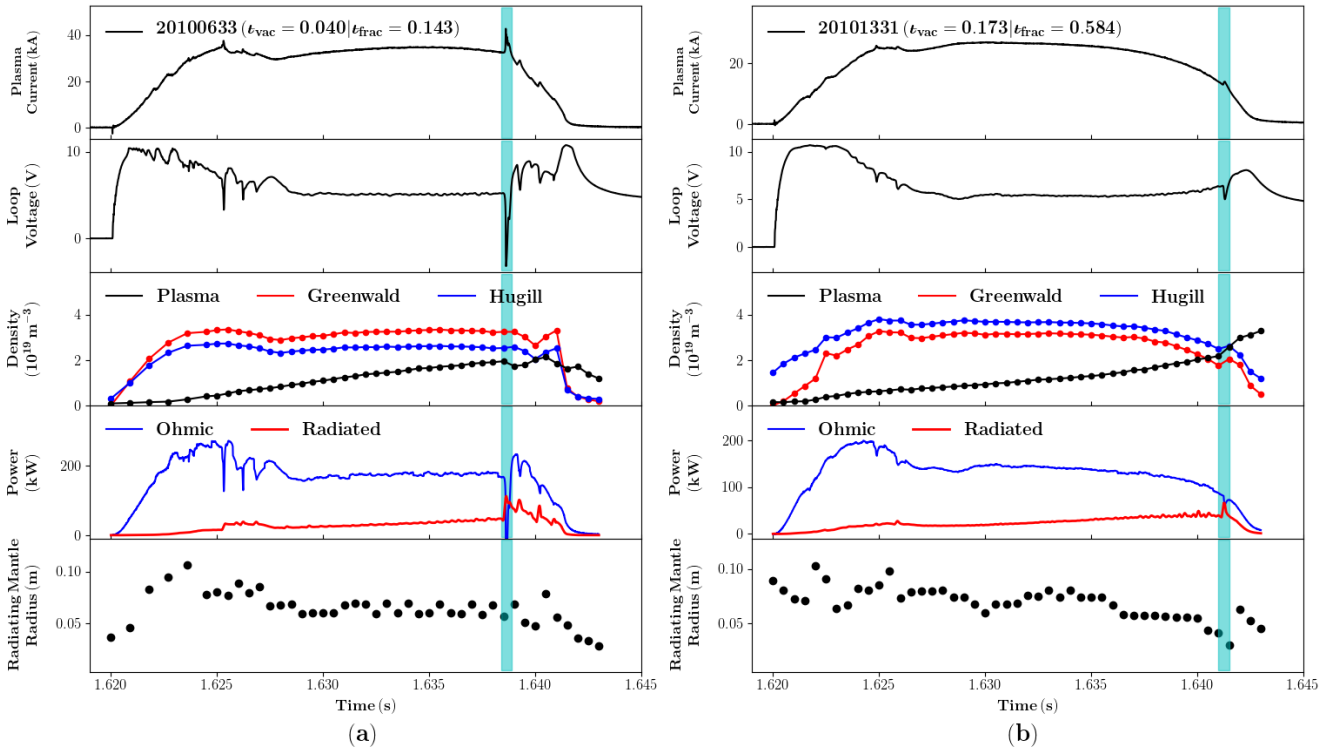

Figure 5.17: Shots 20100633 and 20101331 are plotted showing the plasma current, the loop voltage, and the plasma density. The density with the corrected path length, the calculated Greenwald density, and the calculated Hugill density are also plotted.The bottom two panels contain the total input and output powers (ohmic and radiated) as well as the radial position of the peak bolometer emission location.

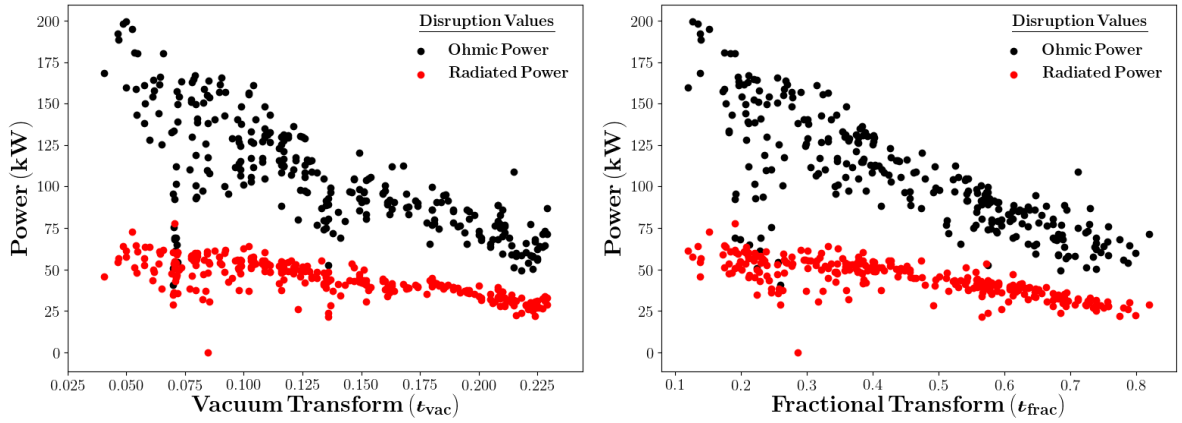

Figure 5.18: The radiated power at the disruption, calculated from the bolometer signals using an Abel inversion, as well as the ohmic input power, taking into consideration the inductive contributions of the changing plasma current, are plotted versus vacuum and fractional rotational transform.

To understand the driving mechanism of the slow plasma collapse, we start by investigating the effects of radiation on the plasma. This study is motivated by the global power balance of input power and radiated power known to impact the density performance on pure stellarators. Returning to Fig. 5.17, the second from the bottom panel shows the ohmic input power and the total radiated power. The total radiated power is calculated by inverting the absolutely calibrated bolometers (see Appx. B) using a magnetic flux surface inversion producing a poloidal slice of plasma emission. Under the assumption that the radiation is toroidally symmetric, the total radiated power can be found. The input power is ohmic and can be calculated using the evolving values of the measured loop voltage and plasma current and the V3FIT reconstructed inductance (see Eq. 2.1.11 in (25)). From Fig. 5.17, we find that the radiation may be a contributing factor in the slow contraction of the plasma at high vacuum transform.

To consider an ensemble study of power balance, Fig. 5.18 shows the ohmic input power, taking into consideration inductive effects, and the total radiated power which is calculated from the DeCNN inverted bolometer signals. While there is more scatter at low vacuum rotational transform, we find that the radiated power becomes more significant at high vacuum rotational transform. However, it does not surpass the input power for any of the terminations. This result

is distinct from typical stellarators where the radiated power can eclipse the input power as the density is ramped up.

In general, we find that plasma terminations at high vacuum rotational transform are different that those at low vacuum rotational transform. The plasmas are found to be smaller in size as the vacuum rotational transform is increased. These plasmas also contract as the density is increased and the plasma current decreases, which causes the current profile naturally to peak. This contraction of the plasma, coupled with the decreased total plasma currents, at high vacuum rotational transform is most likely caused by an increased resistivity of the plasma as more particles are toroidally trapped due to the magnetic configuration become more stellarator-like.

5.7 Empirical Definition of the Transition from Tokamak-like Disruptions to Weak Terminations

Density limit plasma terminations on CTH at low levels of vacuum and fractional rotational transforms exhibit many tokamak-like characteristics. As the vacuum rotational transform (and fractional rotational transform) is increased, the tokamak-like characteristics fade away completely except for a plasma current spike and loop voltage dip which considerably lessen in intensity. The plasma terminations at high vacuum rotational transform, which behave as slowly contracting plasmas, are fundamentally different than those at low vacuum rotational transform, which exhibit the strong plasma disruption characteristics found in tokamaks.

To quantitatively distinguish the two extremes, we attempt to define what is a true disruption on CTH based on its corresponding poloidal magnetic field fluctuations which correlate to MHD activity on multiple diagnostics. Fig. 5.19 shows the poloidal magnetic field fluctuations at the time of peak plasma current and just before the termination. The values are taken from an average over a $2\,ms$ window. Based on the magnetic fluctuations at the terminations shown in Fig. 5.19, the cutoff point that distinguishes the disruptions from the weak plasma terminations was set to $0.3\,G$. A possible explanation of the weakened strength of the poloidal magnetic field fluctuations at the termination for high vacuum transform discharges is that, as the plasma is contracting, the source of the magnetic fluctuations in the plasma becomes physically farther away from the magnetic diagnostics resulting in weaker diagnostics signals. Discharges with

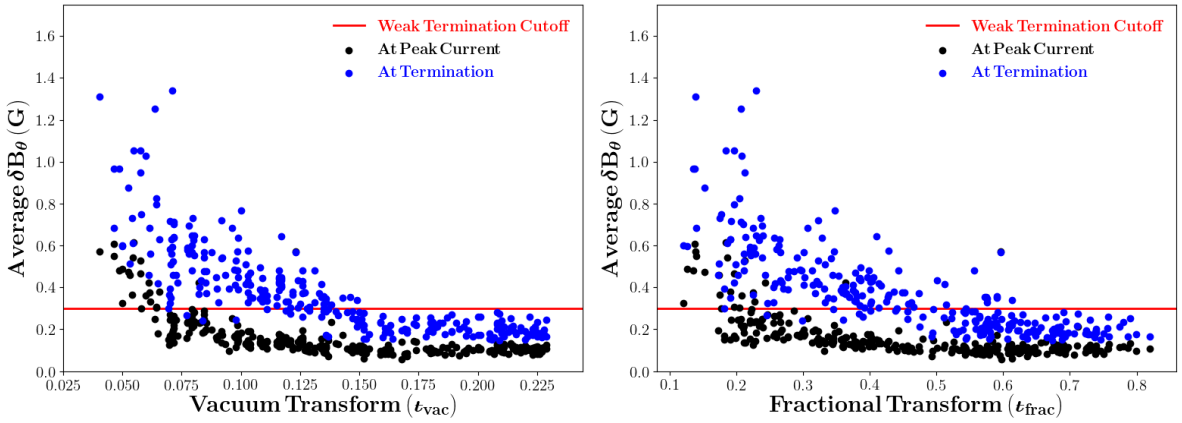

Figure 5.19: The poloidal magnetic field fluctuations, averaged over a $2\,ms$ window, at the time of peak plasma current and just before the termination are plotted versus vacuum and fractional rotational transform. The red line represents the cutoff value ($0.3\,G$) used to distinguish the disruptions from the weak terminations.

poloidal magnetic field fluctuations just before the termination that are weaker than the cutoff value are classified as weak plasma terminations.

To understand the relevance of this definition on the previously shown work, Fig. 5.16 can be replotted to show the demarcation between weak terminations and actual tokamak-like disruptions. Fig. 5.20 shows the replotted Greenwald and Hugill density ratios. Observing the Greenwald ratios, the cutoff appears on average just as the Greenwald ratio hits unity which also corresponds to a fractional rotational transform value of $\iota_{\text{frac}} = 0.5$. For the Hugill ratios, the cutoff mostly appears where the Hugill and Greenwald ratios start to differ significantly. The empirical definition of a disruption on CTH, as based on poloidal magnetic field fluctuations, could possibly indicate the point at which CTH operationally switches from a tokamak-like discharge with significant 3D magnetic fields to a current carrying, stellarator-like discharge.

In review, an empirical definition of CTH disruptions based on poloidal magnetic field fluctuations demonstrates some interesting correlations with the density limit scalings. However, it is greatly limited in that it cannot provide a physics definition of a disruption and could be greatly influenced by other phenomena. As the vacuum rotational transform is raised, the reconstructed last closed flux surface (LCF) shrinks in size meaning that any poloidal magnetic field activity located near or close the LCF on average becomes physically farther away

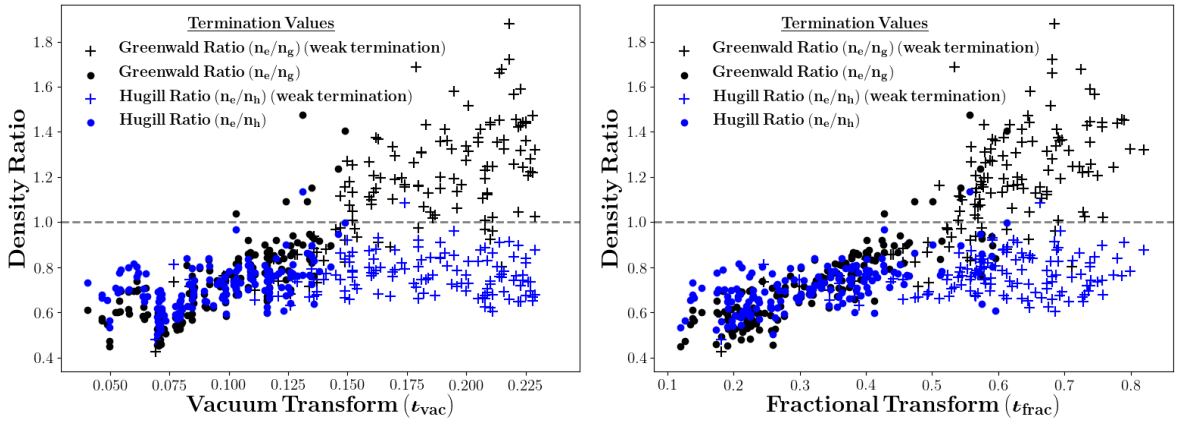

Figure 5.20: The replotting of Fig. 5.16 that distinguishes the weak terminations from the disruptions.

from the magnetic probes producing a weaker signal. Also, with the changing externally applied rotational transform profile, the magnetic surface on which the poloidal magnetic field activity originates may be pushed closer to the core resulting in weaker detected fluctuations. Further investigation is required to determine the significance of these phenomena on the CTH disruptions and its definition.

5.8 Discussion and Future Work

Because the existence of density limits in toroidally confined plasmas has significant impacts on fusion programs around the world, extensive understanding of the physics behind the Greenwald density limit is of great importance. We have shown that the density-limiting behavior of CTH plasmas is qualitatively similar to that seen in tokamaks at low vacuum rotational transform, and is consistent with the classic final scenario of the density limit: current profile shrinkage leads to growing MHD instabilities (usually $m/n = 2/1$ tearing mode) followed by loss of MHD equilibrium, and final disruptions. The affects of the growing MHD mode were evident across multiple diagnostics with the bolometers fluctuations pointing to a spatial origination on the $q = 2$ flux surface. Inverting the bolometer fluctuations, the peak plasma emission fluctuations were found to correlate with the peaking peak poloidal magnetic field fluctuations as both rotated poloidally. These results indicate that in tokamak-like CTH density limit disruptions,

radiating $m/n = 2/1$ magnetic islands grow significantly in strength and radiated emission just before the disruption.

The hybrid plasmas of CTH also show a unique feature that increasing the external rotational or vacuum transform leads to stable operation at densities above the Greenwald limit. However, discharges at these magnetic field configurations show a slow plasma collapse which is similar to that seen in a traditional stellarator. In general, we find that while terminations at high vacuum rotational transform are different that those at low vacuum rotational transform, this difference is not driven by a radiative collapse. But the plasmas are still found to be smaller in size as the vacuum rotational transform is increased. This shrinkage of the plasma, coupled with the decreased plasma currents, at high vacuum rotational transform is most likely caused by an increased resistivity of the plasma as more particles are toroidally trapped due to the magnetic configuration become more stellarator-like. Based on the poloidal magnetic field fluctuations, an empirical definition that distinguishes a CTH disruption from a weak plasma termination has been established.

The physics underlying the tokamak-like density limit in CTH plasmas may be ascribed to a radiative instability localized to a specific rational surface. The best predictor of the tokamak-like density limit characteristics across all ranges of vacuum rotational transform was found to be the Hugill density limit not the Greenwald limit. Of important significance, at increasing levels of vacuum rotational transform, the performance of the CTH plasmas (ie. the slow collapse) is not dictated by either Greenwald or Hugill limits but seems to be caused by increased plasma resistivity possibly due to toroidally trapped particles.

While the available range of CTH diagnostics did provide insight into the growing MHD activity at low levels of vacuum rotational transform, in that frequency coupling was observed just before the disruption, future bolometer/two-color soft x-ray (SXR) installations could provide better spatial and plasma temperature information to be used with existing inversion techniques in order to flesh out the spatial dynamics seen in the plasma. The goal of such an implementation would be to observe the radiation produced by any island structure located at the $q = 2$ flux surface. This bolometer and SXR data, coupled with data reconstruction software that is capable of solving the plasma equilibrium with magnetic islands present (such as

SIESTA (26; 27)) would provide the best possible analysis of the MHD activity driving the tokamak-like density limit. In addition, a study of the increased levels of plasma resistivity at high levels of vacuum rotational transform who be of great benefit to future hybrid devices.

References

[1] M. D. Pandya, M. C. ArchMiller, M. R. Cianciosa, D. A. Ennis, J. D. Hanson, G. J. Hartwell, J. D. Hebert, J. L. Herfindal, S. F. Knowlton, X. Ma, S. Massidda, D. A. Maurer, N. A. Roberds, and P. J. Traverso, "Low edge safety factor operation and passive disruption avoidance in current carrying plasmas by the addition of stellarator rotational transform," *Physics of Plasmas*, vol. 22, no. 11, p. 110702, 2015.

[2] N. A. Roberds, L. Guazzotto, J. D. Hanson, J. L. Herfindal, E. C. Howell, D. A. Maurer, and C. R. Sovinec, "Simulations of sawtoothing in a current carrying stellarator," *Physics of Plasmas*, vol. 23, no. 9, 2016.

[3] J. L. Herfindal, D. A. Maurer, G. J. Hartwell, D. A. Ennis, J. D. Hanson, S. F. Knowlton, X. Ma, M. D. Pandya, N. A. Roberds, P. J. Traverso, and et al., "Sawtooth oscillation behavior with varying amounts of applied stellarator rotational transform," *Physics of Plasmas*, vol. 26, no. 3, 2019.

[4] M. C. ArchMiller, M. R. Cianciosa, D. A. Ennis, J. D. Hanson, G. J. Hartwell, J. D. Hebert, J. L. Herfindal, S. F. Knowlton, X. Ma, D. A. Maurer, M. D. Pandya, and P. Traverso, "Suppression of vertical instability in elongated current-carrying plasmas by applying stellarator rotational transform," *Physics of Plasmas*, vol. 21, no. 5, p. 056113, 2014.

[5] J. D. Hanson, S. F. Knowlton, B. A. Stevenson, and G. J. Hartwell, "Equilibrium and stability of current-carrying discharges in the non-axisymmetric cth experiment," *Contributions to Plasma Physics*, vol. 50, no. 8, pp. 724–730, 2010.

[6] J. Hanson, D. Anderson, M. Cianciosa, P. Franz, J. Harris, G. Hartwell, S. Hirshman, S. Knowlton, L. Lao, E. Lazarus, L. Marrelli, D. Maurer, J. Schmitt, A. Sontag, B. Stevenson, and D. Terranova, "Non-axisymmetric equilibrium reconstruction for stellarators, reversed field pinches and tokamaks," *Nuclear Fusion*, vol. 53, no. 8, p. 083016, 2013.

[7] X. Ma, D. A. Maurer, S. F. Knowlton, M. C. ArchMiller, M. R. Cianciosa, D. A. Ennis, J. D. Hanson, G. J. Hartwell, J. D. Hebert, J. L. Herfindal, M. D. Pandya, N. A. Roberds, and P. J. Traverso, "Non-axisymmetric equilibrium reconstruction of a current-carrying stellarator using external magnetic and soft x-ray inversion radius measurements," *Physics of Plasmas*, vol. 22, no. 12, 2015.

[8] X. Ma, M. R. Cianciosa, D. A. Ennis, J. D. Hanson, G. J. Hartwell, J. L. Herfindal, E. C. Howell, S. F. Knowlton, D. A. Maurer, P. J. Traverso, and et al., "Determination of current and rotational transform profiles in a current-carrying stellarator using soft x-ray emissivity measurements," *Physics of Plasmas*, vol. 25, no. 1, p. 012516, 2018.

[9] T. Dudok de Wit, A. Pecquet, J. Vallet, and R. Lima, "The biorthogonal decomposition as a tool for investigating fluctuations in plasmas," *Physics of Plasmas*, vol. 1, no. 10, pp. 3288–3300, 1994.

[10] T. D. de Witt, "Enhancement of multichannel data in plasma physics by biorthogonal decomposition," *Plasma Physics and Controlled Fusion*, vol. 37, no. 2, p. 117, 1995.

[11] D. A. Maurer, D. Shiraki, J. P. Levesque, J. Bialek, S. Angelini, P. Byrne, B. DeBono, P. Hughes, M. E. Mauel, G. A. Navratil, Q. Peng, D. Rhodes, N. Rath, and C. Stoafer, "High resolution detection and excitation of resonant magnetic perturbations in a wall-stabilized tokamak," *Physics of Plasmas*, vol. 19, no. 5, p. 056123, 2012.

[12] C. Nardone, "Multichannel fluctuation data analysis by the singular value decomposition method. Application to MHD modes in JET," *Plasma Physics and Controlled Fusion*, vol. 34, no. 9, p. 1447, 1992.

[13] J. S. Kim, D. H. Edgell, J. M. Greene, E. J. Strait, and M. S. Chance, "MHD mode identification of tokamak plasmas from Mirnov signals," *Plasma Physics and Controlled Fusion*, vol. 41, no. 11, p. 1399, 1999.

[14] D. Raju, R. Jha, P. Kaw, S. K. Mattoo, Y. Saxena, and A. team, "Mirnov coil data analysis for tokamak ADITYA," *Pramana - journal of physics*, vol. 55, no. 5, pp. 727–732, 2000.

[15] M. J. Hole and L. C. Appel, "Fourier decomposition of magnetic perturbations in toroidal plasmas using singular value decomposition," *Plasma Physics and Controlled Fusion*, vol. 49, no. 12, p. 1971, 2007.

[16] W. H. Press, S. A. Tukolsky, W. T. Vetterling, and B. P. Flannery, *Numerical Recipes in C: The Art of Scientific Computing*. Cambridge University Press, 2nd ed., 1992.

[17] N. Aubry, F. Carbone, R. Lima, and S. Slimani, "Wave propagation phenomena from a spatiotemporal viewpoint: Resonances and bifurcations," *Journal of Statistical Physics*, vol. 76, 08 1994.

[18] D. R. Ferreira, P. J. Carvalho, and H. Fernandes, "Deep learning for plasma tomography and disruption prediction from bolometer data," *IEEE Transactions on Plasma Science*, vol. 48, no. 1, pp. 36–45, 2020.

[19] D. A. Gates and L. Delgado-Aparicio, "Origin of tokamak density limit scalings," *Phys. Rev. Lett.*, vol. 108, no. 16, p. 165004, 2012.

[20] D. Gates, L. Delgado-Aparicio, and R. White, "Physics of radiation-driven islands near the tokamak density limit," *Nuclear Fusion*, vol. 53, no. 6, p. 063008, 2013.

[21] R. B. White, D. A. Gates, and D. P. Brennan, "Thermal island destabilization and the greenwald limit," *Physics of Plasmas*, vol. 22, no. 2, p. 022514, 2015.

[22] D. A. Gates, D. P. Brennan, L. Delgado-Aparicio, Q. Teng, and R. B. White, "Thermo-resistive disruptions and the tokamak density limit," *Physics of Plasmas*, vol. 23, no. 5, p. 056113, 2016.

[23] Q. Teng, D. Brennan, L. Delgado-Aparicio, D. Gates, J. Swerdlow, and R. White, "A predictive model for the tokamak density limit," *Nuclear Fusion*, vol. 56, no. 10, p. 106001, 2016.

[24] K. Borrass, R. Schneider, and R. Farengo, "A scrape-off layer based model for hugill-greenwald type density limits," *Nuclear Fusion*, vol. 37, pp. 523–537, apr 1997.

[25] I. H. Hutchinson, *Principles of plasma diagnostics*. Cambridge, 2002.

[26] M. Cianciosa, S. P. Hirshman, S. K. Seal, and M. W. Shafer, "3d equilibrium reconstruction with islands," *Plasma Physics and Controlled Fusion*, vol. 60, p. 044017, mar 2018.

[27] H. Peraza-Rodriguez, J. M. Reynolds-Barredo, R. Sanchez, J. Geiger, V. Tribaldos, S. P. Hirshman, and M. Cianciosa, "Extension of the siesta mhd equilibrium code to free-plasma-boundary problems," *Physics of Plasmas*, vol. 24, no. 8, p. 082516, 2017.

Chapter 6

Summary and Future Work

6.1 Summary

While the majority of the work described in this thesis revolves around CTH and density limit disruptions, a wavelength calibration system for x-ray imaging crystal spectrometers using direct illumination of the spherical diffracting crystal has been developed, tested, and designed for XICS on W7-X. This system will provide a wavelength calibration across the whole detector with very high accuracy (limited mainly by integration time), but with a single remaining systematic offset. The random error in the measurement is estimated to be 3×10^{-7} Å (50 m/s) with a systematic error of 1×10^{-5} Å (1 km/s). This greatly improves the ability to measure perpendicular flow profiles to high accuracy, and will allow, for the first time on W7-X, parallel flow velocities to be simultaneously measured up to the larger systematic accuracy. Future improvements of the systematic accuracy are expected from future planned improvements in determination of the absolute location of the x-ray source and cross calibration with other diagnostics. In conjunction with the new calibration system, XICSRT, a x-ray ray tracing code in Python, has been developed and released to the public. XICSRT has already been used for development and enhancement of XICS systems for ITER, NIF, and W7-X.

To further the study of CTH density limit disruptions, bolometers were serendipitously installed on CTH. A De-Convolution Neural Network (DeCNN) based inversion method has been developed for the new bolometer arrays to capitalize on the available spatial information. This DeCNN, while structurally similar to DeCNNs developed elsewhere, is fundamentally different

because of the absence of a preexisting bolometer emissivity reconstructions. Without preexisting high quality bolometer inversions available, the DeCNN was trained using synthetic data. With a goal of domain randomization, synthetic data was developed that produced a trained DeCNN that was well generalized and produced better results on real bolometer data than a magnetic flux surface inversion. In addition, a custom loss function was introduced that produced a better trained DeCNN than one that used the built-in loss function. This new DeCNN approach allows for quicker bolometer inversions and the ability to study the fluctuations seen in the bolometer data. The fluctuation pattern rotates in the positive poloidal angle direction with a frequency of approximately $5kHz$. Using the DeCNN inversion, the total radiated power can be calculated quickly and was found to be in good agreement with previous methods.

Because the existence of density limits in toroidally confined plasmas has significant impacts on fusion programs around the world, extensive understanding of the physics behind the Greenwald limit, in particular, is of great importance. This thesis has shown that the density-limiting behavior of CTH plasmas is qualitatively similar to that seen in tokamaks at low vacuum rotational transform, and is consistent with the classic final scenario of the density limit: current profile shrinkage leads to growing MHD instabilities (usually $m/n = 2/1$ tearing mode) followed by loss of MHD equilibrium, and final disruptions. The affects of the growing MHD mode were evident across multiple diagnostics with the bolometers fluctuations pointing to a spatial origination on the $q = 2$ flux surface. The hybrid plasmas of CTH also show a unique feature that increased external rotational or vacuum transform leads to stable operation at densities above the Greenwald limit. However, discharges at these magnetic field configurations show a slow plasma collapse which is similar to that seen in a traditional stellarator.

The physics underlying the tokamak-like density limit in CTH plasmas may be ascribed to a radiative instability localized to a specific rational surface. The best predictor of the tokamak-like density limit characteristics across all ranges of vacuum rotational transform was found to be Hugill density limit not the Greenwald limit. Of important significance, at increasing levels of vacuum rotational transform, the performance of the plasma (ie. the slow collapse) is not dictated by either Greenwald or Hugill limits but seems to be caused by increased plasma resistivity possibly due to toroidally trapped particles.

6.2 Future Work

In the future, without the long computational times, the DeCNN based total radiated power could be used as a runday diagnostic for CTH operators and coordinators. Seeing a ring of emissivity in the background bolometer inversion, it might be possible extract contours of constant bolometer emissivity to use as a proxy for magnetic flux surfaces to invert the interferometer (1) density measurements to get a plasma density profile.

A DeCNN meant for SXR inversions could also be trained using synthetic data that allowed peak profiles. In addition, a Tikhonov regularization using various functionals, such as the Minimum Fisher Information, could be developed to provide a higher quality check of the DeCNN inversions. Also, because domain randomization of synthetic data has been linked to model-based Bayesian formalism, the developement of a Bayesian inversion method, with or without a model basis, would further illustrate the potential of the synthetically-trained DeCNN inversion method.

The inclusion of additional bolometer arrays, such as a six bolometer (each with 20 channels) array setup to be poloidally symmetric and at a different toroidal location than the existing array, with its subsequently trained DeCNN inversion, would allow both an even more accurate total radiated power estimate and an opportunity to track bolometer emission moving toroidally across the plasma. This additional bolometer information could be coupled with magnetic diagnostics using a Siesta-based V3FIT (2; 3) reconstruction to attempt to map magnetic islands with bolometer emission which would provide the best possible analysis of the MHD activity driving the tokamak-like density limit. In addition, a study of the increased levels of plasma resistivity at high levels of vacuum rotational transform who be of great benefit to future hybrid devices.

References

[1] M. C. Miller, J. D. Hanson, G. J. Hartwell, S. F. Knowlton, D. A. Maurer, and B. A. Stevenson, “Design and implementation of a multichannel millimeter wave interferometer

for the compact toroidal hybrid experiment," *Review of Scientific Instruments*, vol. 83, no. 10, pp. –, 2012.

[2] M. Cianciosa, S. P. Hirshman, S. K. Seal, and M. W. Shafer, "3d equilibrium reconstruction with islands," *Plasma Physics and Controlled Fusion*, vol. 60, p. 044017, mar 2018.

[3] H. Peraza-Rodriguez, J. M. Reynolds-Barredo, R. Sanchez, J. Geiger, V. Tribaldos, S. P. Hirshman, and M. Cianciosa, "Extension of the siesta mhd equilibrium code to free-plasma-boundary problems," *Physics of Plasmas*, vol. 24, no. 8, p. 082516, 2017.

Appendices

Appendix A

Overview of Python Scripts Written for CTH Data Access and Analysis

This appendix describes the codes that I wrote to analyze, grab, or filter the data presented in this thesis. With multiple individuals already using and modifying these scripts for their own work, this appendix serves as a short reference and introduction to what has already been developed for CTH in the Python programming language. All scripts were written using Python 3.6. The codes are located on CTH group's hard drive known as 'bonnie' under one of the following directories:

1. /Python/
2. /Python/recon/
3. /_Users/Kring/python/

The programs were written using Python 3.6 but have shown good compatibility with more recent versions. Anaconda is the recommended distribution of Python. It provides an easy packaging system using the *conda* environment with a large list of widely used libraries. In addition, most external packages can easily be installed using the *conda install* method using the Anaconda Prompt.

A.1 CTH Data Access and Processing Scripts

For CTH Data access, MDS+ must be installed on the computer as well as for Python. If the Python scripts do not work, try making a local copy of the MDS+ Python files and directly

import them into the scripts. Most issues with MDS+ can be resolved if the computer is using the most recent version of MDS+.

cthdata.py Class(es): **CTHData**. Generic class to access the CTH MDS+ tree.

cthsxr.py Class(es): **Bolometer, SXR_TN**. Grabs and calibrates the bolometer and SXR data for a given shot. Includes contour plotting routines. Uses: **CTHData**.

cthmagnetics.py Class(es): **Mirnov240Data, ToroidalData**. Grabs and calibrates the B-dot probes in the poloidal array at $\phi = 240$ as well as the toroidal array. Includes contour plotting routines. Uses: **CTHData**.

magnetic_shift.py Class(es): **MagneticAxisVerticalShift**. Class that calls specific cube coils to get an estimate of the vertical shift of the plasma. Uses: **CTHData**.

A.2 V3FIT Reconstruction Scripts

These scripts were intended to be used on a reconstruction server such as Recon2 or Recon3. In principle, they can be used for a local installation of V3FIT.

v3data.py Class(es): **V3Data**. Class is modeled off previous Labview programs to grab the data needed for V3FIT reconstructions. Uses: **CTHData**.

recon_input.py Class(es): **InputClass**. Class is the workhorse for grabbing data and parsing it into V3FIT friendly input files. The reconstruction, and subquent reconstructions if multiple times are being reconstructed, can run through class. It Can be used directly or with the commandline interfaces **recon_runner.py** and **full_shot_runner.py**. Uses: **V3Data**.

recon_runner.py Class(es): None. Interface for running V3FIT reconstruction for a single shot at set time(s) from the command line on Recon2 or Recon3. Multiple requirements for use including MDS+ and V3FIT. **intall_steps.txt** is the recommended installation procedure for use. Uses: **InputClass**.

full_shot_runner.py Class(es): None. Interface for running V3FIT reconstruction for the full shot with starting/stopping times and number of reconstructions given from the command line on Recon2 or Recon3. Multiple requirements for use including MDS+ and V3FIT. **intall_steps.txt** is the recommended installation procedure for use. Uses: **InputClass**.

vmec.py Class(es): **wout_file**. Class to read the VMEC and V3FIT produced *wout* files. Included functions can give the magnetic flux surface coordinates in machine coordinates (**R,Z,**ϕ).

result_file.py Class(es): **result_file**. Class to read the *result* files produced with V3FIT.

A.3 Bolometer Specific Scripts

Machine learning specific scripts require a Python environment with Tensorflow installed. Using Anaconda as recommended above, a environment can be created for Tensorflow usage with CPU using the following commands in the Anaconda Prompt:

```
> conda create -n tf tensorflow
> conda activate tf
```

which creates a **tf** conda environment. To access, the environment must be activated which allow subsequently run scripts to use this custom environment. A similar method can be used for GPU ready Tensorflow:

```
> conda create -n tf-gpu tensorflow-gpu
> conda activate tf-gpu
```

In general, I recommend all training be done via GPU, but usage of a trained machine learning model is easily done with a CPU.

cthsxr.py Class(es): **Bolometer, SXR_TN**. Grabs and calibrates the bolometer and SXR data for a given shot. Includes contour plotting routines. Uses: **CTHData**.

flux_surface_grid_inv_direct.py Class(es): **FluxSurfaceGrid**. Generic class to handle inverted bolometer signals including. plotting. Depending on the size of the inversion

grid, the class can generate the projection matrix for any defined line of sight. Can be used with or without a V3FIT reconstructed wout file.

direct_inversion.py Class(es): **ConstrainedTransform**. This class can perform a magnetic flux surface inversion when provided with a wout file from a V3FIT reconstruction.

pathlength.py Class(es): **Pathlength2D**. Class called by **ConstrainedTransform** and **FluxSurfaceGrid** to handle intersections of lines of sight with inverted plasma emission grids or reconstructed magnetic flux surfaces.

cth_bolometer_inversion.py Class(es): **CTHBolometerInversion**. This class uses **ConstrainedTransform** and **FluxSurfaceGrid** to perform an SVD based direct inversion of the bolometer signals. Process needs considerable refinement.

ml_generate_data.py Class(es): None. Script to generate data for DeCNN training. The parameter randomization can be modified easily to switch between hollow and peaked emission profiles with hotspots. Uses: **FluxSurfaceGrid**.

adam_custom_loss.py Class(es): None. Script to define and train a De-Convolutional Neural Network (DeCNN) using a CPU. Script requires a slight modification for GPU training. Script must be used in a Python environment where tensorflow has been installed.

keras_custom_loss.py Class(es): **CustomLoss**. Class to be used for trained DeCNN models that have an architecture with custom loss function as described in Chap. 4. Script must be used in a Python environment where tensorflow has been installed. Uses: **CustomLoss**.

cth_decnn.py Class(es): **DeCNN**. Class to use a trained DeCNN model with real data. Script must be used in a Python environment where tensorflow has been installed. Uses: **CustomLoss**.

decnn_runner.py Class(es): None. Script to be used from the command line to use the DeCNN on real bolometer or SXR data. Script must be used in a Python environment where tensorflow has been installed. Uses: **DeCNN**.

A.4 Data Analysis Scripts

For convenience, most of the routines used for analysis (such as SVD, data smoothing or filtering, FFT, etc.) can be found in the following scripts. The correct way to uses these functions is to import the proper class and then call the needed function. An example is as follows:

```
from general_analysis import Analysis
an = Analysis()
x = np.linspace(0,1,100)
value_to_find = .6
value_index = an.find_closest_index(x, value_to_find)
```

general_analysis.py Class(es): **Analysis**. Class serves to simply call custom analysis functions. Examples include: Singular Value Decomposition (SVD), Fast Fourier Transform (FFT), Hilbert Transform, plotting the vacuum vessel of CTH for bolometer inversions, disruption analysis using SVD, interpolation been bolometer viewing chords, custom profiles for plotting, Butterworth filter, conversion of a string containing an array to an actual array, etc. Uses: **Pathlength2D, FluxSurfaceGrid**.

video_analysis.py Class(es): **VideoAnalysis**. Class that can before video related data analysis including converting a Numpy array from inverted CTH bolometer data into a video. Also includes the capability to study contours in images or videos.

A.5 Python Plotting

I have found through much trial and error that high quality plots can be made in Python using complicated scripting. For Fig. A.1, the Python script is below. This working example with data can be found at

/Python/plotting/kring_example_plot/kring_example_plot.py.

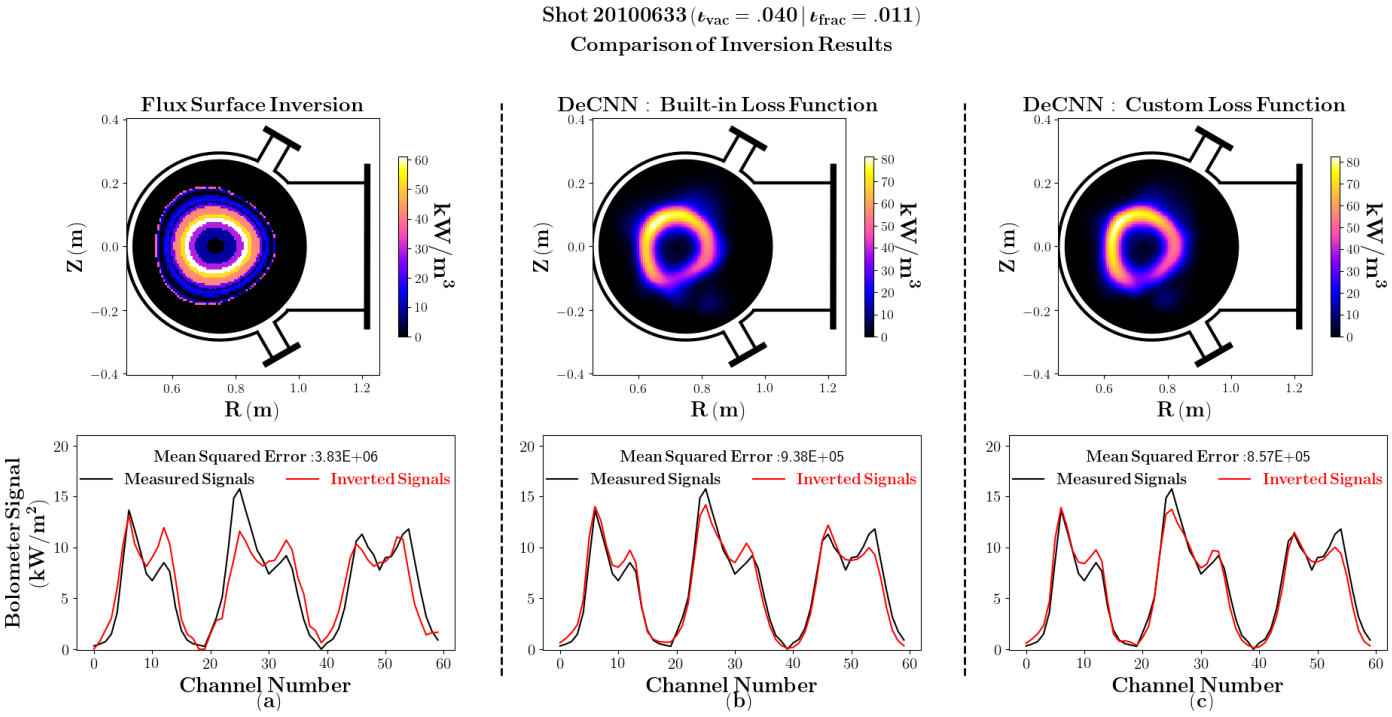

Figure A.1: Complex plot example.

```
import numpy as np
import matplotlib
from flux_surface_grid_inv_direct import FluxSurfaceGrid
from general_analysis import Analysis
an = Analysis()

matplotlib.rcParams.update(matplotlib.rcParamsDefault)
matplotlib.rcParams['text.usetex'] = True
matplotlib.rcParams['text.latex.preamble'] = [
    r'\usepackage{amsmath}',
    r'\usepackage{amssymb}',
    r'\usepackage{color}',
    r"\DeclareRobustCommand*{\iotabar}{\ensuremath{\raisebox{-.7ex}{$\mat
    \mkern-8mu\boldsymbol{\iota}}}}",
    r"\DeclareMathSymbol{\mh}{\mathord}{operators}{`\-}"]
```

```
matplotlib.rcParams.update({'font.size': 15})
matplotlib.rcParams.update({'font.weight':'bold'})
matplotlib.rc('font', **{'family': 'sans-serif', 'sans-serif': ['DejaVu S
matplotlib.rc('text', usetex=True)
plt = matplotlib.pyplot
Line2D = matplotlib.lines.Line2D
gridspec = matplotlib.gridspec
font = {'weight' : 'bold',
        'size'   : 15,}

# Initiating Flux Surface Grid
wfile = 'wout.example.nc'
grid1 = FluxSurfaceGrid(wfile, size=96)
grid1.make_grid(manually_set_size=True,
                size = [[0.75-0.295,0.75+0.295],[-0.295, 0.295]])

# Compare models with vacuum vessel plotted
fig = plt.figure(figsize=(18,10))
gs = gridspec.GridSpec(3, 3,height_ratios=[.0001,1.2,1],
width_ratios=[1,1,1])#,hspace=0)#, wspace=0.1, hspace=.1)

plt.subplot(gs[0,:])
plt.title(r'$\bold{Shot \, 20100633 \,( \iotabar_{vac} = .040 \,
| \, \iotabar_{frac} = .011)}$'+
'\n'+r'$\bold{ Comparison \, of \, Inversion \, Results}$',
fontsize=20)
plt.axis('off')
plt.subplot(gs[1,0])
```

```
bolo_inv_grid = np.load('bolo_inv_grid.npy')
grid1.grid['grid_data'] = bolo_inv_grid/1E3
grid1.plot_grid(cbar_label=r'$\bold{kW/m^3}$')
an.plot_vacuum_vessel(circle_size=.44)
plt.xlabel(r'$\bold{R␣\,␣(m)}$',fontsize = 20,
weight ='bold',usetex=True)
plt.ylabel(r'$\bold{Z␣\,␣(m)}$',fontsize = 20,
weight ='bold',usetex=True)
plt.title(r'$\bold{␣Flux␣\,␣Surface␣\,␣Inversion}$',
          fontsize=20)


plt.subplot(gs[1,1])
builtin_grid = np.load('decnn_builtin_loss_grid.npy')
grid1.grid['grid_data'] = builtin_grid/1E3
grid1.plot_grid(cbar_label=r'$\bold{kW/m^3}$')
an.plot_vacuum_vessel(circle_size=.44)
plt.xlabel(r'$\bold{R␣\,␣(m)}$',fontsize = 20,
weight ='bold',usetex=True)
plt.ylabel(r'$\bold{Z␣\,␣(m)}$',fontsize = 20,
weight ='bold',usetex=True)
plt.title(r'$\bold{DeCNN:␣\,␣Built␣\text{-}␣in␣\,␣Loss␣\,␣Function}$',
          fontsize=20)


plt.subplot(gs[1,2])
custom_grid = np.load('decnn_custom_loss_grid.npy')
grid1.grid['grid_data'] = custom_grid/1E3
```

```
grid1.plot_grid(cbar_label=r'$\bold{kW/m^3}$')
an.plot_vacuum_vessel(circle_size=.44)
plt.xlabel(r'$\bold{R\,(m)}$',fontsize = 20,
weight ='bold',usetex=True)
plt.ylabel(r'$\bold{Z\,(m)}$',fontsize = 20,
weight ='bold',usetex=True)
plt.title(r'$\bold{DeCNN:\,Custom\,Loss\,Function}$',
          fontsize=20)


plt.subplot(gs[2,0])
p_x = np.linspace(0,59,60)
bolo_inv_signals = np.load('bolo_inv_signals.npy')
bolo_data_sub = np.load('bolo_data.npy')
mse0 = np.sum((bolo_data_sub-bolo_inv_signals)**2)/60
plt.plot(p_x, bolo_data_sub/1E3, 'k',
label=r'$\bold{Measured\,Signals}$')
plt.plot(p_x, bolo_inv_signals/1E3, 'r',
label=r'$\bold{Inverted\,Signals}$')
plt.xlabel(r'$\bold{Channel\,Number}$',fontsize = 20,
weight ='bold',usetex=True)
plt.ylabel(r'$\bold{Bolometer\,Signal}$' +'\n' +
r'$\bold{(kW/m^2)}$',fontsize = 20, weight ='bold',usetex=True)
leg=plt.legend(prop=font,ncol=2,loc=9,frameon=False)
leg.get_texts()[1].set_color('r')
leg.set_title(r'$\bold{Mean\,Squared\,Error:}$' +
'{:.2E}'.format(mse0),prop={'size':15})
plt.ylim([-.05, 21])
```

```
plt.subplot(gs[2,1])
p_x = np.linspace(0,59,60)
builtin_signals= np.load('decnn_builtin_loss_signals.npy')
mse1 = np.sum((bolo_data_sub-builtin_signals)**2)/60
plt.plot(p_x, bolo_data_sub/1E3, 'k',
label=r'$\bold{Measured \, Signals}$')
plt.plot(p_x, builtin_signals/1E3, 'r',
label=r'$\bold{Inverted \, Signals}$')
plt.xlabel(r'$\bold{Channel \, Number}$',fontsize = 20,
weight ='bold',usetex=True)
#plt.ylabel(r'$\bold{Bolometer \, Signal \, (kW/m^2)}$',
fontsize = 20, weight ='bold',usetex=True)
leg=plt.legend(prop=font,ncol=2,loc=9,frameon=False)
leg.get_texts()[1].set_color('r')
leg.set_title(r'$\bold{Mean \, Squared \, Error:}$' +
'{:.2E}'.format(mse1),prop={'size':15})
plt.ylim([-.05, 21])

plt.subplot(gs[2,2])
p_x = np.linspace(0,59,60)
custom_signals= np.load('decnn_custom_loss_signals.npy')
mse2 = np.sum((bolo_data_sub-custom_signals)**2)/60
plt.plot(p_x, bolo_data_sub/1E3, 'k',
label=r'$\bold{Measured \, Signals}$')
plt.plot(p_x, custom_signals/1E3, 'r',
label=r'$\bold{Inverted \, Signals}$')
plt.xlabel(r'$\bold{Channel \, Number}$',fontsize = 20,
```

```
weight ='bold',usetex=True)
#plt.ylabel(r'$\bold{Bolometer \, Signal \, (kW/m^2)}$',
fontsize = 20, weight ='bold',usetex=True)
leg=plt.legend(prop=font,ncol=2,loc=9,frameon=False)
leg.get_texts()[1].set_color('r')
leg.set_title(r'$\bold{Mean\ \,\ Squared\ \,\ Error:}$' +
'{:.2E}'.format(mse2),
prop={'size':15})
plt.ylim([-.05, 21])


fig.text(.2,.005,r'$\bold{(a)}$',fontsize = 20, weight ='bold',
usetex=True,ha='center')
fig.text(.525,.005,r'$\bold{(b)}$',fontsize = 20, weight ='bold',
usetex=True,ha='center')
fig.text(.845,.005,r'$\bold{(c)}$',fontsize = 20, weight ='bold',
usetex=True,ha='center')


x1 = .36
x2 = .68
l1 = Line2D([x1,x1], [0.05, .85],c='k',linestyle='--', linewidth=2,
transform=fig.transFigure, figure=fig)
l2 = Line2D([x2,x2], [0.05, .85],c='k',linestyle='--', linewidth=2,
transform=fig.transFigure, figure=fig)
fig.lines.extend([l1, l2])
plt.tight_layout()
figManager = plt.get_current_fig_manager()
```

```
figManager.window.showMaximized()
plt.show()
```

Appendix B

Absolute Calibration of Bolometers Calculation using Projected Planes

Jeff Herfindal's work in designing, building, and calibrating the SXR cameras has played an immense role in the work of this thesis. An exploded view of the SXR cameras can be seen in Fig. B.1. This appendix is meant to extend the relative calibration of the two-color system into an absolute calibration. The relative calibration was all that was required for two-color system because when determining the electron temperature, the original goal of the system, the thin and thick filtered signals are divided by each other removing the need for an absolute calibration.

For the relative calibration, the geometric factor of the system was found. While the geometric factor derivation can be found in appropriate detail in Herfindal's Thesis, it is defined as

$$f_{\text{g}} = \frac{A_{\text{diode}} A_{\text{slit}}}{4\pi d^2} \cos^4\alpha \tag{B.1}$$

where A_{diode} is the area of diode, A_{slit} is the area of the slit, and d is the distance between the two. The angle α is the angle between the diode and the slit as defined in Fig. B.2.

In practice, the relative geometric factor was actual found by measuring each diode response to a source while the SXR camera was translated on an optics bench. By normalizing each measured response to the response of the diode closest to the plane the slit in Fig. B.2 (such as diode 11 in the 20 diode array), Eq. B.2 can be rewritten as

$$f_{i,\text{relative}} = \frac{f_i}{f_{11}} = \frac{\cos^4\alpha_i}{\cos^4\alpha_{11}} \tag{B.2}$$

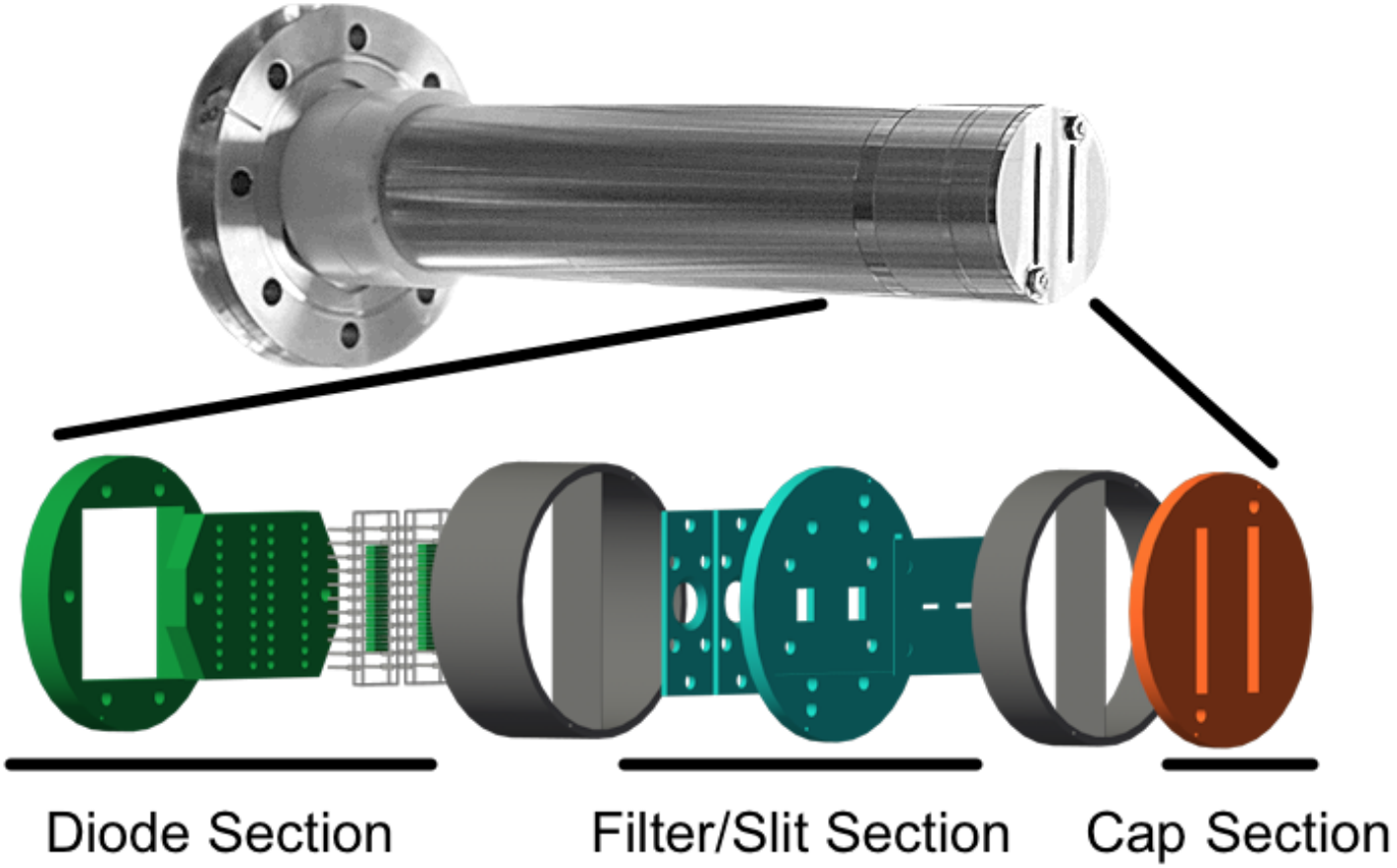

Figure B.1: Exploded view of the two-color system.

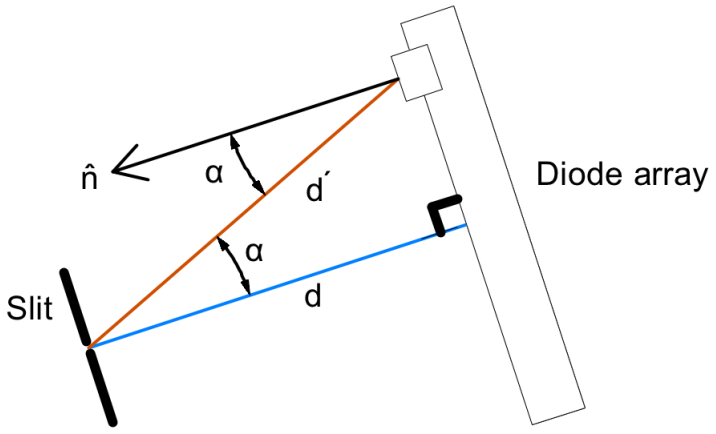

Figure B.2: Illustration of the apparent slit width as viewed by the diode.

Having measured the relative geometric factor, the final task that remains is to find the geometric factor for diode 11 (f_{11}) using Eq. B.2. A difficulty arises because the poloidal slit is not at the same slit as the toroidal slit. So to resolve Eq. B.2, the poloidal slit was projected to the toroidal slit's location, taking into consideration the physical size of the diode to accurately get a projection. Using the absolutely calibrated bolometers, the raw signals in volts can be converted to W/m^2 or power incident on the surface of each diode.